Seismic structure and crustal accretion along an intermediate-rate mid-ocean ridge segment

Robert Todd Weekly

A dissertation submitted in partial fulfillment of the

requirements for the degree of

Doctor of Philosophy

University of Washington

2013

Reading Committee:

William S.D. Wilcock, Chair

Thomas L. Pratt

Kenneth C. Creager

Department Authorized to Offer Degree:

Earth and Space Sciences

University of Washington

Abstract

Seismic structure and crustal accretion along an intermediate-rate mid-ocean ridge segment

Robert Todd Weekly

Chair of the Supervisory Committee:

Professor William S.D. Wilcock

School of Oceanography

Epicenters and magnitudes for 36,523 earthquakes recorded along the Endeavour segment between August 2003 and October 2006 are automatically determined using a local ocean-bottom seismometer (OBS) network. The catalog is dominated by two swarm sequences in January and February 2005 in the vicinity of the Endeavour overlapping spreading center, which included earthquakes in West Valley, the northern portion of the Endeavour segment, southwest Endeavour Valley and the Endeavour vent fields. These swarms are attributed to volcanism including a dike intrusion on the northern Endeavour in February 2005 and smaller diking events on the propagating tip of the West Valley segment in both swarms. The dike on the northern Endeavour propagated to the south, which is inconsistent with magma sourced from the axial magma chamber beneath the elevated central portion of the segment. Following the

swarms, seismic activity on the Endeavour segment decreased on average to ~15% of pre-swarm values and almost ceased at the segment ends. I infer that a six-year non-eruptive event that started with a swarm in 1999 and finished with the 2005 swarms ruptured the entire segment and relieved plate-spreading stresses. The inferred coupling between the 1999 and 2005 events, the observation of extensive precursory activity prior to the 2005 swarms, and the interaction between seismically active regions during the swarms is consistent with static triggering with delays influenced by viscoelastic relaxation, hydraulic diffusion and magma withdrawal and replenishment.

The isotropic and anisotropic *P*-wave velocity structure of the upper oceanic crust on the Endeavour Segment of the Juan de Fuca Ridge is studied using refracted travel time data collected by an active-source, three-dimensional tomography experiment. The isotropic velocity structure is characterized by low crustal velocities in the overlapping spreading centers (OSCs) at the ends of the segment. These low velocities are indicative of pervasive tectonic fracturing and persist off-axis, recording the history of ridge propagation. Near the segment center, velocities within the upper 1 km show ridge-parallel bands with low velocities on the outer flanks of topographic highs. These features are attributed to localized thickening of the volcanic extrusive layer from eruptions extending outside of the axial valley that flow down the fault-tilted blocks that form the abyssal hill topography. On-axis velocities are relatively high beneath the hydrothermal vent fields due to the infilling of porosity by mineral precipitation. Lower velocities are observed beneath the most vigorous vent fields in a seismically active region above the axial magma chamber and may reflect increased fracturing and higher temperatures. Seismic anisotropy is high on-axis but decreases substantially off-axis over ~8 km (0.3 Ma). This decrease coincides with an increase in seismic velocities at depths ≥1 km and is attributed to the

infilling of cracks in the sheeted dike layer by mineral precipitation associated with near-axis hydrothermal circulation. The orientation of the fast-axis of anisotropy is ridge-parallel near the segment center but curves near the segment ends reflecting the tectonic fabric within the OSCs.

TABLE OF CONTENTS

LIST OF FIGURES

LIST OF TABLES

ACKNOWLEDGEMENTS

The work presented within this dissertation would not have been possible without the assistance, guidance, and support of many individuals. My primary advisor, William Wilcock, was instrumental in developing my research and providing a seemingly endless amount of support, both academically and personally, to assist me in this accomplishment. William was always honest, direct, and available for discussion about a wide range of topics that extended beyond the scope of immediate scientific pursuits. He also provided valuable insight about balancing the economic and political interests of the Marine Operations department responsible for maintaining an active oceanographic research vessel. Perhaps most admirably, he is also a dedicated father and husband who was always vivaciously engaged in his personal life. During my time as his student, I realized that William is a vital contributor of the School of Oceanography and is a prime example of the type of faculty member that drives graduate students to the University of Washington. I have learned a tremendous amount from him about mid-ocean ridge research and scientific methodologies, but also how to conduct myself professionally in an academic framework. William is an ideal model of a research scientist and I consider myself extremely fortunate to have had the opportunity to have him as a mentor.

My committee members, Kenneth Creager, Thomas Pratt, Marv Lilley, and Steve Kramer were incredible resources who encouraged me to think critically about the broader implications of my research when I was focused on smaller details. They challenged me to explore hypotheses that extended beyond the scope of my discipline and made me a better scientist in the process. Conversations with Thomas were particularly helpful when discussing ways to improve my writing technique that allowed the research to be conveyed to the broader scientific

community in a thoughtful, impactful way. His professional experience helped me consider how my science was going to be received by different audiences.

Both experiments discussed within the dissertation were partly organized and co-funded by faculty members at the University of Oregon, Doug Toomey and Emilie Hooft. I was extremely lucky to have the chance to interact with both of them on a semi-regular basis and their guidance on conducting research, drafting manuscripts, and maintaining professional relationships has been invaluable. Their support and input as co-authors for the two manuscripts that came out of this dissertation was extremely helpful and I remain grateful for being able to tap into their extensive research experience. Additionally, I will always remember our time spent together aboard the R/V Marcus Langseth along cruise MGL-0910 and the many accomplishments and tribulations that came with it.

The data collection and analysis of this work would not have been possible without the efforts of the ship operations and technical crew of the R/V Thomas Thompson, R/V Marcus Langseth, R/V Western Flyer, ROPOS, and Tiburon. Our time at sea together was something I will never forget, and thank you for the opportunity to experience working and living at sea in a friendly, inclusive environment.

Attaining my degree would have been exponentially more difficult without the constant support of other graduate students who were always there to celebrate every accomplishment along the way. I consider myself very fortunate to develop a plethora of friendships within the department of Earth and Space Sciences and the School of Oceanography at the University of Washington, and also within the department of Geological Sciences at the University of Oregon. I take away an abundance of incredible memories and sincerely look forward to keeping track of

everyone as we continue to grow and pursue our interests, whether they focus on research or otherwise.

My parents are ultimately responsible to introducing me to and fostering a personal connection to the ocean. They allowed me to spend much of my adolescence surfing and scuba diving along the beaches of California and Mexico while developing a curiosity and appreciation for the ocean. While they helped start the journey, my wife, Lora, has helped me through this most recent part. Throughout my time in graduate school, her unwavering support has been instrumental in providing me with the motivation to finish and accomplish all that I have. I would not be the man I have become without her. Thank you for always having faith in my abilities and for loving me unconditionally.

DEDICATION

for Lora

Chapter 1

INTRODUCTION

The global mid-ocean ridge (MOR) system constitutes an elongate chain of seafloor volcanoes that is found in each of the Earth's oceans and is responsible for continuously repaving about two-thirds of the surface of the Earth through the formation of oceanic crust. Along these divergent plate boundaries, decompressional melting of upwelling mantle peridotite [*Kushiro*, 2001] produces magma that buoyantly rises and ponds at shallow crustal depths. The genesis of relatively uniform 6-km-thick oceanic crust occurs through episodic volcanic activity, including seafloor eruptions and crustal dike injections [*Delaney et al.*, 1998]. As the crust ages and moves away from the spreading center, it is subsequently altered by dynamic interactions between extensional tectonic faulting and hydrothermal circulation. Tectonic activity associated with brittle faulting accommodates lithospheric extension and alters the permeability of the crust to facilitate hydrothermal circulation. Hydrothermal fluid circulation cools oceanic crust and controls magma solidification and the depth of brittle-ductile transition [*Toomey et al.*, 1985].

1.1 Summary of mid-ocean ridge morphologies

MOR segments display a wide range of morphologic characteristics that are influenced by the relative contributions of volcanic, tectonic, and hydrologic subsurface processes. Global studies of MORs show that ridge-spreading rate is the primary variable for determining the morphology of a ridge segment and the relative contributions of these processes to crustal accretion [*Purdy et al.*, 1992; *Sinton and Detrick*, 1992; *Phipps Morgan and Chen*, 1993b]. Along fast-spreading rate ridges, the rate of magma supply to the segment balances the rate that

hydrothermal fluids extract heat from the crust, and a steady-state axial magma chamber (AMC) forms beneath the magmatically active portion of the segment [*Sinton and Detrick*, 1992]. The ridge crest is characterized by a gentle bathymetric rise with low relief and spreading is primarily accommodated by episodic eruptive diking events in the upper crust and ductile flow in the lower crust [*Haymon et al.*, 1991; *Sinton and Detrick*, 1992; *Delaney et al.*, 1998; *Macdonald*, 1998]. Several seafloor eruptions associated with magmatic dike intrusion have been detected along the fast-spreading East Pacific Rise [*Haymon et al.*, 1993; *Tolstoy et al.*, 2006; *Soule et al.*, 2007] and the southern portion of the intermediate-rate Juan de Fuca Ridge [*Sohn et al.*, 1998a; 1999b; *Dziak et al.*, 2007].

Conversely, the rate of spreading along slow-spreading rate ridges is insufficient to sustain a steady-state AMC and accretion is accommodated by alternating episodes of amagmatic, fault-controlled extension and ephemeral volcanism [*Smith and Cann*, 1993]. Along these segments, hydrothermal circulation is facilitated by steep listric normal faults that allow fluids to permeate and cool thicker portions of the crust [*Sinton and Detrick*, 1992]. Along these faults are localized zones of hydrothermal alteration where water-rock reactions form clay-like minerals that clog the fluid flow pathways if the faults become inactive [*Wilcock and Fisher*, 2004]. Intermediate-spreading rate segments contain elements of both fast- and slow-spreading systems. Specifically, like fast-spreading ridges they contain a steady-state crustal AMC that tends to reside deeper in the crust and it has been proposed that, like slow-spreading ridges, hydrothermal circulation is controlled by steep inward-dipping faults that bound the axial valley [*Carbotte et al.*, 2006; *Van Ark et al.*, 2007].

1.2 Seismic data acquisition

Seismic techniques, including earthquake monitoring and seismic imaging, are extremely useful for understanding subsurface geological processes [*Tolstoy*, 2008]. Long-term earthquake monitoring enables investigations of the linkages between tectonic, volcanic, and hydrologic processes including normal-fault driven extension, magmatic recharge and dike injection, and thermal strain induced by hydrothermal circulation [*Fox and Dziak*, 1998; *Tolstoy et al.*, 2006; *deMartin et al.*, 2007; *Wilcock et al.*, 2009]. Along fast-spreading rate ridges, small magnitude ($M < 3$) earthquakes within the shallow crust are common and seismicity rates are driven by volcanic emplacement and hydrothermal cooling. In contrast, earthquakes at slow-spreading rate ridges are larger in magnitude ($M \sim 5$), occur deeper in the crust and result from tectonic and volcanic processes.

Characterizing the seismic velocity structure of a MOR segment is commonly performed using two complementary seismic techniques; multi-channel seismic reflection and travel-time tomography. Multi-channel reflection studies image sharp sub-horizontal changes in seismic impedance (the product of density and velocity) and are thus well-suited to imaging interfaces in lithology or porosity. Along MORs they have been particularly important for imaging the geometry of the crustal AMC and the base of the volcanic extrusive layer [*Detrick et al.*, 1987; 1990; *Kent et al.*, 1990; *Mutter*, 1992; 1995; *Detrick et al.*, 2002]. Recent studies have also shown that MCS techniques are capable of imaging melt bodies away from the ridge-axis [*Canales et al.*, 2012]. Tomographic images are obtained by inverting crustal refraction travel-time data obtained from recording airgun shots using ocean-bottom seismometers [*Toomey et al.*, 1990; *Toomey et al.*, 1994; *Bazin et al.*, 1998; *Dunn et al.*, 2000; *West et al.*, 2001; *Seher et al.*, 2010a]. They provide a three-dimensional view of the seismic velocity structure, which is

sensitive to variations in crustal porosity structure, lithology, presence of magma or partial melt, and crustal temperature.

The crux of this dissertation is better constraining the variability of crustal accretion along an intermediate-spreading rate ridge segment using two of the aforementioned seismic techniques. I combine microearthquake and tomography data collected from the Endeavour Segment of the Juan de Fuca Ridge to (1) understand the relative contributions of tectonic and volcanic processes to episodes of seafloor spreading, and (2) identify how crustal accretion varies in the magmatically active central portion of a spreading segment compared to the ends of the segment, where no magma chamber is observed.

1.3 Endeavour segment geologic setting

The Endeavour Segment is a 90-km-long intermediate-rate spreading segment located near the northern end of the Juan de Fuca Ridge that is bounded to the north and south by the left-stepping Endeavour and Cobb overlapping spreading centers (OSCs). The central portion of the segment is comprised of a 1-km-wide, 75-m-deep axial valley and is flanked by a series of volcanically constructed ridge-parallel abyssal hills and valleys spaced ~6 km apart. This ridge-basin sequence overlies a broad (~45-km-wide) regional plateau that extends out to crustal ages of 0.7 Myr and coincides with the onset of the Brunhes/Matayama magnetic reversal [*Karsten et al.*, 1990; *Carbotte et al.*, 2008]. It has been proposed that current magma supply to the segment is influenced by the mantle melt anomaly associated with nearby seamount chains [*Karsten et al.*, 1986; *Karsten and Delaney*, 1989; *Carbotte et al.*, 2008]. Within the axial valley are five high-temperature hydrothermal vent fields spaced 2-3 km apart that host large sulfide structures [*Delaney et al.*, 1992; *Robigou et al.*, 1993; *Kelley et al.*, 2001; *Kelley et al.*, 2002; *Glickson et*

al., 2007]. The vent fields have been the focus of interdisciplinary studies since their discovery and are of particular interest to hydrothermal researchers due to the temperature and chemistry gradients that are found within and between fields [*Lilley et al.*, 1993; *Butterfield et al.*, 1994].

Chapter 2

TERMINATION OF A SIX-YEAR RIDGE-SPREADING EVENT OBSERVED USING A SEAFLOOR SEISMIC NETWORK ON THE ENDEAVOUR SEGMENT, JUAN DE FUCA RIDGE

2.1 Introduction

Earthquakes occurring along mid-ocean ridges result from the release of stress within the brittle portion of oceanic lithosphere. Plate spreading processes that contribute to stress accumulation include extensional tectonics [*Toomey et al.*, 1988; *Wolfe et al.*, 1995; *Barclay et al.*, 2001; *deMartin et al.*, 2007], magmatic activity [*Sohn et al.*, 1998a; *Dziak and Fox*, 1999a; b; *Dziak et al.*, 2004; *Wilcock et al.*, 2009], and hydrothermal circulation [*Sohn et al.*, 1998b; *Wilcock et al.*, 2002; *Tolstoy et al.*, 2006; *Tolstoy et al.*, 2008]. The relative contributions of each process to the local stress field is determined by spreading rate [*Tolstoy*, 2008] and each of these processes produce distinct patterns of seismicity.

Along slow-spreading-rate ridges (1-4 cm/yr full rate) [*Macdonald*, 2001], such as the Mid-Atlantic Ridge (MAR), the rate of spreading is believed to be insufficient to sustain a steady-state axial magma chamber (AMC) [*Sinton and Detrick*, 1992; *Phipps Morgan and Chen*, 1993a]. Stress accumulation and axial valley morphology are influenced by alternating episodes of volcanism and tectonic extension [*Karson et al.*, 1987; *Smith and Cann*, 1992; 1993]. Earthquakes observed on the MAR have magnitudes up to about $M_w = 5$, extend up to 8 km deep beneath the axial valley and adjacent rift mountains, and have focal mechanisms consistent with normal faulting [*Toomey et al.*, 1985; *Huang et al.*, 1986; *Wolfe et al.*, 1995; *Barclay et al.*, 2001; *deMartin et al.*, 2007]. Large magnitude events tend to be followed by aftershock sequences that show a modified Omori law decay pattern and yield *b*-values of ~1.0 [*Bohnenstiehl et al.*, 2002].

At fast- (>9 cm/yr full rate) and intermediate- (4-9 cm/yr full rate) spreading-rate ridges, extension is primarily accommodated via episodic diking events driven by a steady-state crustal AMC [*Sinton and Detrick*, 1992; *Delaney et al.*, 1998]. The earthquakes are smaller because the lithosphere is thin and a large proportion of fault slip occurs aseismically [*Cowie et al.*, 1993; *Tolstoy*, 2008]. Between episodic diking events, the highest concentration of microearthquakes occurs directly above the AMC in the shallow crust and is associated with thermo-mechanical strain induced by a combination of hydrothermal cooling [*Wilcock et al.*, 2002; *Sohn et al.*, 2004] and magma chamber inflation [*Wilcock et al.*, 2009]. Because of the importance of diking events in crustal formation and interest in understanding their impacts on seafloor hydrothermal and biological processes [*Delaney et al.*, 1998], considerable efforts have been made to respond to these events [*Cowen et al.*, 2004] and understand their characteristics. Earthquakes associated with seafloor eruptions have been investigated using local seismic networks or regional hydroacoustic arrays on the East Pacific Rise (EPR) at 9˚50' N [*Tolstoy et al.*, 2006], the Juan de Fuca Ridge [*Dziak et al.*, 1995; *Dziak and Fox*, 1999a; *Sohn et al.*, 1999a; *Dziak et al.*, 2011], and the Gorda Ridge [*Fox and Dziak*, 1998]. Diking events are marked by the onset of intense earthquake swarms that lack a discernible mainshock-aftershock sequence and the magnitude-frequency distribution of these swarms yield *b*-values significantly greater than unity [*Bohnenstiehl et al.*, 2002]. The rate of seismicity can build for several years prior to an eruption with precursory swarms lasting a few hours, while the dike injection occurs over the course of 1-2 weeks and is accompanied by extensive seismicity with rates >25 events/hr [*Dziak and Fox*, 1999b]. Post-eruption seismicity rates decline sharply and return to background levels on timescales of several months as the crust returns to thermal equilibrium [*Sohn et al.*, 1998a].

In contrast to diking events that feed seafloor eruptions, the seismicity associated with

intrusive diking events has not been extensively studied. A notable exception is the Endeavour segment of the Juan de Fuca Ridge where swarms in June 1999 and January 2000 [*Johnson et al.*, 2000; *Bohnenstiehl et al.*, 2004] and February 2005 [*Hooft et al.*, 2010] were investigated with hydroacoustic recordings and a local seismic network, respectively. In this section, i present a three-year catalog of seismicity obtained with an automated algorithm devised to process a large amount of data recorded by a local seafloor OBS network deployed on the Endeavour segment from 2003 – 2006. The catalog includes two substantial swarms in January and February 2005. I discuss the characteristics of the two swarms and their contribution to the spreading cycle, compare them to magmatic events in other locations and discuss the role of precursory activity and triggering.

2.2.1 Regional geology

The Juan de Fuca Ridge (JdFR) is an intermediate-rate (5.7 cm/yr [*DeMets et al.*, 1994]) spreading center located in the northeast Pacific Ocean that forms the boundary between the Pacific and Juan de Fuca plates (Figure 1a, inset). The JdFR is comprised of seven individual spreading segments that are bounded by large OSCs. The regional tectonics of the northern JdFR are complicated by the presence of an unstable triple junction [*Hyndman et al.*, 1979] where the Sovanco and Nootka transform faults intersect the ridge, and by north-south compression resulting from the relative motions of the Pacific and Explorer plates [*Kreemer et al.*, 1998].

The Endeavour Segment is a 90-km-long spreading segment located near the northern end of the JdFR (Figure 1a). The segment is bounded to the north and south by the Endeavour and Cobb OSCs, respectively, with several prominent seamount chains located on its western

flank. The central portion of the segment comprises a series of ridge-parallel abyssal hills and valleys spaced ~6 km apart [*Karsten et al.*, 1986]. This ridge-basin sequence overlies an elevated plateau with thickened crust that extends out to ages of 0.7 Ma [*Carbotte et al.*, 2008]. It has been proposed that magma supply is enhanced because the ridge has overridden the mantle melt anomaly that generated the Heckle Seamount chain [*Karsten and Delaney*, 1989; *Carbotte et al.*, 2008].

At the center of the segment, five high-temperature (>300˚C) black smoker fields are spaced 2-3 km apart within the 1-km-wide, 75-m-deep axial valley (Figure 1b) with several low-temperature (<100˚C) diffusely venting sites interspersed between the fields [*Delaney et al.*, 1992; *Robigou et al.*, 1993; *Kelley et al.*, 2001; *Kelley et al.*, 2002; *Glickson et al.*, 2007]. From north to south, the fields are named Sasquatch, Salty Dawg, High Rise, Main Endeavour Field, and Mothra (Figure 1b). *Wilcock and Delaney* [1996] suggested that tectonic faulting and downward propagation of a cracking front into a solidified magma chamber controlled heat supply and hydrothermal circulation beneath the vent fields. More recently, however, a multi-channel seismic dataset imaged an AMC underlying all of the vent fields at a depth of 2-3 km beneath the seafloor [*Carbotte et al.*, 2006; *Van Ark et al.*, 2007]. The presence of an AMC suggests that a substantial amount of magmatic heat is being supplied to the hydrothermal system and that volcanism is an integral component of present-day plate spreading and seismogenesis at the Endeavour segment.

2.2.2 Seismicity

The U.S. Navy's Sound Surveillance System (SOSUS) hydrophone network provides a record of ~50,000 earthquakes larger than magnitude ~2 that have occurred along the Juan de

Fuca Ridge since 1991 [*Dziak et al.*, 2011]. With the exception of Axial Seamount, the southern and central segments of the JdFR have been seismically active only during periods of volcanism. In contrast, the northern portion of the JdFR, including the Endeavour, has been continually seismically active and the locus of many seismic swarms.

Two periods of particular interest are swarm sequences recorded between June 1999 and January 2000 along the central and southern portions of the Endeavour segment [*Johnson et al.*, 2000; *Bohnenstiehl et al.*, 2004], and between January and March 2005 along the northern Endeavour and adjacent southern West Valley Segments [*Hooft et al.*, 2010]. Although *Johnson et al.* [2000] originally interpreted the June 1999 swarm as having a tectonic source, the frequency-magnitude distribution of earthquakes [*Bohnenstiehl et al.*, 2002], strain-induced pressure changes in regional boreholes [*Davis et al.*, 2001] and perturbations to the fluid chemistry and volatile content [*Lilley et al.*, 2003; *Seewald et al.*, 2003; *Seyfried et al.*, 2003] are consistent with a non-eruptive diking event. *Bohnenstiehl et al*. [2004] argue that dike propagation associated with the June 1999 swarm increased post-seismic Coulomb stress levels immediately to the south of the swarm terminus and led to a second swarm in January 2000 that had a more limited along-axis extent.

In addition to the SOSUS records, the 2005 swarms were recorded by a local OBS network. *Hooft et al*. [2010] located over 6,000 earthquakes for the February swarm using manual picks. The spatial and temporal pattern of earthquakes is complex with the locus of seismicity evolving over the course of the swarm as earthquakes occur near the Endeavour Seamount and West Valley Segment, on the northern Endeavour Segment, within the Endeavour Valley and under the vent fields. The majority of moment release, including the six largest earthquakes that have strike-slip mechanisms, occurred at the southwest end of the Endeavour

Valley near the southern extension of the West Valley Segment. However, the magnitude and polarity of borehole pressure anomalies and their timing relative to the onset of seismicity indicated a dike intrusion on the northern portion of the Endeavour Segment [*Hooft et al.*, 2010]. The February 2005 swarm triggered earthquakes and a hydrologic response within the vent fields. An increase in vent field seismicity occurred within ~2.5 days of the onset of the swarm, coincident with a modest temperature increase (~4 ˚C) at a diffuse vent in the Mothra field. *Hooft et al*. [2010] interpret this delay between swarm onset and observed thermal anomalies as the time required for a hydrologic pressure perturbation to diffuse along the ridge.

A number of studies at the Endeavour Segment have employed local OBS networks to study microearthquakes associated with hydrothermal venting [*McClain et al.*, 1993; *Wilcock et al.*, 2002; *Wilcock et al.*, 2009]. *McClain et al*. [1993] argued that ongoing tectonic extension maintains the conduits necessary for sustained fluid circulation and formation of mature hydrothermal vent fields. A 55-day study in 1995 located nearly 1,000 earthquakes concentrated at ~2 km depth beneath the axial valley with focal mechanisms that were consistent with plate spreading and tensile stresses due to hydrothermal cooling [*Wilcock et al.*, 2002]. Focal mechanisms for 170 events occurring beneath the hydrothermal vent fields during 2003-2004 similarly delineate a zone of ridge-perpendicular horizontal tension [*Wilcock et al.*, 2009]. However this region was bracketed by zones of compression on the ridge flanks, which suggests that seismicity at the ridge-axis results from magmatic inflation of the AMC rather than tectonic extension [*Wilcock et al.*, 2009].

2.3 Keck seismic network

From August 2003 to October 2006, an eight-station, 10-km-aperture array was deployed

along the central portion of the Endeavour Segment of the Juan de Fuca Ridge (Figure 1b). The array comprised seven short-period three-component corehole ocean-bottom seismometers (OBS) deployed in horizontal drill holes or concrete "seismonuments" [*Stakes et al.*, 1998] and one buried broadband Guralp CMG-1T OBS [*Stakes et al.*, 2002; *Romanowicz et al.*, 2006]. The short-period sensor comprised three orthogonal Mark Products L-28LB geophones that have a flat frequency response from 1 – 90 Hz and were sampled at 128 Hz. The broadband sensor was a three-component Guralp CMG-1T that has a flat frequency response from 2.8 mHz – 50 Hz and was sampled at either 50 or 100 Hz.

The Keck network was deployed in a novel way using remotely operated vehicles (ROVs) instead of traditional free-fall seismometer deployment methods [*Wilcock et al.*, 2007]. This ensured strong coupling of the sensors to the seafloor and enabled measurement of horizontal sensor orientation. Using ROVs for annual deployments ensured that the network continued to record high-quality data comparable to land-based seismometer networks for over 39 consecutive months and allowed the determination of a microearthquake catalog that, to date, spans a longer period of time than any other earthquake catalog derived from a seafloor OBS network. There were, however, periods of instrument failures in years 2 and 3 that are summarized in Table 1.

To correct for timing errors, I calculated clock corrections by assuming a constant drift rate between each deployment and recovery. I was unable to obtain clock offsets upon recovery of station KEBB after the second year, and stations KEMF, KENE, KENW and KESE after the third year due to instrument power loss before recovery. For stations KENE, KENW and KESE in year 3, clock drift rates were obtained using the known times of 190 shots (40 in^3 source volume) obtained in July 2006 with the *R/V Tully*. Clock drift rates for stations KEBB in year 2

and KEMF in year 3 were calculated iteratively during the earthquake analysis by fitting a trend to the mean daily misfit between observed and predicted times for earthquake arrivals.

2.4 Automated location methods

In order to process the data efficiently, I implement an automatic algorithm which locates earthquakes using *Hypoinverse* [*Klein*, 2002] with a layered velocity model derived from earlier studies (Figure 2); the method is described in detail in Appendix A. The algorithm uses the ratio of the root-mean-squared (RMS) amplitudes in short-term and long-term windows to trigger on impulsive arrivals, associates triggers observed on multiple stations as events and distinguishes earthquakes from ~20-Hz whale calls [*Cummings and Thompson*, 1971; *Watkins et al.*, 1987] on the basis of frequency content. For each earthquake, it picks potential *P*- and *S*-wave arrival times based on sharp increases in the smoothed RMS amplitude and with an auto-regressive method [*Takanami and Kitagawa*, 1988], assigns pick weights on the basis of signal-to-noise, and systematically searches for an earthquake location that maximizes the number of adequately modeled picks. Earthquakes located more than 3 km from the nearest station are assigned a fixed focal depth of 3 km, the average depth of earthquakes determined both on- and off-axis in an earlier study [*Wilcock et al.*, 2002]. The final catalog uses *P*- and *S*-wave picks obtained from the autoregressive and RMS amplitude methods, respectively, because these choices minimized the RMS-weighted phase residuals. *S*-wave picks were downweighted by a factor of 0.5 to account for their greater uncertainty. The catalog includes only earthquakes located with a minimum of six picks of which at least two must be *P*-waves and two must be *S*-waves. Station corrections are included which were calculated iteratively to account for local structure beneath stations and systematic pick biases (see Table A1 in Appendix A). The catalog completeness is

comparable to manual catalogs obtained by student analysts [*Wilcock et al.*, 2009; *Hooft et al.*, 2010] (see Appendix A).

To estimate hypocentral uncertainties, *Hypoinverse* [*Klein*, 2002] requires a value for the 'picking' error, σ, of a *P*-wave arrival. This accounts for all sources of error including the errors in reading the onset of arrivals, clock errors and errors arising from modeling travel times using a simplified one-dimensional velocity model and a flat datum. Following [*Sohn et al.*, 1998a] I calculate this value according to:

$$\sigma^2 = \frac{\sum_{i=1}^{n}\sum_{j=1}^{m_i} w_{i,j}^2 \Delta t_{i,j}^2}{\sum_{i=1}^{n}(m_i - p)} \tag{1}$$

where w is the weight assigned to an arrival (the product of the pick weight, phase weight and any down-weighting applied by *Hypoinverse*), Δt is the travel time residual, m is the number of arrival time observations for a particular earthquake, n is the number of earthquakes, p is the number of free parameters being solved for, and i and j are indices of the earthquake and arrival time observation, respectively. A value of 95 ms is obtained for the full catalog, which likely reflects the strong velocity heterogeneity in the region [*Weekly et al.*, 2011].

Seismic moments are calculated using attenuation-corrected *P*- and *S*-wave spectral amplitudes [*Brune*, 1970; *Hanks and Wyss*, 1972], following the methods and values developed for previous MOR earthquake studies [*Tréhu and Solomon*, 1983; *Toomey et al.*, 1988; *Wilcock et al.*, 2002; *Hooft et al.*, 2010]. The seismic moment (M_o) for each *P*- or *S*-wave arrival on a station is given by:

$$M_O = \frac{4\pi\rho x c^3 \Omega_0}{KR} \tag{2}$$

where ρ is the rock density at the hypocentral source, x is the epicentral distance to the

earthquake, c is seismic wave speed, Ω_0 is the spectral amplitude in the 4-10 Hz frequency band corrected for attenuation, K represents a free-surface correction, and R is a radiation pattern factor. The parameter values based on *Toomey et al.* [1985] are shown in Table 2. The seismic moment for an earthquake is equal to the average of the median values of M_o for *P*-waves and for *S*-waves.

Seismic moment is converted to moment magnitude (M_W) after *Hanks and Kanamori* [1979],

$$M_W = \frac{2}{3}\log_{10} M_O - 10.7 \tag{3}$$

This relationship is used to plot the logarithm of the cumulative number of earthquakes above a certain magnitude as a function of magnitude for various regions and time intervals. The *b*-value and its uncertainty are calculated using the method outlined by *Wiemer and Wyss* [2002]. For a range of completeness magnitudes, this method determines the goodness-of-fit between the observed frequency-magnitude distribution and a synthetic distribution predicted by the maximum likelihood solution. The *b*-value is determined from the minimum completeness magnitude, M_C; I take the *b*-value that corresponds to either the maximum of the goodness-of-fit or the first instance that the goodness-of-fit exceeds 0.9. Uncertainties in *b*-value are calculated following the method of *Shi and Bolt* [1982].

2.5 Results

The catalog comprises 36,523 earthquakes occurring between August 2003 and October 2006 along the Endeavour Segment and adjacent segments. Figure 3a shows a histogram of daily earthquake counts of regional (epicenter >3 km from all stations) and local earthquakes. During the deployment, two seismic swarms in January and February 2005 ruptured the northern

portion of Endeavour Segment and the adjacent southern extension of the West Valley Segment. Following the swarms, the average daily seismicity count decreases to ~12% of pre-swarm levels. Though the period between April and October 2005 is an interval of reduced network sensitivity due to two station failures and degraded data fidelity on two others (Table 1), the decrease is apparent at all magnitude thresholds. If the period between October 2005 and June 2006 is considered a better representation, the observed post-swarm seismicity levels still decrease substantially to ~17% of pre-swarm levels.

Figure 4 shows epicenters color-coded by origin times relative to the 2005 swarms and outlines six seismically active regions which I will refer to as West Valley (WV) which also includes the area around the Endeavour and East Heck seamounts; Northern Endeavour Segment (NES) including the area to the east of the ridge; SouthWest Endeavour Valley (SWEV) including the area immediately north of the network; the Vent Fields (VF); the Cobb Overlapping spreading center and Southern Endeavour segment (COSE); and the Northern Symmetric Segment (NSS). Figure 3b shows the moment release for the full catalog. Except for a magnitude 5.4 earthquake on November 19, 2005 that is located in West Valley to the north of most of the seismicity in the catalog, nearly all the moment release occurs within the six geographic regions.

Median formal location uncertainties for each region were calculated with *Hypoinverse* for subsets of earthquakes with at least ten arrivals and are listed in Table 3. Within the network, the median maximum horizontal and median vertical uncertainties are 0.5 km and 0.8 km, respectively. Outside the network where the depth is fixed, the maximum 1-σ horizontal uncertainty tends to be tangential to the network and ranges from ~1 km in the southern portion of SWEV to 4-5 km at the segment ends. In the radial direction the formal horizontal location

uncertainties are significantly smaller. However, these uncertainties do not include contributions from uncertainties in the ratio of V_P/V_S [*Hooft et al.*, 2010]. An uncertainty of 5% in V_P/V_S leads to an additional uncertainty in the radial direction that is ~12% of the distance to an event. As a result total uncertainties in the radial and tangential directions are similar. It also should be noted that none of the uncertainties include the effect of systematic errors arising from crustal velocity heterogeneity which is quite significant in this region [*Weekly et al.*, 2011]. To first order, such errors will not affect the pattern of epicenters in a given region but they may substantially offset distant epicenters from their true location.

2.5.1 Northern seismicity

Figure 5 shows the distribution of epicenters, histograms of earthquake occurrence, moment release curves, and *b*-value plots for earthquakes to the north of the network in the WV, NES and SWEV regions. To allow comparisons of moment release between regions, the moment release curves for each region are also shown in Figure 3b-c. The cumulative moment releases totaled 1 x 10^{23} dyne-cm, 2 x 10^{23} dyne-cm, and 2 x 10^{24} dyne-cm for the WV, NES and SWEV, respectively, with the majority of seismic energy released during the January and February 2005 swarms (Figure 3b-c). Prior to the 2005 swarms, the histograms of daily earthquake counts and the small step-like increases in the cumulative moment release rates (Figures 5b-d) indicate that smaller swarms typically occurred every few months in each region, lasted 1-2 days, and comprised up to ~100 earthquakes (Figures 5b-d). There were several swarms in WV between April and June 2004 (Figure 5b), a swarm in NES in June 2004 (Figure 5c) and another in SWEV and NES on October 5, 2004 that was large enough to be detected by SOSUS (http://www.pmel.noaa.gov/vents/acoustics/seismicity/nepac/endeav1004.html) (Figures

5b-c). Starting roughly coincident with this swarm on October 5, 2004, seismicity rates progressively ramp up over several months preceding the 2005 swarm sequences mainly in the WV and NES (Figure 5b-c).

Figure 6 shows the distribution of epicenters for the October 5, 2004; January 2005 and February 2005 swarms color coded by time. The October 5, 2004 swarm (Figure 6a) includes ~250 earthquakes that occurred in two locations, the NES about 20-30 km north of the network and SWEV about 5 km north of the network. The net seismic moment release was 1.8×10^{22} dyne-cm with 65% released in the NES. Seismicity commenced early on October 5 at both locations and lasted for 2 days with no resolved spatial migration of epicenters.

The swarms in January and February 2005 included activity in multiple regions (Figure 6b-c). The January swarm lasted from January 31 through February 13 and included ~2,000 earthquakes. The net seismic moment release was 4.0×10^{22} dyne-cm with the NES, WV, and SWEV contributing 55%, 30% and 15%, respectively (Figure 5b-d). At the swarm onset, earthquakes concentrated ~5 km west of the northern Endeavour Segment near Endeavour Seamount (Figure 6b). The rates of seismicity increased markedly on February 3 and the focus of earthquakes on the color-coded plot appears to move towards the southeast over 2-3 days. This is confirmed by a plot of earthquake longitude versus time (Figure 7a), which shows that location of the most intense seismicity, but not its onset, moved east at a rate of 0.4 km/hr. While there may be large systematic offsets in locations at this distance from the network, this temporal trend cannot be attributed to location error. Activity persisted in the NES and WV regions for the remainder of the swarm.

Activity in SWEV on the southern extension of the West Valley Segment commenced on February 5, six days after the swarm started (Figure 6b). The catalog does not discern a clear

migration direction for the initial epicenters in this region, although the locus of most intense seismicity jumped 5-10 km southward on February 6 (Figure 7b) where it was sustained within a ~5 km^2 area for the remainder of the swarm. On February 11, an intense cluster of earthquakes migrated about 2 km south over 12 hours at 0.15 km/hr (Figure 7b).

The second, larger February swarm occurred over ~23 days between February 22 and March 16 and was first analyzed by *Hooft et al.* [2010]. While the earthquakes occurred in roughly the same regions as the January swarm, the seismicity patterns differ significantly. For this swarm, the catalog includes ~5,000 earthquakes and the total moment release was 2.3 x 10^{24} dyne-cm with >90% released in the SWEV region (Figure 5c). Because earthquakes in the NES and SWEV merge for this swarm, I divide them for the purposes of the migration analysis using a boundary approximately midway between the Endeavour spreading axis and West Valley propagator (Figure 6c). The earliest seismic activity is located within the WV and NES (Figure 6c). Seismicity rates increased in NES on February 25 and spiked again on February 27 (Figure 7c), the onset of the main swarm as identified by *Hooft et al.* [2010]. Additional clusters of seismicity occurred progressively further southward on February 28, March 1, and March 2 (Figure 7c). Overall the seismicity migrates about 20 km south at ~0.25 km/hr. If this seismicity is located on the Endeavour ridge axis, then the epicenters further to the north may be systematically offset ~10 km to the east.

Earthquakes within the SWEV commenced ~6 hours after the onset of the February 27 activity in NES. The data shows that the onset of SWEV seismicity migrated rapidly 20-25 km to the south over 10 hours at a rate of 2 km/hr (Figure 7d) from the tip of the WV propagator toward the western abyssal ridge. On February 28 and March 1, the six largest earthquakes occurred in this region. They have strike-slip focal mechanisms that require either right-lateral

motion on N-S trending faults or left-lateral motion on E-W trending faults. Over several days, the focus of the most intense seismicity in the SWEV migrated ~10 km to the south and southeast where it merged with the southward migrating earthquakes on the NES around March 3 (Figure 6c). After March 8 the epicenters appear to branch into several distinct north-south linear trends at latitudes between 48˚04' N and 48˚02' N with the easternmost earthquakes about 5 km north of the Sasquatch vent fields; this is also the area where the October 2004 SWEV activity was located (Figure 4).

The rate of seismicity decayed steadily during the period March 10-15. Following the end of the February swarm, seismicity in WV returns to pre-swarm levels and nearly ceases in NES (Figure 5a-b). In SWEV, seismicity continues at moment release rates that are about half the pre-October 2004 levels in an east-west band that extends from the ridge axis a few kilometers north of the network to about 15 km to the west (Figure 4).

For WV, SWEV and NES, pre-swarm *b*-values (Figures 6e-g) are similar for all three regions (~2). During the January and February 2005 swarms, the *b*-values for the WV and NES regions decrease moderately to a value of 1.6 while the SWEV *b*-value decreases substantially to 1.2. The *b*-value for WV remained at a value of 1.6 while the *b*-value for SWEV rebounded to 1.9, comparable to the pre-swarm value. Calculating a post-swarm *b*-value for the NES region was infeasible since very few earthquakes were located in the region during this time.

2.5.2 Vent field seismicity

The cumulative moment release in the VF region is 6.9 x 10^{21} dyne-cm, substantially lower than in other regions (Figure 3c). Between August 2003 and September 2004, an average of 9 events/day were located, all with magnitudes less than ~2.5. The most intense seismic

activity (Figure 8a) is between the High Rise and Main Endeavour fields extending up to 1 km south of the Main Endeavour field with a smaller cluster of seismicity near Mothra field. The depths of VF earthquakes (Figure 9) are consistent with a ~1-km-thick band of seismicity directly overlying the AMC [*Wilcock et al.*, 2002; *Tolstoy et al.*, 2008; *Wilcock et al.*, 2009].

The rate of seismicity decreased by 60% during fall 2004 (Figures 8b), approximately a month prior to the October 5 swarm in NES and SWEV. During the January and February 2005 swarms, seismicity within the VF region increased starting 1-2 days after the swarm onsets (Figure 5d and 8b). Peak daily seismicity counts are ~100 and ~200 events/day for the January and February swarms, respectively. The swarms account for about 50% of the total moment release in the region and include earthquakes with magnitudes up to 2.8. Seismicity during the January swarm located primarily between the High Rise and Salty Dawg fields while earthquakes were concentrated farther south between the Main Endeavour and High Rise fields during the February swarm (Figures 8 and 9). During the swarms, the earthquakes also tend to locate at shallower depths (Figure 9). Because the network was significantly degraded during the swarms (Table 1) and *Hypoinverse* sometimes preferentially locates earthquakes near particular layer interfaces, the clustering of locations near 1.2 km depth may be an artifact of the location algorithm.

Following the swarms, the rate of seismicity decreased to ~15% of pre-swarm values and maximum earthquake magnitudes were ~2.2. The highest concentration of earthquakes is to the south of the Main Endeavour field with additional clusters between High Rise and Main Endeavour and near Mothra, similar to pre-swarm patterns (Figure 8a). Seismic *b*-values within the region were 1.7 both before and after the swarms, dropping to 1.4 during the swarms (Figure 8c).

2.5.3 Southern seismicity

Seismicity located south of the Keck network (Figure 10a) was primarily associated with deformation in the Cobb OSC (COSE) and on the Northern Symmetric Segment (NSS). The cumulative seismic moment release for the COSE and NSS totaled 1.9 x 10^{22} and 5.2 x 10^{22} dyne-cm, respectively. Swarms lead to a step-like pattern of observed moment release because a large number of earthquakes are recorded within a short amount of time (Figure 10b-c). There is an indication that there may be large systematic location errors due to velocity heterogeneity; if earthquakes on the NSS are centered on the spreading center, the COSE and NSS earthquakes may be mislocated on average 10-15 km too far west.

Prior to the 2005 swarms, the average rate of seismicity in each region was 3-4 events/day. Following the swarms, the earthquake rates in NSS were unchanged but the COSE region entered a sustained period of seismic quiescence with only a handful of earthquakes located over 18 months (Figure 10b). Thus, while seismicity on the south Endeavour segment almost ceased, the Northern Symmetric Segment was unaffected. The *b*-values in the two regions were ~2 before the swarm and do not change significantly in the NSS afterwards.

2.6 Discussion

2.6.1 The 2005 swarms

A key question for understanding the January and February 2005 swarms is the relative roles of tectonic and volcanic processes. The swarms exhibited complicated rupture patterns with seismicity occurring throughout a broad region encompassing the WV, SWEV, NES and VF regions (Figure 6b-c) and appear to be closely linked based on the similar distributions of

seismicity along the northern Endeavour segment and the southern extension of the West Valley segment. The seismic moment release of the February swarm is nearly two orders of magnitude larger than the January swarm. However, the magnitude of the pressure anomalies measured at regional boreholes show that the majority of the moment release was aseismic [*Hooft et al.*, 2010]; the pressure anomalies associated with the February swarm are only about twice those for the January swarm suggesting that the aseismic moment releases are more similar (E.E. Davis, personal communication). The borehole pressure data [*Hooft et al.*, 2010] and some of the characteristics of seismicity including the lack of main shocks, *b*-values that are always significantly greater than unity and the migration of epicenters are consistent with a magmatic swarm. However, other characteristics such as the band of epicenters striking oblique to the northern Endeavour during the January 2005 swarm, the strike-slip focal mechanisms within the Endeavour-West Valley OSC during the January 2005 swarm and the decrease in *b*-values observed in several regions are difficult to attribute to magmatic processes and suggest a tectonic component.

The onset of the January swarm on January 31 is marked by earthquakes in the Endeavour – West Valley OSC near the vicinity of Endeavour Seamount. Over 2-3 days, epicenters in the NES region migrated 20 km southeast along a trend oblique to the Endeavour ridge (Figure 6b). Although this trend appears to extend well east of the ridge axis onto the Juan de Fuca plate, the epicenters in this region may be systematically displaced to the east. The curious migration pattern does not correlate with any trends in seafloor morphology and is inconsistent with propagation of a dike along the northern Endeavour Segment. One explanation is that the trend could be due to shear deformation associated with reorganization of the Pacific-Juan de Fuca-Explorer plate boundary. Specifically, from an analysis of regional bathymetry,

the distribution of epicenters from SOSUS and focal mechanisms from the Canadian National Seismograph Network, *Dziak* [2006] argues that the Heck, Heckle and possibly Springfield seamount chains overlie splays of a broad southward migrating Sovanco transform fault that provide conduits for seafloor volcanism. The observed earthquakes align with the eastward extension of the Heck seamount chain and could indicate strike-slip motion along this splay.

Seismicity in the SWEV initiated 4 days after the NES on February 5. The epicenters extend ~15 km along the N-S trend of the West Valley propagator with most of the seismicity concentrated at the southern end of the Endeavour Valley (Figure 6b) well to the south of the bathymetric expression of the propagator. No clear along-axis migration of epicenters is resolved (Figure 7b) except for a short episode of seismicity near the end of the swarm. Thus, the earthquake epicenters alone do not provide conclusive evidence for a volcanic source. However for this swarm the borehole pressure data (E.E. Davis, personal communication) suggest that nearly all the moment release is aseismic and the characteristics of the pressure anomalies require a coseismic strain that was substantially different from the June 1999 [*Davis et al.*, 2001] and February 2005 swarms [*Hooft et al.*, 2010]. Rather than decreasing, the pressures to the north in Middle Valley increased indicating reduced pore volume. On the western ridge flanks the pressures also increased but the relative amplitude was markedly less than for the other swarms. This pattern of pressure anomalies may be compatible with the injection of a northwest-southeast oriented dike near the southern tip of the West Valley Segment (E.E. Davis, personal communication). Southward growth of the West Valley propagator beyond the region in which it has a bathymetric expression is consistent with models for the evolution of the Endeavour-West Valley OSC that predict the eventual truncation of the Endeavour Segment [*Karsten et al.*, 1990].

The February swarm was analyzed previously by *Hooft et al.* [2010]. Although the majority of the seismic moment release was within the SWEV region, the swarm initiated in the NES. From the pattern and timing of borehole pressure anomalies and their similarity to the 1999 swarm, *Hooft et al.* [2010] infer the swarm was linked to a dike injection on the NES. The NES earthquakes locate significantly to the east of the spreading axis but the locations may be biased by large velocity heterogeneities within the region [*Weekly et al.*, 2011]. *Hooft et al.* [2010] did not resolve migration of the onset of seismicity in the NES but found that the seismicity switched off from north to south. Unlike *Hooft et al.* [2010] who subdivided the earthquakes into rectangular regions similar to those shown in Figure 4, I subdivide the earthquakes in the February swarm by their proximity to the Endeavour segment and the West Valley propagator (Figure 6c). Earthquakes closest to the Endeavour segment are concentrated in bursts that migrate unsteadily 30 km south over about 3 days (Figure 7c). This migration of earthquakes supports the inference that the February swarm was associated with a dike on the NES [*Hooft et al.*, 2010] although it suggests that the pattern of injection was complex. The overall migration rate is lower than observed for eruptive events [*Dziak et al.*, 2007]. The north to south migration direction is inconsistent with a dike sourced from the AMC associated with the elevated central portion of the Endeavour Segment [*Van Ark et al.*, 2007] and could be interpreted as evidence of a tectonic cause. Alternatively, a southward propagating diking event on the northern Endeavour could have been sourced from the north by magma associated with the Heck Seamounts [*Dziak*, 2006], and specifically the Endeavour Seamount, which lies at the northern end of the Endeavour – West Valley OSC (Figure 1). For this interpretation, one can speculate that the southeast striking band of epicenters in the January swarm may have been associated with fault-controlled melt supply from the Endeavour Seamount to the northern

Endeavour segment.

Hooft et al. [2010] resolved a southward migration of epicenters on the SWEV starting 11 hours after the initiation of the main swarm on the NES on February 11. Using this division of earthquakes, seismicity on the West Valley propagator initiates about 6 hours after the NES, somewhat earlier than reported by *Hooft et al.* [2010]. The onset of seismicity migrates ~20 km south at about 2 km/hr (Figure 7d), much faster than the speed of ~0.6 km/hr reported by *Hooft et al.* [2010]. This migration rate is consistent with observations for eruptive diking events at mid-ocean ridges [*Dziak et al.*, 2007] but an event response cruise found no evidence for an eruption (http://www.pmel.noaa.gov/vents/acoustics/seismicity/nepac/endeav0205/response-cruise.html). *Hooft et al.* [2010] argue that the borehole pressure data is inconsistent with a strain field created by a northwest-southeast oriented dike in the SWEV. However, this inference does not preclude a diking event on the West Valley propagator, but rather requires that the pressure signal be dominated by a larger event on the northern Endeavour segment.

The six largest events of the swarm occurred in SWEV on February 28 and March 1 and the swarm continued in this region for about 2 weeks. The presence of large earthquakes is reflected in the low *b*-value of 1.3 observed during the swarm in this region (Figure 5g) and suggests an enhanced tectonic component. However, it is important to note that the focal mechanisms indicate a sense of strike-slip motion on ridge-perpendicular faults that is opposite to the offset of the OSC. *Hooft et al.* [2010] argue that these mechanisms might reflect reactivation of ridge-parallel strike-slip faults in the OSC in response to the stress changes induced by a dike intrusion on the northern Endeavour. During the second week, seismicity reached the southern end of the SWEV region (~48˚02'N) and earthquakes appear to cluster into several distinct north-south lineations spaced 2-3 km apart that may correlate with seafloor

topographic features. The slow epicentral migration to the south and southeast, oscillatory seismic rate [*Hooft et al.*, 2010], lack of aftershock activity, and a possible correlation to seafloor volcanic features suggests that this seismicity could be associated with magma bodies that extend across the OSC as observed on the East Pacific Rise at 9°03'N [*Kent et al.*, 2000; *Toomey et al.*, 2007]. The restoration of high *b*-values in the SWEV region following the swarm Figure 5g) is consistent with a volcanic influence. Alternatively, the observation that the SWEV region remains seismically active following the 2005 swarms (Figure 4) could be interpreted and indicative of a tectonic response to static stress changes.

In summary, the dominant signal in the borehole pressure records is a diking event on the northern Endeavour in late February [*Hooft et al.*, 2010] which I infer extends 20 km along axis from 48°15'N to 48°02'N (Figure 8c). The origin of the seismicity that trends oblique to the NES in the earlier January swarm is enigmatic and the interpretation of magma migration from under Endeavour Seamount is speculative. I infer that both swarms also involved intrusions beyond the tip of the West Valley propagator and that there was possibly additional magmatic activity elsewhere in the Endeavour Valley near the conclusion of the February swarm. The drop in *b*-values during the swarm, particularly in the SWEV region (Figure 5g), is surprising given the evidence for magmatic extension and suggests a tectonic component. Focal mechanisms of larger events determined from land-based networks (Figure 4 and 5) indicate east-west strike-slip motion, which is counter to the offset of the OSC.

The 2005 swarms are interpreted as the terminus of a 6-year spreading episode that started in 1999 and ruptured the Endeavour Segment. The 1999-2000 swarm sequence extended along the central and southern portions of the Endeavour segment from about 47˚40'N to 48˚05'N [*Bohnenstiehl et al.*, 2004]. The 1999 swarm was interpreted in terms of a 40-km-long

dike [*Davis et al.*, 2001] and the characteristics of earthquakes in the 2000 swarm are consistent with a deeper intrusion although a tectonic cause is also possible [*Bohnenstiehl et al.*, 2004]. The combination of diking events in 1999, 2005 and possibly 2000 appears to have ruptured the majority of the Endeavour segment from about 47˚40'N to 48˚15'N. Following the February 2005 swarm, seismicity essentially ceased at the ends of the segment and decreased substantially in SWEV and VF regions (Figure 4) suggesting that extensional stresses have been relieved along the entire segment.

2.6.2 Comparison with other magmatic spreading events

SOSUS monitoring has provided a 20-year record of seismic swarms on the Juan de Fuca and Gorda ridge including those associated with eruptive (1993 on CoAxial [*Dziak et al.*, 1995], 1996 on the Gorda Ridge [*Fox and Dziak*, 1998] and 1998 on Axial Seamount [*Dziak and Fox*, 1999b]) as well as many non-eruptive spreading events. A synthesis of the observations [*Dziak et al.*, 2007] suggests that eruptive events are characterized by an early onset of earthquake migration and faster migration rates. It is thought that higher excess magma pressure is required for eruptions, most likely because of magma recharge into crustal magma bodies prior to the eruption. At the detection threshold of SOSUS, the February 2005 Endeavour swarm fits this model; the speed of migration of 0.2 km/hr and onset after 72 hours compare with speeds of 1-2 km/hr and onset times <1 day for the eruptive events [*Dziak et al.*, 2007]. However, the local network data presents a more nuanced picture. In the presence of substantial precursory activity, the onset time of a swarm is somewhat subjective. While earthquakes on the northern Endeavour only migrate southward at 0.25 km/hr, there is fast migration at ~2km/hr on the West Valley propagator (Figure 7d) within hours of the onset of the main swarm.

From a theoretical standpoint it is not clear why eruptive and intrusive diking events should always have distinct seismic characteristics. *Buck et al.* [1997] explain the difference between eruptive and non-eruptive events in terms of the relative values of the overburden pressure at the AMC and the pressure at the base of a column of erupting magma. In this model, the thickness of low-density extrusives at any particular site will be self-regulating so that the average density of the upper crust matches that of the least dense erupting lavas. The difference between eruptive and non-eruptive events may reflect small changes in the composition and volatile content of the magma and in average upper crustal densities rather than profound difference in characteristics of dike intrusion.

In comparison with the eruptive events observed along the Juan de Fuca ridge, the pattern of seismicity for the 2005 Endeavour swarm is complex. The three diking-eruptive events [*Dziak et al.*, 1995; *Fox and Dziak*, 1998; *Dziak and Fox*, 1999b] were all characterized by seismicity focused in a single region that migrated down the gradient of the axial rift bathymetry on a timescale of ~2 days before decaying over several weeks. The duration of the two 2005 Endeavour swarms is similar but seismicity was detected in four regions. This complexity partly reflects the improved resolution of a local seismic network compared to SOSUS (most of the SOSUS locations for the February 2005 swarm were in SWEV [*Hooft et al.*, 2010]) but it also reflects the tectonics of the region and in particular the involvement of two limbs of the OSC. It is interesting to note that the 1999 Endeavour swarm on the central/southern Endeavour led to seismicity on Surveyor Volcano on the Northern Symmetric Segment, the opposing limb of the Cobb OSC. *Bohnenstiehl et al.* [2004] inferred that dynamic stresses triggered earthquakes on the opposing limb of the OSC.

The February 2005 swarm is unique in that the inferred dike on the northern Endeavour

migrates up the gradient of the axial valley towards the center of the segment. This differs from the three eruptive events and the non-eruptive events on the Endeavour in 1999 [*Bohnenstiehl et al.*, 2004] and Middle Valley in 2001 [*Davis et al.*, 2004]. It is also different from the magmatic diking sequences observed on land at Krafla from 1974-1984 [*Sigmundsson*, 2006] and in Afar from 2005-2009 [*Ebinger et al.*, 2010] which were both fed from a central magma body. This suggests that the source of magma for volcanism on Endeavour is more complex than the commonly accepted model in which magma is supplied to the crust at the center of the segment and the dikes migrate away from this source to the segment ends [e.g., *Macdonald*, 1998]. Given the presence of a large seamount in the Endeavour – West Valley OSC, it is plausible that the northern portion of the Endeavour segment might tap an alternate magma source. *Grandin et al.* [2012] argue that along-axis variations in the depth to the brittle-ductile transition plays a greater role than topography in horizontal dike propagation because thicker lithosphere can store more elastic strain energy. If the 1999/2000 events on the central/southern Endeavour depleted a magma reservoir at the center of the segment, the elastic potential energy stored in the crust to the north may have drawn magma from an alternative source.

If the 1999 – 2005 swarm sequence is considered as the magmatic phase of a single spreading cycle that ruptured the whole Endeavour segment, then the duration of the magmatic phase is substantially longer than other ridge-spreading events. The three eruptive events in the NE Pacific [*Dziak et al.*, 1995; *Fox and Dziak*, 1998; *Dziak and Fox*, 1999b] were limited to single eruptions lasting for days. On the East Pacific Rise at 9°50'N, isotopic dating of lava flows suggests that the eruptions in 1991 and 2005 extended over ~1 year [*Rubin et al.*, 1994] and ~6 months [*Rubin*, 2006], respectively. The timescales of the Endeavour event are more consistent with the observation of rifting on land where rifting episodes at Krafla Volcano,

Iceland and in Afar have lasted a decade and involve many dike intrusions along the same segment [*Sigmundsson*, 2006; *Ebinger et al.*, 2010]. These sequences can be explained in terms of the large extensional stresses required to rupture thick lithosphere; the resulting large extensional strains coupled with a limited crustal magma reservoir requires multiple diking episodes with magma recharge of the magma body in between to accommodate the strain [*Qin and Buck*, 2008]. At the Endeavour, the lithosphere is thin and each portion of the ridge experienced only one major dike injection, but the interval between the 1999 and 2005 events may well reflect a timescale of magma supply. The sharp drop off in seismicity following the 2005 swarms is consistent with observations on Axial Seamount [*Dziak and Fox*, 1999a] and the East Pacific Rise [*Tolstoy et al.*, 2006], which show a progressive ramp up in seismicity prior to eruptive events and a sharp decrease at their conclusion.

2.6.3 Precursory activity and triggering

The patterns of seismicity surrounding the 2005 Endeavour swarms suggest seismic triggering over length scales from <10 km to 50 km and at various timescales. During the swarms, the seismicity migrated between regions on timescales of hours to days. The long-term decrease in seismicity along the Endeavour Segment following the 2005 swarms occurred within days, or at most weeks. The spatial coincidence of earthquakes suggests that seismicity is linked between the two swarms on a timescale of one month. On a time scale of several months, the moment release rate in WV and NES gradually increases prior to the 2005 swarms starting with a small swarm on October 5, 2004. Finally, on a 6-year timescale, I infer that the 2005 swarms are linked to the 1999 and 2000 swarms that ruptured the Endeavour segment further south [*Bohnenstiehl et al.*, 2004].

Two mechanisms are invoked to explain remote earthquake triggering: coseismic changes to static Coulomb stresses [*Harris and Simpson*, 1992; *King et al.*, 1994; *Nostro et al.*, 1997; *Stein et al.*, 1997; *Hardebeck et al.*, 1998] and dynamic transient stresses induced by passing seismic waves [*Hill et al.*, 1993; *Kilb et al.*, 2000; *Gomberg et al.*, 2001; *Prejean et al.*, 2004; *Brodsky and Prejean*, 2005]. Static stress changes can either promote or retard seismic activity and operate over length scales of approximately three fault (or dike) lengths [*King et al.*, 1994] and timescales that can be quite long [*Freed*, 2005]. Dynamic triggering can operate over longer ranges but on short timescales. Surface waves from earthquakes located up to several thousand kilometers away have triggered increases in local seismicity in volcanic-hydrothermal systems on land [*Hill et al.*, 1993; *Prejean et al.*, 2004].

On the Endeavour Segment, *Bohnenstiehl et al*. [2004] argued that dynamic triggering during volcanic intrusive events plays a role in triggering seismicity at other locations on the ridge. While this interpretation cannot be discounted, I argue that static triggering could account for all the observations around for the 2005 swarms. To evaluate the feasibility of static triggering, it is necessary to know the pattern of deformation to determine whether regions of increased and decreased seismicity are consistent with the changes in the stress field from earlier events. Unfortunately, the detailed strain field associated with 2005 swarms is unknown, so it is not possible to quantify how static stresses linked active regions during the 2005 swarms. *Bohnenstiehl et al.* [2004] showed that the injection of the 1999 dike on the central Endeavour generated static stresses that reduced extensional stresses to either side but promoted extensional failure on the ridge axis to the south where the 2000 swarm occurred. The 1999 dike would also have generated extensional stresses on the ridge axis to the north that are consistent with the deformation inferred for NES in the February 2005 swarm [*Hooft et al.*, 2010].

A variety of post-seismic static stress transfer mechanisms can potentially explain the delay in triggered seismicity observed in the dataset. Viscoelastic relaxation involves transfer of elastic strain from the ductile lower crust and upper mantle to the brittle seismogenic upper crust. The characteristic timescale for the relaxation of a Maxwell solid is $2\mu/E$ where μ is the dynamic viscosity and E is Young's modulus [e.g., *Turcotte and Schubert*, 2002]. For an effective μ ranging from 10^{19} to 10^{21} Pa-s and $E = 10^{11}$ Pa, the characteristic times are ~ 1 to 100 years. Detailed modeling shows that the relaxation times are dependent on the vertical viscosity structure, the depth of brittle-ductile transition, the dip angle of the fault and the effective coefficient of fault friction [*Freed and Lin*, 1998; *Nostro et al.*, 2001; *Freed*, 2005]. *Freed and Lin* [2001] show that the 7-year delay between the 1992 Landers and 1999 Hector Mine earthquakes is consistent with lower crustal and upper mantle viscosities of 1.6×10^{19} Pa-s and 8×10^{18} Pa-s, respectively. Beneath mid-ocean ridges, upper mantle viscosities are commonly modeled as 10^{18}-10^{19} Pa-s [*Parmentier and Phipps Morgan*, 1990] but may either be higher at shallow depths due to dewatering [*Hirth and Kohlstedt*, 1996] or lower due to the presence of partial melt. The viscosities of hot and possibly partially molten lower crustal rocks are not well known but experimental constraints suggest values similar to the mantle [*Hirth et al.*, 1998]. Detailed modeling would be necessary to fully evaluate the timescales of viscoelastic relaxation in a mid-ocean ridge setting, but it is clearly a plausible mechanism to explain the time delay between the 1999-2000 swarms and 2005 swarms.

Poroelastic rebound occurs when the full static stress changes are not realized until pore fluids diffuse out of and into regions that experience volumetric compression and dilation respectively. The characteristic timescale for this process is given by D^2/η where D is the length scale and η the diffusion coefficient given by $\eta = k/\mu S$ with k the permeability, μ the fluid

viscosity and *S* the uniaxial storage compressibility [e.g., *Crone et al.*, 2010]. *Hooft et al.* [2010] model the increase in vent field seismicity observed ~2.5 days following the onset of the February 2005 swarm on the northern Endeavour in terms of along-axis diffusion of a hydrologic pressure perturbation. Using a characteristic diffusion length and time of 35 km and 2.5 days, respectively, they estimate a crustal permeability ~10^{-9} m^2. This value is high but consistent with permeability estimates for a sediment-capped layer 2A off-axis [*Davis et al.*, 2000]. Since there is no sediment cap on the ridge axis, pore fluid pressure perturbations are more likely to dissipate by vertical diffusion across the seafloor. The relatively shallow depths observed for the vent field seismicity during the swarms (Figure 9) are consistent with such an interpretation. Assuming the model parameters of *Crone et al.* [2010], reducing the diffusion length scale to 2 km yields a permeability of order 10^{-13} m^2 to 10^{-12} m^2 which matches estimates for ridge-axis hydrothermal fields [*Lowell and Germanovich*, 1994; *Wilcock and McNabb*, 1996; *Stroup et al.*, 2009; *Crone et al.*, 2011].

When evaluating whether poroelastic rebound can account for triggering timescales in the data, it is important to recognize that the permeability of ocean crust can vary by many orders of magnitude [e.g., *Fisher*, 1998] and that the partial sediment cover in the region may lead to variations in the diffusion length scales. If permeabilities range from 10^{-14} m^2 to 10^{-10} m^2 and the diffusion length scale from 2 to 10 km, the timescales obtained from the model of *Crone et al.* [2010] will range from ~1 hour to ~1 year. Given the wide range of feasible time scales, poroelastic rebound could explain large portion of the triggering observations.

Another mechanism that could account for a delay in triggering is the time required for pressure perturbations associated with the withdrawal or supply of magma to diffuse within and between magma systems. *Hooft et al.* [2010] argue that the characteristic diffusion timescale for

a pressure perturbation within the axial melt/partial mush zone would exceed the timescales for poroelastic diffusion because of the higher viscosity of the magma. However, this inference may be incorrect because magma may be less compressible than water [e.g., *Spera*, 2000] and the effective permeability of the melt region is unknown. Indeed, if magmatic pressure reductions are the cause of decreased seismicity following the 2005 swarm, the short timescale for the segment-wide cutoff might be cited as evidence for a magmatic system that is well connected along axis, either within the crustal AMC and mush zone or below the Moho where the melt fractions may be high [*Dunn et al.*, 2000].

2.7 Conclusions

In this paper I have presented a catalog of seismicity on the Endeavour Segment from 2003-2006 that is derived from a local seismic network. The primary conclusions are:

- Two regional seismic swarms, beginning in January and February 2005, were observed along the northern portion of the Endeavour Segment and within the adjacent Endeavour Valley. While they appear to have a tectonic component, I infer that these events were linked to intrusive volcanism, including diking on the Northern Endeavour during the February swarm and smaller dike intrusions on the propagating tip of the West Valley segment during both swarms.
- The seismicity associated with the 2005 swarms is more complex than that of other documented mid-ocean ridge spreading events. This likely reflects the complicated tectonics of the region and in particular the partition of magmatic spreading between two limbs of the Endeavour – West Valley OSC. The inference of a southward propagating dike on the northern Endeavour suggests that magma supply to the Endeavour may not be

limited to the central portion of the segment and could be associated with the Endeavour seamount melt source.

- Following the February 2005 swarm, the average seismicity rate along the Endeavour Segment decreased substantially with seismicity almost ceasing entirely at the ends of the segment. Seismic rates on the overlapping portions of the adjacent segments did not change. I infer that the swarms of January and February 2005 mark the termination of a 6-year non-eruptive spreading event that initiated with the June 1999 swarm and cumulatively ruptured and relieved stresses along the whole segment.
- The catalog shows extensive seismic triggering during the 2005 swarms at length scales of up to 50 km and timescales ranging from hours to years. While dynamic triggering may play a role, I argue that static triggering could account for all the observations with the timescale of delays influenced by the timescales of viscoelastic rebound, hydraulic diffusion, and magma withdrawal and replenishment.

Figure 1. (a) Bathymetric map of the Endeavour segment showing the Keck seismometer network (orange symbols) and high-temperature vent fields (yellow stars) on the central portion of the segment. Black lines show plate boundaries and the black box shows the area in Figure 1b. The inset figure shows the regional setting of the Endeavour segment at the northern end of the Juan de Fuca Ridge. (b) Bathymetric map of vent field area showing the seismometer network with station names labeled in italics and high temperature vent fields labeled in bold. The extent of the axial magma chamber [*Van Ark et al.*, 2007] is indicated by gray shadow. Bathymetry is from the Seabeam data set collected by the NOAA/VENTS program.

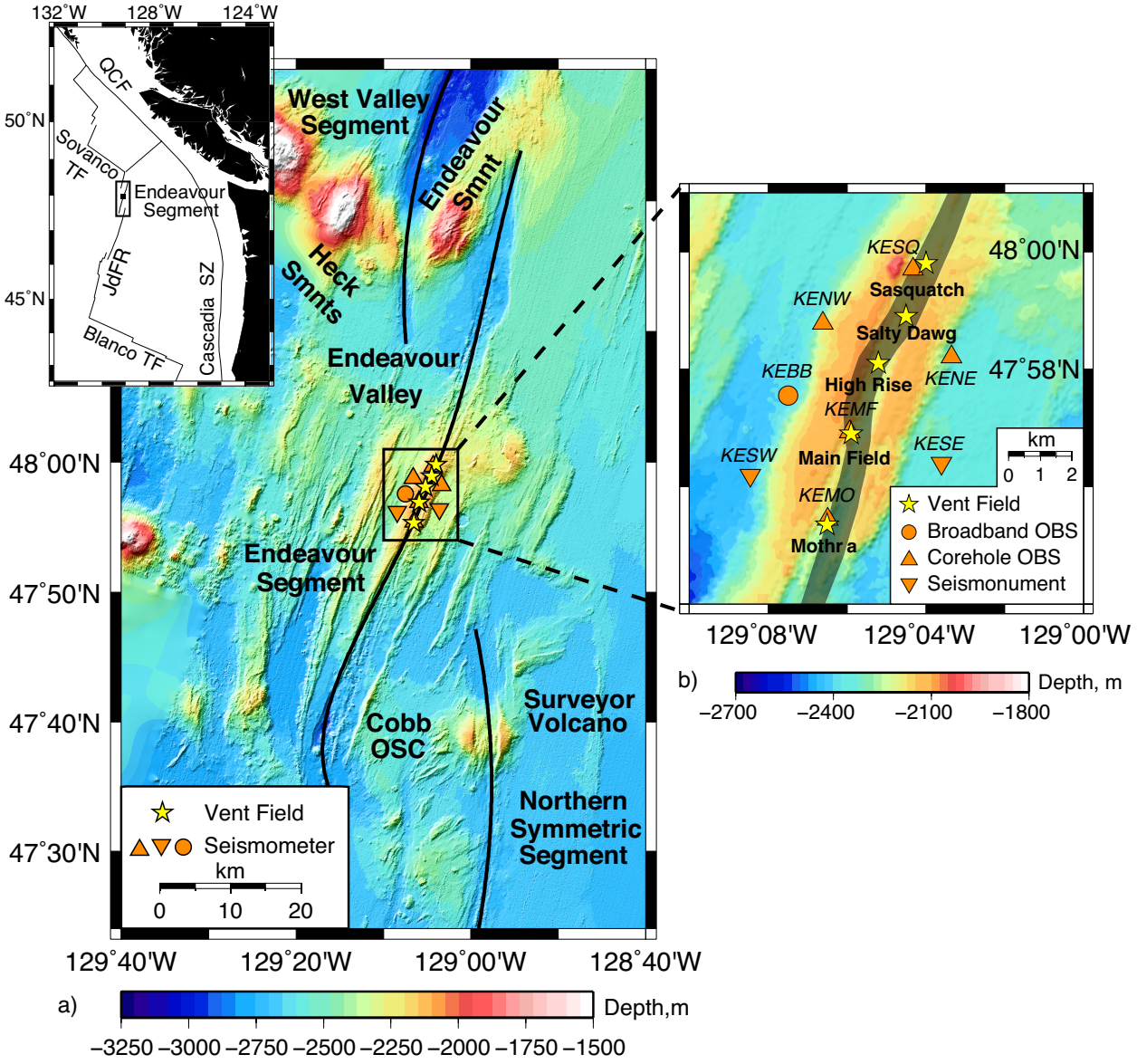

Figure 2. *P*- (red line) and *S*-wave (blue line) velocity models used for determining earthquake locations using *Hypoinverse* [*Klein*, 2002]. The *P*-wave model is derived from a previous refraction experiment [*Cudrak and Clowes*, 1993] while the *S*-wave model is derived assuming V_P/V_S = 3.0 above 0.4 km and V_P/V_S = 1.72 below 0.4 km [*Wilcock et al.*, 2009].

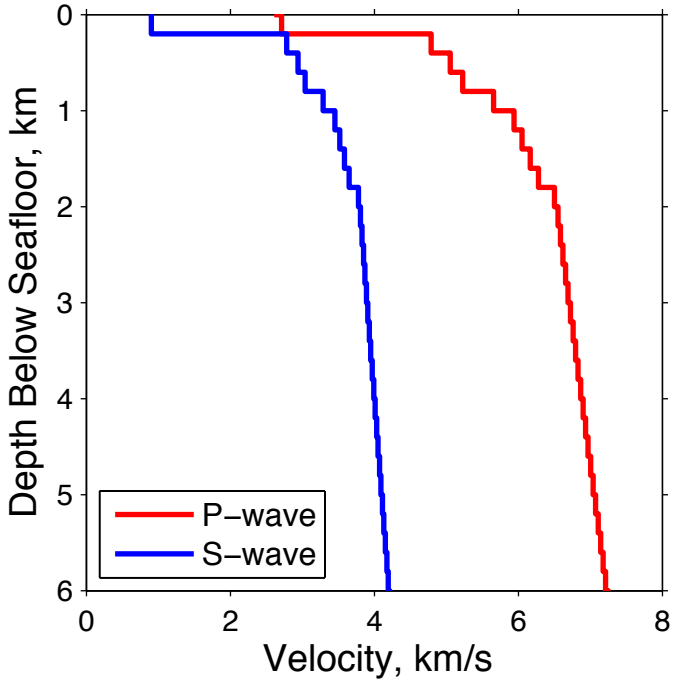

Figure 3. (a) Histogram of daily earthquake counts between August 2003 and October 2006. Local earthquakes located within 3 km of the nearest station are shaded green while regional earthquakes located further away are shown in blue. Note that the maximum rate for the February 2005 swarm has been clipped at 500 events/day but peak activity exceeds 1,000 events/day. The dashed black lines show the onset times for the October 2004, January 2005, and February 2005 swarms discussed in the text. (b) The cumulative moment release rate for the entire catalog (black), SWEV (red) and for the five other regions combined. (c) Cumulative moment release rates for all regions except the SWEV.

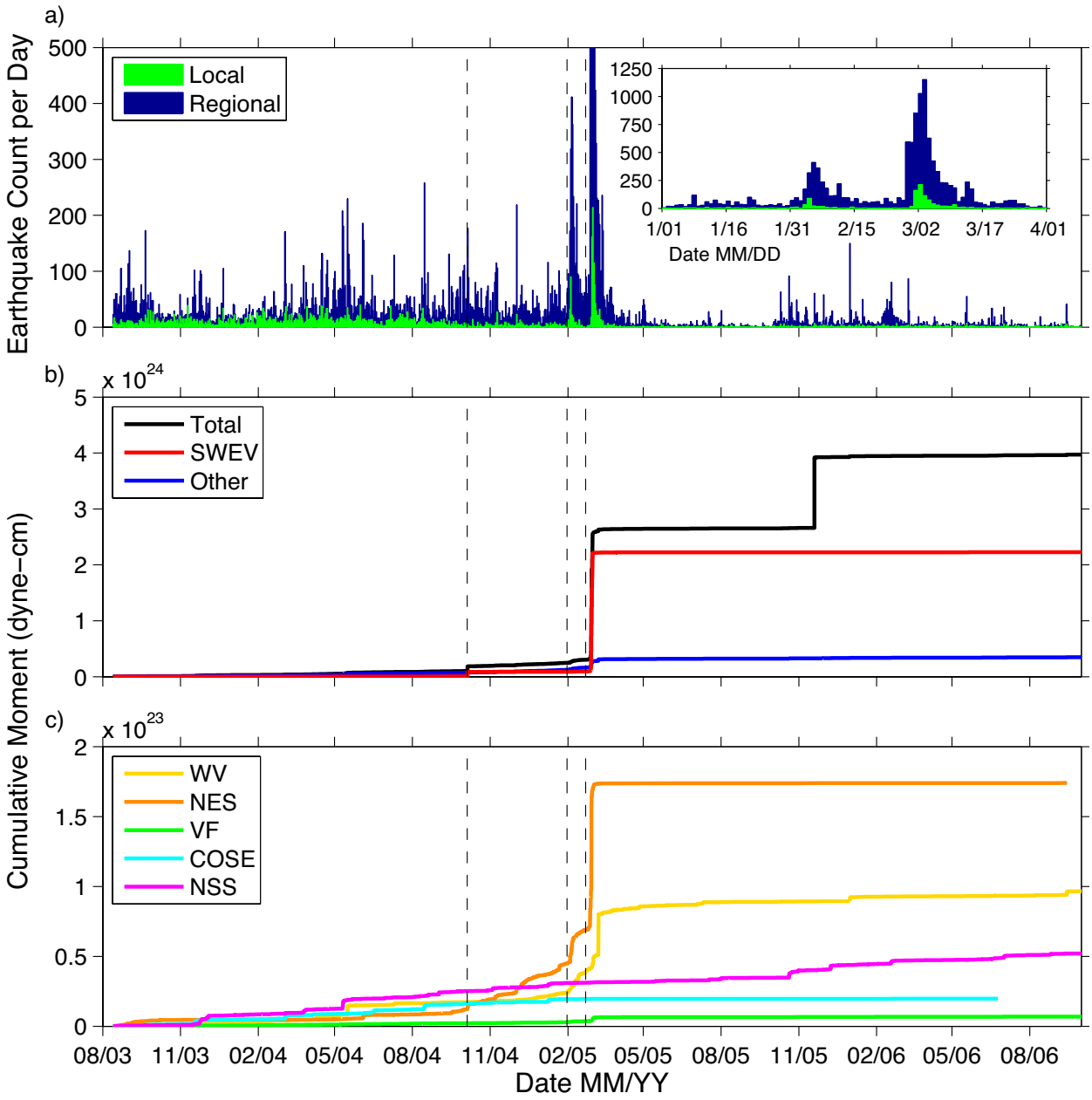

Figure 4. Segment-scale bathymetric map showing epicenters of 27,066 earthquakes located with at least 8 total arrivals. Colors indicate the time periods prior to the 2005 swarms (green), during the January 2005 swarm (violet), during the February 2005 swarm (blue), and following the swarms (red). Dashed white ellipses indicate seismically active areas associated with the October 5, 2004 swarm. The labeled boxes show the six regions of seismicity discussed in the text. For the purpose of assessing location errors, the SWEV has been further subdivided by the white dashed line into northern and southern regions. Focal mechanisms are shown for 6 large earthquakes in the February 2005 swarm analyzed by the Canadian National Seismograph Network. A cross near the northern edge of the map shows the location of a magnitude 5.4 earthquake on November 19, 2005 that is apparent in the cumulative moment release curve for the catalog (Figure 3b). Note that seismic activity occurring earlier in the deployment, particularly the portion of the January 2005 swarm located within the SWEV, is partially obscured by the February 2005 swarm.

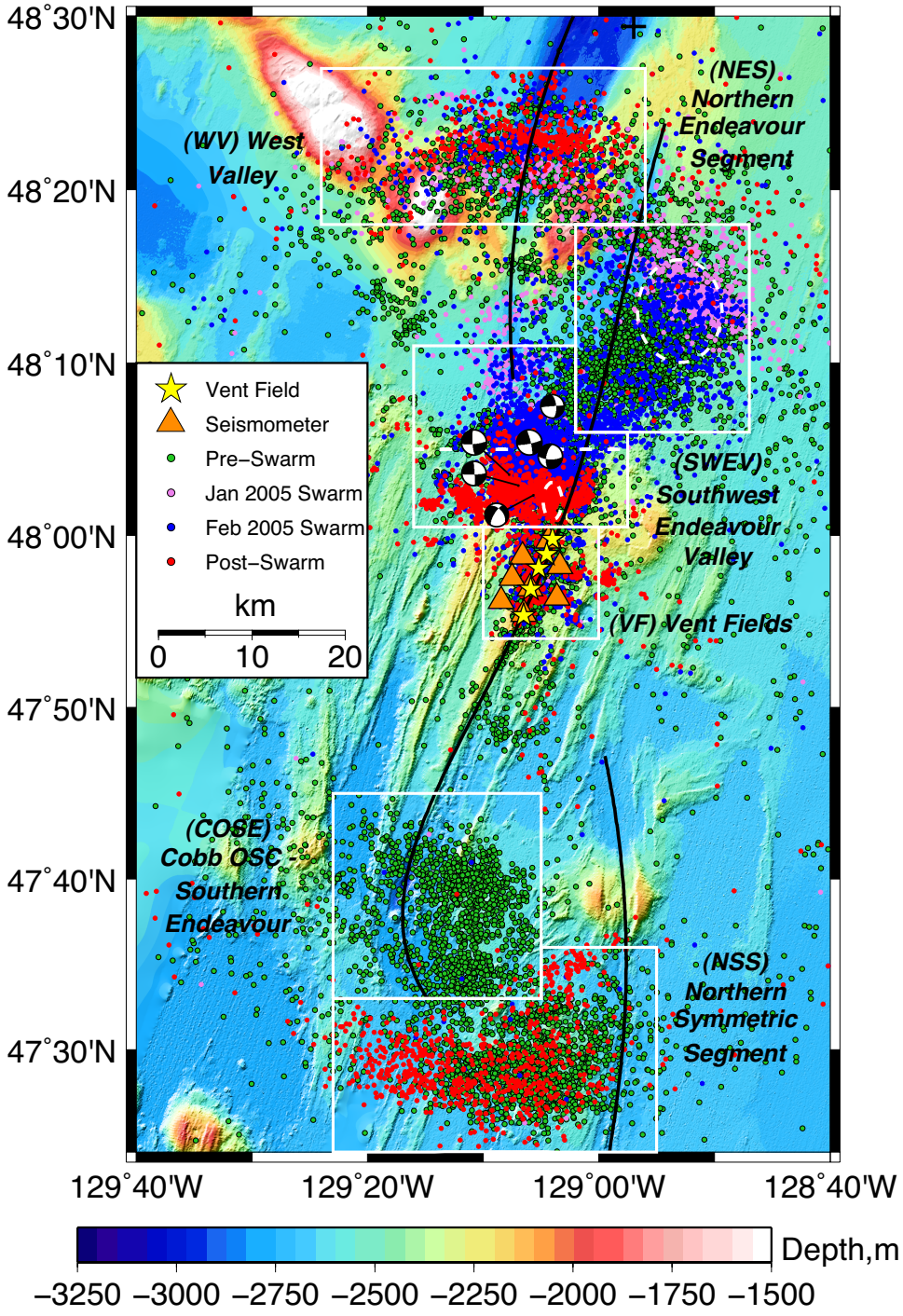

Figure 5. Seismicity within the northern regions. (a) Grayscale bathymetry overlain with earthquakes color-coded as in Figure 4. Median 1-σ location uncertainty ellipses are shown for the WV, NES and northern and southern portions of the SWEV region (delineated by a dashed white line) and include both formal location errors from *Hypoinverse* and an estimate of the uncertainty resulting from incomplete knowledge of the V_P/V_S ratio. (b-d) Histograms showing the daily counts of earthquakes and moment release curves for the (b) WV, (c) NES, and (d) SWEV. Note that different vertical scales are used for each plot. Vertical dashed lines show the onset times of the October 5, 2004 and January and February 2005 swarms. (e-g) Plots of earthquake count versus magnitude threshold for (e) WV, (f) NES, and (g) SWEV for the periods before (green), during (blue) and after (red) the 2005 swarms. The *b*-values and 2-σ uncertainties are labeled on the plots and dashed lines show magnitude of completeness. To directly compare *b*-values for pre- and post-swarm periods, a single value for the magnitude of completeness was chosen (dashed black lines) while a separate magnitude of completeness was chosen to calculate *b*-value for the swarms (dashed blue line).

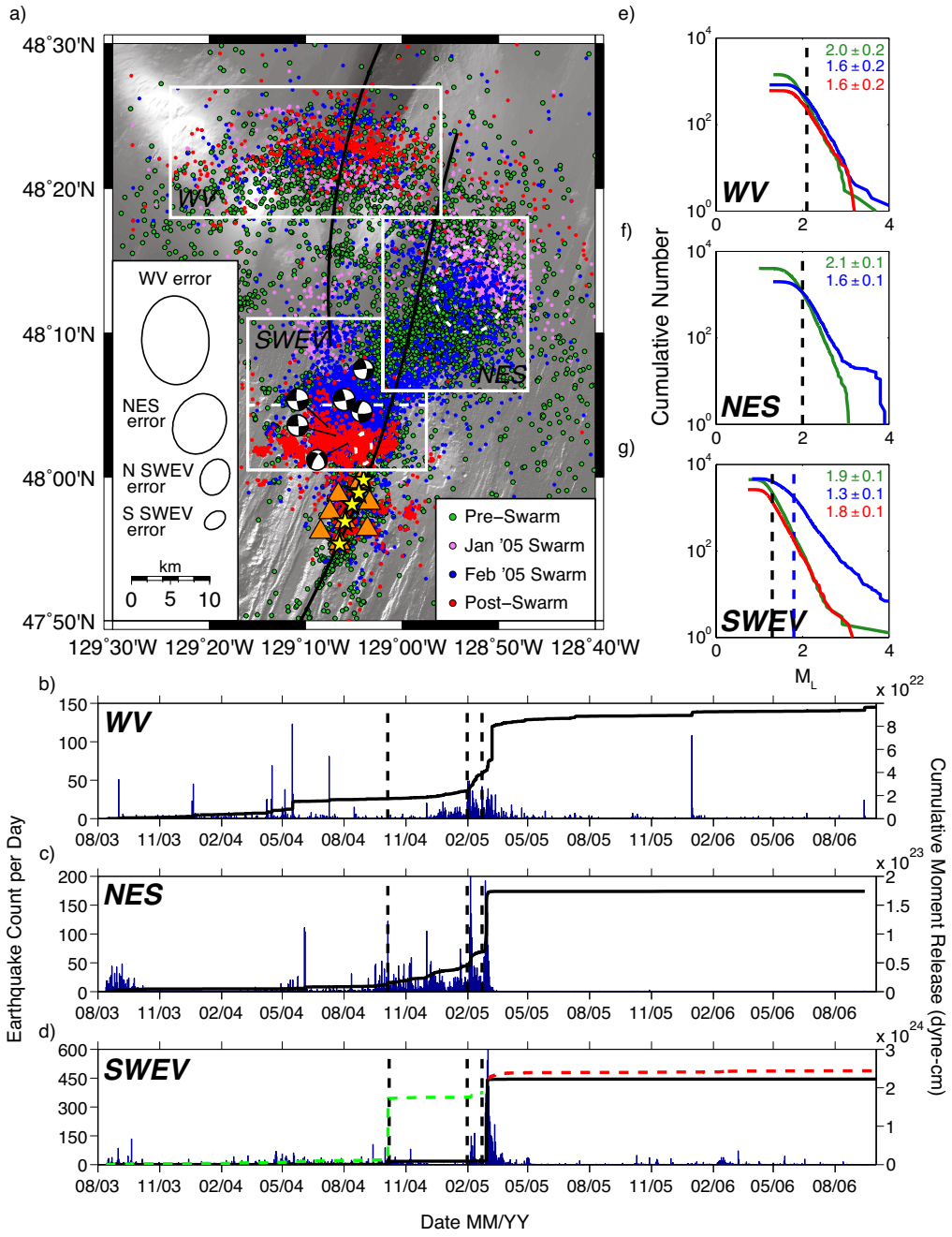

Figure 6. Gray scale bathymetric map showing epicenters (colored dots) located along the Endeavour and West Valley segments (solid black lines) during the (a) October 5, 2004, (b) January 2005 and (c) February 2005 swarms. The color of the epicenters indicates the calendar day as shown in the color bars; cooler colors show earthquakes that occurred later in the respective swarm. Note the difference in duration of each swarm. All earthquakes that satisfied the minimum location criteria of six arrivals are shown. White dashed lines delineate the regions used to analyze the migration patterns of earthquakes as shown in Figure 7.

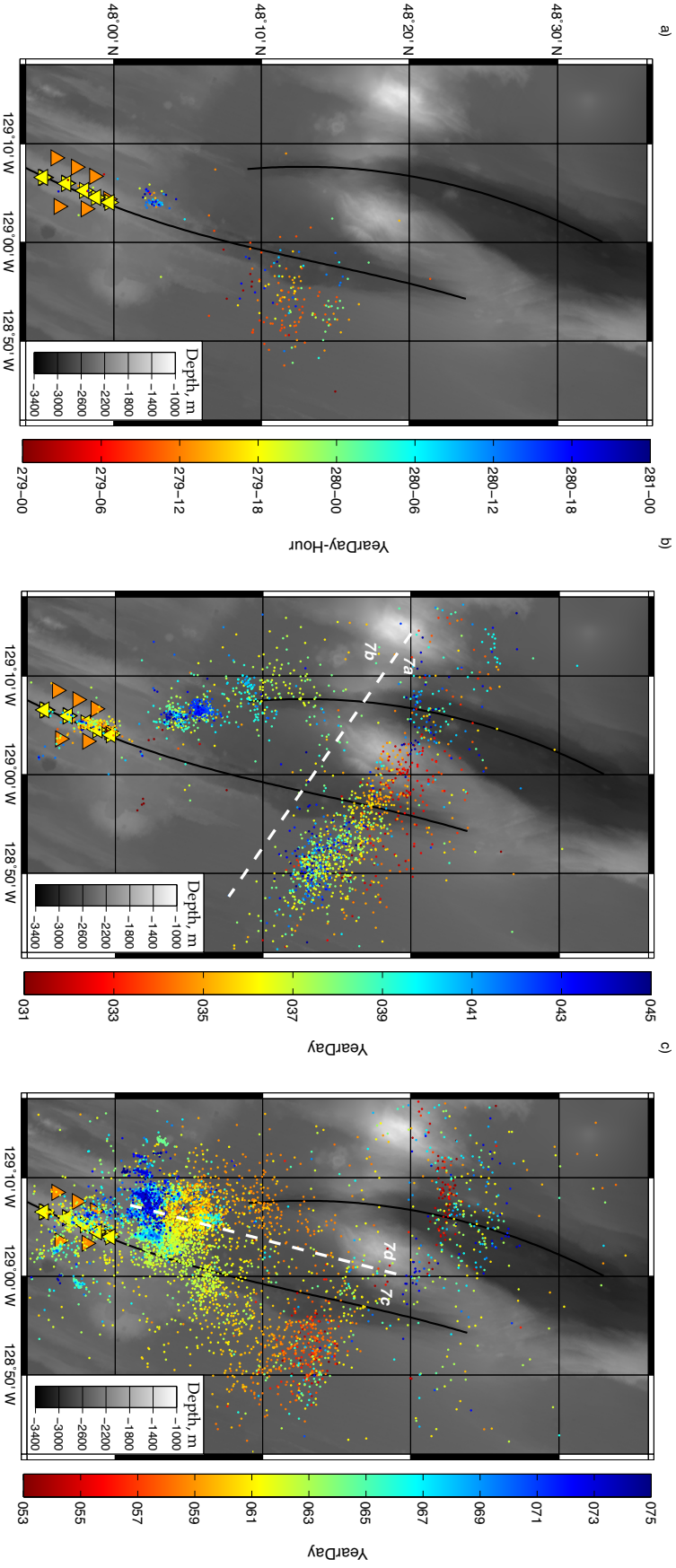

Figure 7. Plots showing the temporal migration of earthquakes in the 2005 swarms. (a) Longitude versus time for earthquakes on the northern Endeavour in the January swarm. (b) Latitude versus time for earthquakes on West Valley propagator in the January swarm. (c-d) Latitude versus time for earthquakes on northern Endeavour and West Valley propagator, respectively, in the February swarm. The division of earthquakes between geographic regions is illustrated in Figure 6. Dashed lines indicate the linear fit calculated by fitting a least squares straight line to specific time segments (indicated by color highlighting).

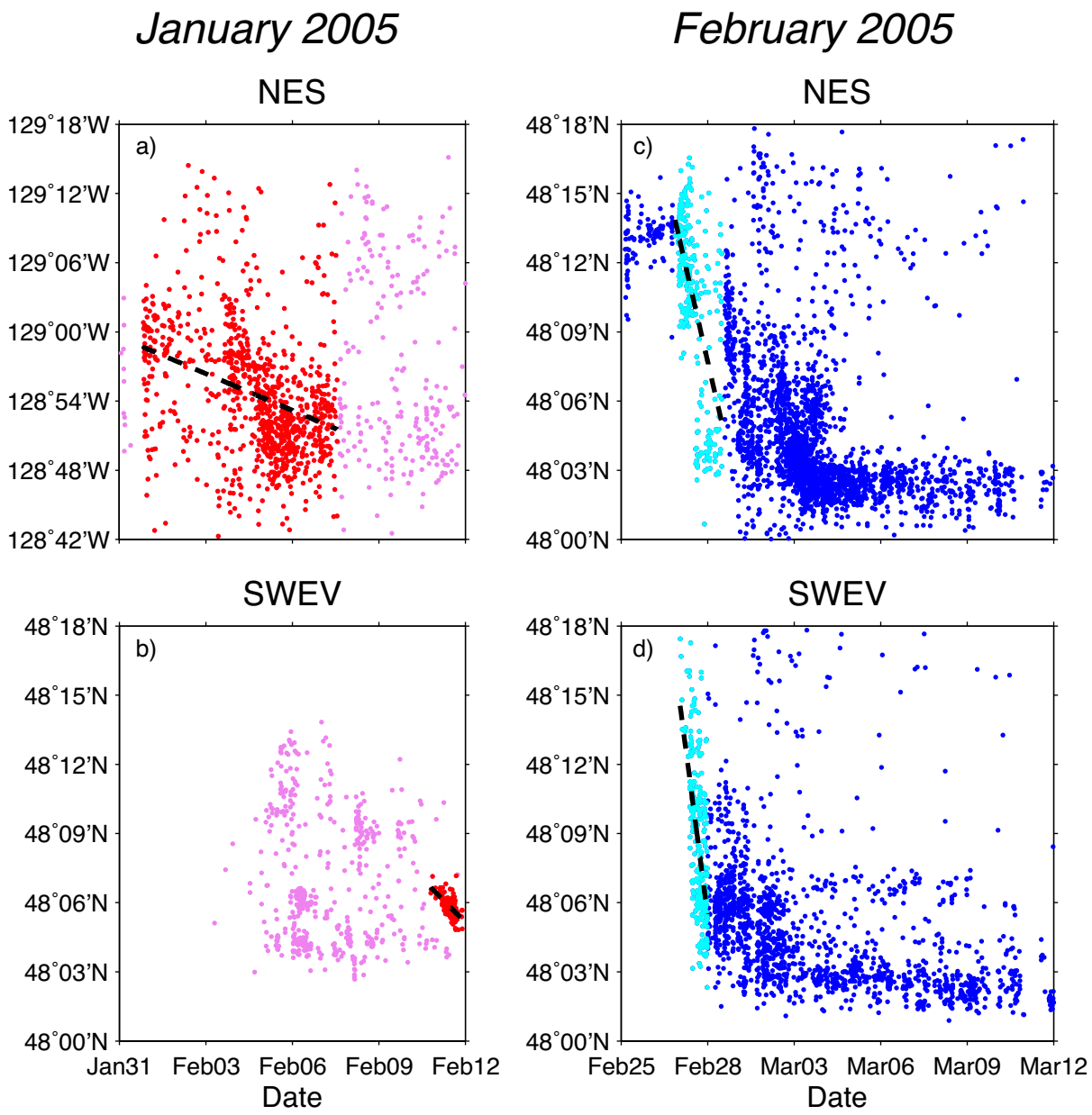

Figure 8. Seismicity in the Vent Field region plotted using the same conventions as Figure 5. (a) Bathymetric map of vent field area showing all earthquakes located with at least six arrivals color coded by time.). High temperature vent fields (yellow stars), seismometers (orange symbols) and the footprint of the AMC (gray shadow) are also shown. The white line (A-A') shows the location of the along-axis cross-section in Figure 9. (b) Histogram of daily earthquake counts and moment release curve with the onset of the swarms shown by dashed black lines. (c) Plot of earthquake count versus magnitude threshold used to calculate *b*-values and 2-σ uncertainties for periods before (green), during (blue), and after (red) the 2005 swarms. Note that a different magnitude of completeness was used to calculate *b*-values for the swarm period (dashed blue line) than for the periods before and after (dashed black line) the swarms.

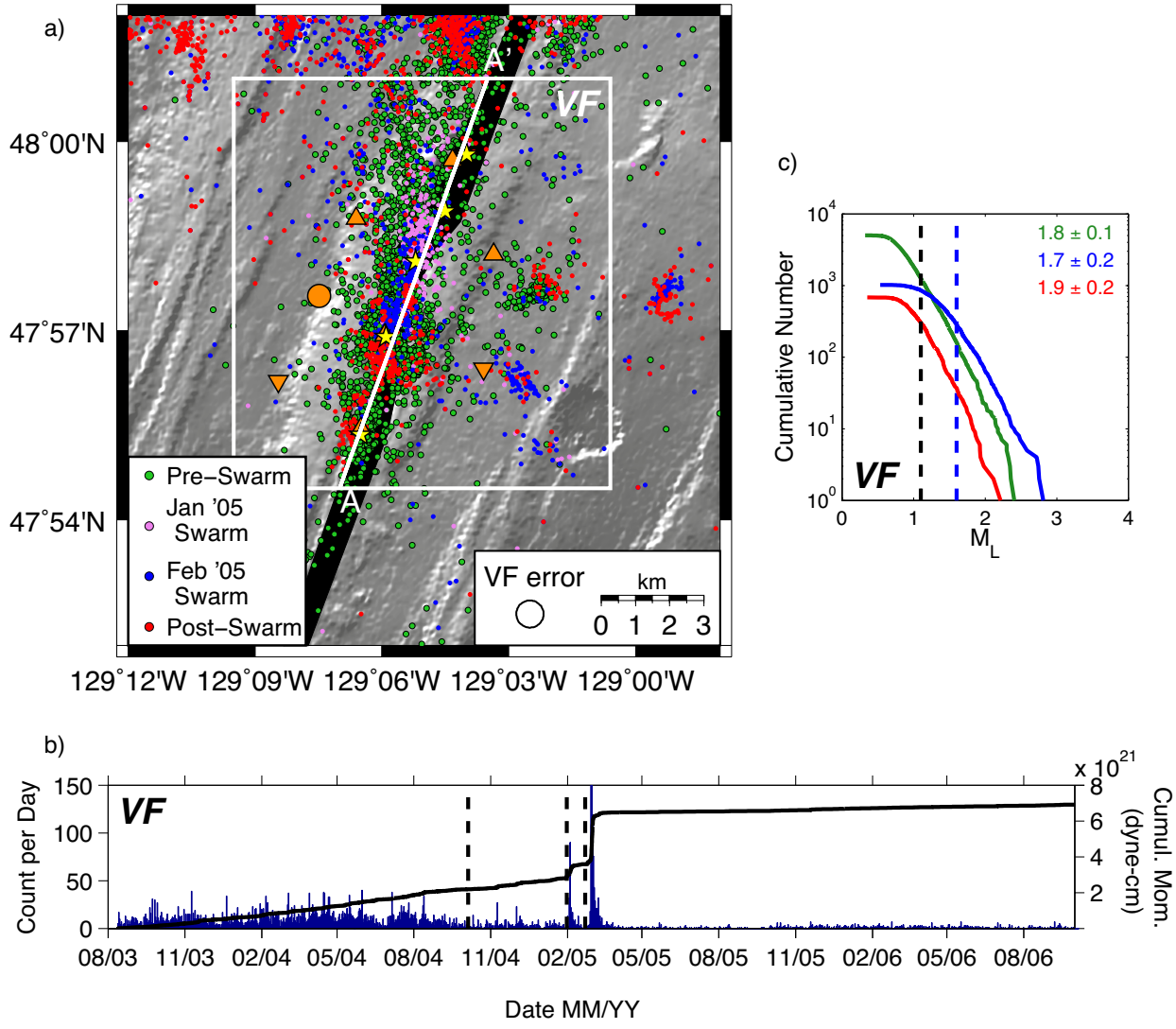

Figure 9. Along-axis cross-section showing vent field earthquakes for different time periods (circles color coded by time as in Figure 4). The thick gray line shows the top of the AMC [*Van Ark et al.*, 2007]. The location of the cross section is shown in Figure 8 and the maximum horizontal projection distance is 1 km.

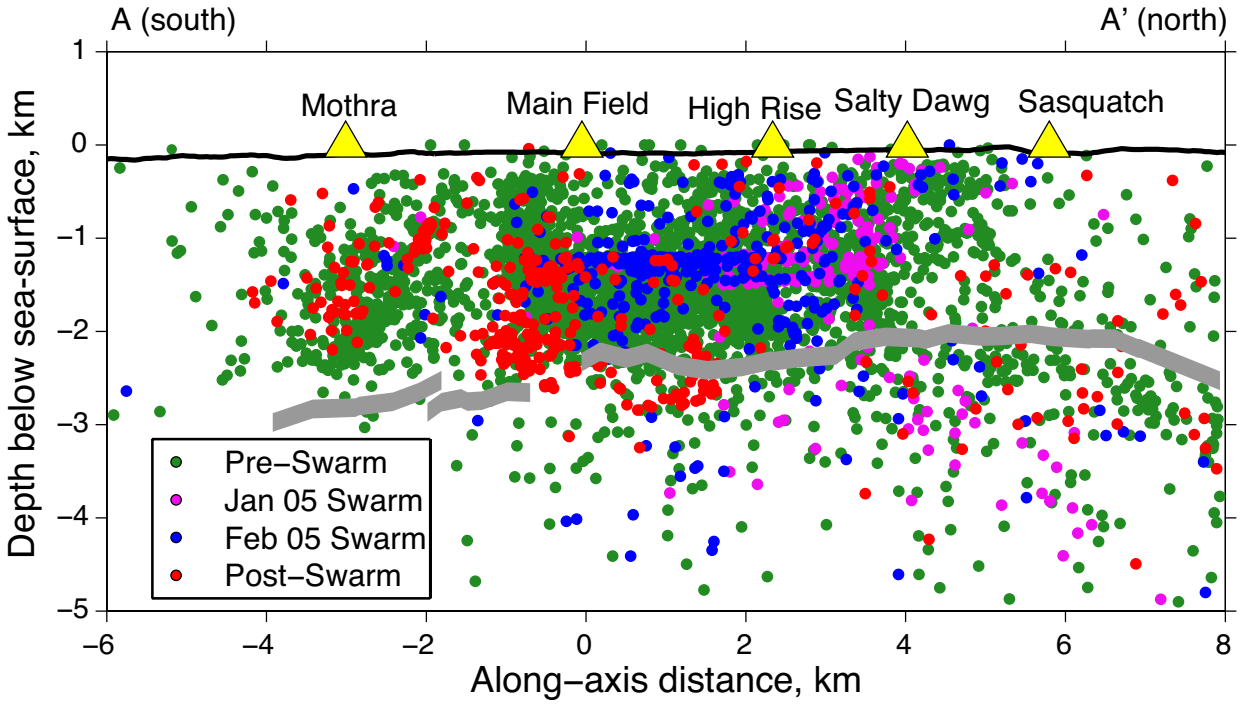

Figure 10. Seismicity in the southern regions plotted using the same conventions as Figures 5 and 8. (a) Grayscale bathymetry overlain by epicenters color coded by time. (b-c) Histograms of daily earthquake counts and moment release plots for the (b) COSE and NSS regions with the onset of the 2005 swarms shown with dashed black lines. (d-e) Plots of earthquake count versus magnitude threshold used to calculate *b*-values. The *b*-values and their uncertainties are labeled on the plots with dashed lines showing the magnitude of completeness. No *b*-values were calculated for the swarm periods, or for the post-swarm COSE region, because of an insufficient number of earthquakes.

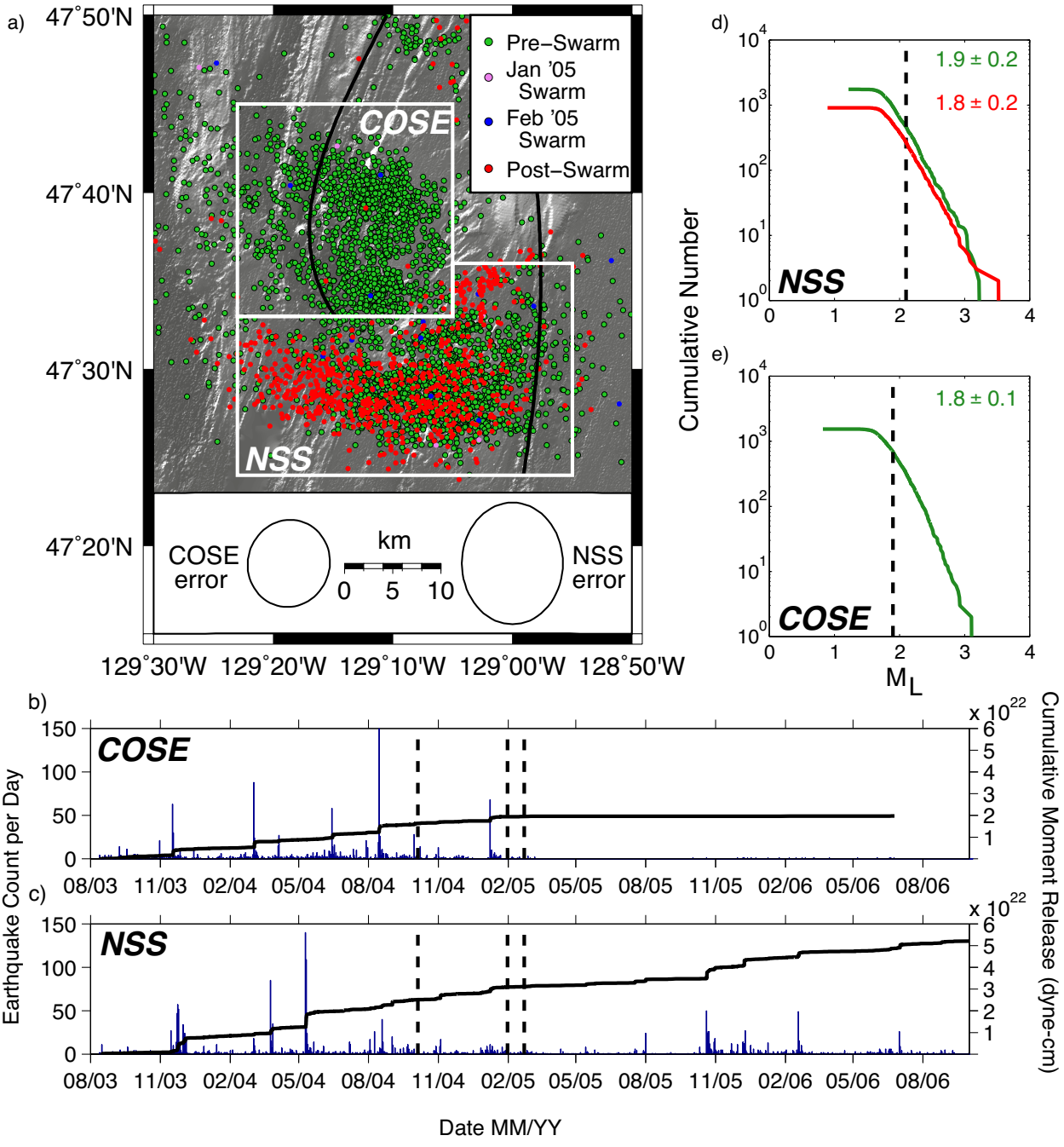

Table 1. Summary of instrument failures

Station	Year 1 (Aug 2003 – Aug 2004)	Year 2 (Aug 2004 – Sept 2005)	Year 3 (Sept 2005 – Oct 2006)
KEMO	-	Low S/N	-
KEMF	-	Low S/N	No data June 10 – Oct 31
KESQ	-	No data	-
KESW	-	No data Dec 9 – Feb 28	-
KESE	-	-	No data
KENW	-	-	-
KENE	-	-	-
KEBB	No data May 31 – Aug 9	No data March 14 – Sept 26	No data

Station locations are shown in Figure 1b. Periods during the deployment when instruments were not operating or recording degraded data are noted. Calendar dates are used to indicate periods when data is unavailable for a portion of a deployment. Low S/N indicates that the signal to noise was low because the gain was set very low so that only the largest events were recorded.

Table 2. Parameters used to obtain earthquake magnitudes

Parameter	P	S
ρ (g/cm^3)	3	3
c (km/s)	6.5	3.7
R	0.42	0.59
K	1.5	1.7
Q	(30 500)	(50 400)
f (Hz)	4-10	4-10

Values appropriate for mid-ocean ridge setting were taken from *Toomey et al.* [1985]. ρ is the rock density, c is the seismic wave speed, R is a radiation factor, K is a free surface correction, Q is a two-element attenuation model with the first value assumed within 1 km of the receiver and the second value elsewhere, and f is the frequency band used to obtain spectral amplitudes.

Table 3. Median formal location uncertainties

Region	$\overline{R}$ (km)	L_{maj} (km)	AZ_{maj} (˚N)	L_{min} (km)	AZ_{min} (˚N)	L_{vert} (km)	$L_{VP/VS}$ (km)
WV	46	4.3	87	1.2	2	-	4.8
NES	32	3.3	116	1.1	27	-	3.2
Northern SWEV	18.7	1.8	113	1.0	11	-	2.0
Southern SWEV	11.2	1.0	143	0.7	59	-	1.3
VF	2.4	0.5	4	0.3	13	0.8	0.2
COSE	36.5	4.3	106	1.3	16	-	3.8
NSS	51.7	5.3	90	1.4	4	-	4.7

Earthquakes with at least 10 arrivals were used to calculate the median formal location uncertainties from *Hypoinverse* for each region shown in Figure 4, with the SWEV divided into northern and southern portions. $\overline{R}$ is the median distance to the events from station KEMO, L is the length of the major (L_{maj}) and minor (L_{min}) principle axis of the 1-σ error ellipse, while AZ is the azimuth of the principle axis, measured clockwise from North. Vertical uncertainties (L_{vert}) were only calculated for the VF earthquakes since the depth was fixed for events outside the network. $L_{VP/VS}$ are additional radial uncertainties that would arise from a 5% uncertainty in V_P/V_S.

Chapter 3

UPPER CRUSTAL SEISMIC STRUCTURE OF THE ENDEAVOUR SEGMENT, JUAN DE FUCA RIDGE FROM TRAVEL TIME TOMOGRAPHY: IMPLICATIONS FOR OCEANIC CRUSTAL ACCRETION

3.1 Introduction

The upper oceanic crust is formed by episodic diking and eruptive volcanic events sourced from mid-crustal magma chambers, and is subsequently modified by tectonic extension, hydrothermal alteration, and off-axis volcanism. Understanding the interplay of these processes and their variation with time and location is a central goal of mid-ocean ridge research. Because seismic velocities are sensitive to composition, porosity, fracturing, temperature and the presence of melt, marine seismic imaging techniques are important tools for characterizing the structure of the crustal accretion zone and the off-axis crustal stratigraphy that reflects the time-integrated history of upper oceanic crust.

Multichannel seismic (MCS) studies are sensitive to the presence of interfaces within the crust and can also be used to resolve the shallow velocity structure. As such, they have been used to measure several characteristics of upper crustal structure, including: (1) the subsurface geometry of an axial magma chamber (AMC), including its along-axis continuity, width, and thickness [e.g., *Kent et al.*] and its melt content [*Hussenoeder et al.*, 1996; *Singh et al.*, 1998]; (2) variations in the depth from the seafloor to the base of seismic layer 2A, which is most commonly interpreted as the boundary between high-porosity extrusives and low-porosity sheeted dikes [*Harding et al.*, 1993; *Kent et al.*, 1994; *Kappus et al.*, 1995; *Carbotte et al.*, 1997]; (3) the presence of off-axis magma bodies that may contribute to the accretion of oceanic crust away from the ridge axis [*Canales et al.*, 2012]; and (4) off-axis velocity increases in the

extrusive unit [*Rohr*, 1994; *Nedimovic et al.*, 2008] that provide information about sealing of cracks and closure of pore space due to hydrothermal mineral precipitation [*Jacobson*, 1992].

Seismic refraction tomography studies provide complementary information on spatial variations in seismic velocity. They have been used to measure: (1) thickness variations in layer 2A inferred from velocity variations within the upper 1 km of crust [*Toomey et al.*, 1990; 1994; *Bazin et al.*, 2001]; (2) velocity variations in the upper crust related to fracturing and thermal structure [*Toomey et al.*, 1994; *Dunn et al.*, 2000; *Van Avendonk et al.*, 2001; *Dunn et al.*, 2005; *Seher et al.*, 2010a]; (3) mid-crustal magma bodies located both beneath the ridge axis [*Toomey et al.*, 1990; *Dunn et al.*, 2000; *Magde et al.*, 2000] and away from it [*Durant and Toomey*, 2009]; (4) variations in anisotropy that are directly related to aligned cracks and fractures in the upper crust [*Barclay et al.*, 1998; *Dunn and Toomey*, 2001; *Barclay and Wilcock*, 2004; *Tong et al.*, 2004; *Seher et al.*, 2010b].

The Endeavour segment of the Juan de Fuca Ridge (JdFR) has an intermediate spreading rate and is characterized by a central portion underlain by an axial magma chamber that supports several high-temperature hydrothermal vent fields and by large overlapping spreading centers at either end. In this study, seismic tomographic methods are utilized to characterize three-dimensional segment-scale variations in the isotropic and anisotropic velocity structure of the upper crust of the Endeavour segment. The images are used to investigate the processes of crustal accretion and their variations along-axis on an intermediate spreading rate ridge segment.

3.2 Endeavour segment geologic setting

The Endeavour segment is a ~90-km long, intermediate-rate (56 mm/yr [*Wilson*, 1993]) spreading center located near the northern end of the JdFR (Figure 11). The Endeavour segment

forms left-stepping overlapping spreading centers (OSCs) with the West Valley and Northern Symmetric segments. To the south, the Cobb OSC separates the Endeavour and Northern Symmetric segments by ~30 km. Since its formation at 5 Ma [*Hey and Wilson*, 1982] the net migration of the Cobb OSC has been to the north, but it has undergone alternating episodes of northward and southward propagation during its recent history [*Johnson et al.*, 1983; *Shoberg et al.*, 1991]. From 0.7 – 0.4 Ma the northern end of the Northern Symmetric segment propagated quickly northward leaving a bathymetric record of a failed propagator on the Juan de Fuca Plate (Figure 11). The southern end of the Endeavour segment then propagated more gradually to the south before the current episode of northward propagation of the Northern Symmetric segment started at < 0.1 Ma [*Shoberg et al.*, 1991]. To the north, the Endeavour – West Valley (E-WV) OSC separates the two spreading centers by 15 km. The E-WV OSC formed within the past 50 kyr, and perhaps as recently as 10 kyr, when the spreading axis switched from the Middle Valley segment to the West Valley segment (Figure 11) as a result of ongoing reorganization of plate boundaries at the northern end of the Juan de Fuca Ridge [*Davis and Lister*, 1977; *Davis and Villinger*, 1992].

Several prominent seamount chains on the Pacific plate side of the JdFR intersect the Endeavour segment [*Davis and Karsten*, 1986]; they are, from south to north, the Springfield, Heckle, and Heck seamount chains. The central 20 km portion of the Endeavour segment features a plateau that extends 45 km across axis and is elevated 300 m relative to the rest of the segment. It has been postulated that this plateau is a result of enhanced crustal production due to the ridge capturing the hot spot anomaly associated with the Heckle Seamount chain [*Karsten and Delaney*, 1989; *Carbotte et al.*, 2008].

A recent MCS experiment indicates that AMCs underlie portions of each segment of the JdFR. The thickness of seismic layer 2A and the AMC depth vary by segment [*Carbotte et al.*, 2008] and, in general, both increase from south to north. On the Endeavour segment, the AMC underlies the central portion of the segment at 2.1 – 3.3 km depth [*Van Ark et al.*, 2007]. The AMC provides a heat source for five high temperature hydrothermal vent fields that are spread 2 – 3 km apart in the axial valley [*Kelley et al.*, 2002; 2012]. From south to north, the fields are named Mothra, Main Endeavour, High Rise, Salty Dawg, and Sasquatch. The hydrothermal systems have been studied extensively and are characterized by significant along-axis gradients in temperature and chemistry [*Butterfield et al.*, 1994; *Kelley et al.*, 2002; *Kelley et al.*, 2012].

Studies of microearthquakes from the central axial region show a concentration of seismicity at ~2-km depth just above the AMC [*Wilcock et al.*, 2002; 2009; *Weekly et al.*, 2013], with the most intense seismicity occurring beneath the High Rise and Main Endeavour fields [*Wilcock et al.*, 2009] which also have the largest area and highest heat flux [*Kellogg*, 2011]. *McClain et al.* [1993] argue that off-axis normal faults maintain the conduits necessary to support robust hydrothermal circulation and the formation of long-standing vent fields. The characteristics of hypocenters and focal mechanisms for earthquakes recorded in 2003-2004 are consistent with ongoing magma inflation [*Wilcock et al.*, 2009].

The Endeavour segment has been the site of several large volcanic earthquake swarms. In June 1999, a swarm on the central Endeavour [*Johnson et al.*, 2000; *Bohnenstiehl et al.*, 2004] significantly perturbed the chemistry of hydrothermal fluids [*Lilley et al.*, 2003; *Seyfried et al.*, 2003] and was the result of a dike intrusion [*Davis et al.*, 2001]. A second swarm to south in the 2000 may also have been associated with a dike [*Bohnenstiehl et al.*, 2004]. In January and February 2005, two complex seismic swarm sequences located near the E-WV OSC likely

involved magmatic intrusions on the northern Endeavour and southernmost portion of the West Valley segment [*Hooft et al.*, 2010; *Weekly et al.*, 2013]. These swarms were followed by a substantial decrease in seismicity rates along the Endeavour segment and have been interpreted as the end of a 6-year non-eruptive spreading event that started with the 1999 swarms and cumulatively relieved plate-spreading stresses [*Weekly et al.*, 2013].

The MCS data show that seismic layer 2A thickens along axis from about 150 – 300 m on the northern Endeavour segment to almost 600 m south of the segment center [*Van Ark et al.*, 2007]. In contrast to seismic studies conducted at the southern JdFR [*Canales et al.*, 2005] and the East Pacific Rise [*Harding et al.*, 1993; *Kent et al.*, 1994] that found evidence for 2A thickness increasing off-axis, there is no clear pattern of off-axis thickening at the Endeavour segment [*Van Ark et al.*, 2007]. There appears to be a weak correlation between fault-bounded, axis-parallel bathymetric highs and a thicker layer 2A [*Van Ark et al.*, 2007]. *Barclay and Wilcock* [2004] also inferred this correlation from a small seismic refraction data set. MCS profiles that extend onto the flanks of the JdFR show systematic increases in layer 2 velocities with off-axis distance; layer 2A velocities attain values typical for mature oceanic crust of ~4.0 km/s within 5 – 8 Ma of formation [*Nedimovic et al.*, 2008] while the upper portion of layer 2B undergoes a much more rapid maturation with velocities increasing by ~0.8 km/s within ~0.5 Ma [*Newman et al.*, 2011]. The gradual evolution of layer 2A is attributed to a reduction in porosity of the upper extrusive volcanic unit through long-term exposure to "passive" off-axis hydrothermal circulation, while the more rapid evolution of layer 2B results from mineral precipitation driven by the solidification and cooling of the oceanic crust [*Carbotte et al.*, 2012].

3.3 Experiment geometry and data acquisition

In August and September 2009, a three-dimensional seismic tomography experiment was conducted along the Endeavour segment (Figure 12). A seismic network comprising 68 four-component (three orthogonal geophones and a hydrophone) ocean bottom seismometers (OBSs) was deployed at 64 sites and recorded ~5,500 airgun shots from the 36-element, 6600 in^3 airgun array of the *R/V Marcus G. Langseth*. The experiment used a nested source-receiver geometry to collect data that sampled the crust and topmost mantle beneath an approximately 90-km-by-50-km area centered on the ridge segment. The segment-scale upper mantle structure was targeted with six 105-km-long lines shot at a maximum distance of 30 km from the ridge axis and two ridge-perpendicular lines shot along the northern and southern limits of the experiment. An intermediate-scale grid was comprised of 19 shot lines spaced 1 km apart within a 20-km-by-60-km region centered on the shallow central plateau. This grid recorded travel-time data for imaging off-axis structure and the along-axis distribution of the crustal magmatic plumbing system. The finest grid covered a 10-km-by-20-km area centered near the Main Endeavour vent field (47˚57'N, 129˚06'W) and comprised 10 shorter (20-km-long) shot lines interlaced within the crustal grid. This central grid included the densest shot and receiver distributions and was designed to image the detailed structure of the upper crust near the hydrothermal vent fields. Shot spacing along all lines was 500 m. All shot lines were obtained with the airgun array towed at 9-m depth; the middle 105-km-long, ridge-parallel lines on each flank were reshot with the airguns towed at 15-m depth to increase the low-frequency content of the source signal.

Instrument and shot locations were determined simultaneously by inverting acoustic-water-wave arrivals [*Creager and Dorman*, 1982] that were automatically picked using an auto-regressive method [*Takanami and Kitagawa*, 1988]. Water column velocity structure was

determined from expendable bathythermograph profiles collected throughout the experiment. The final horizontal 1-σ location uncertainties for stations and shots were 13 m and 9 m, respectively. Vertical station uncertainty was 10 m, as determined from the bathymetric map obtained using the onboard EM122 multibeam system.

The data return was remarkably high, with 49 instruments yielding good quality data on both the hydrophone and vertical channels and only 2 sites lacking good data on either channel. Figure 13 shows several examples of crustal arrivals recorded by a station on the east flank of the central Endeavour (Figure 12). Ray paths that do not cross the ridge axis exhibit impulsive first-arriving (*Pg*) energy with a high signal-to-noise ratio and good trace-to-trace coherency at shot-receiver offsets up to 35 km (Figure 13a-b). Waveforms from *Pg* ray paths that propagate across the ridge axis generally exhibit a more complex shape where first-arriving energy is emergent and attenuated (Figure 13c).

An iterative strategy for compiling a catalog of *Pg* travel-times was adopted. First, impulsive arrivals for non-ridge-crossing ray paths were picked at small source-receiver offsets of < 10 km. The range of picks was progressively increased by inverting the picks for velocity structure and using the results to generate predicted travel-times that guided subsequent picking efforts at larger ranges. For non-ridge-crossing ray paths, picking first arrivals was possible up to ranges of ~35 km. However, the maximum pick range was much smaller for ridge-crossing ray paths (~20 km) due to lower amplitudes and a lack of trace-to-trace coherency of waveforms. The total data set includes 96,156 *Pg* travel-times picked on the 62 reporting instruments. For 49 of the 62 instruments, arrival times were picked after summing the vertical and hydrophone channels while arrivals for the remaining 13 instruments were identified on one channel, depending on data quality.

Pick uncertainties were estimated visually, with larger uncertainties assigned to waveforms with an emergent first arrival, or to groups of waveforms that showed significant trace-to-trace variability. Nearly 80% of *Pg* data were assigned an uncertainty between 10 and 15 ms while ~97% were assigned uncertainties less than 20 ms. The root-mean-square uncertainty for the entire *Pg* dataset is 13 ms. It is noted that other sources of experimental error that include source or receiver location uncertainties, instrument clock corrections and seafloor bathymetry, result in travel time uncertainties that are generally smaller than the picking error [*Barclay et al.*, 1998].

3.4 Tomographic method

I used a tomographic technique to invert travel-time data for isotropic slowness and seismic anisotropy [*Toomey et al.*, 1994; *Dunn et al.*, 2005]. Assuming an initial model, I forward modeled predicted travel times and calculated residuals for ray paths between sources and receivers. The inverse problem was linearized about the model to obtain a set of equations that mapped model perturbations into travel time residuals. Additional equations with parameters set by the user determined the smoothness and *a priori* variance of the model. A least squares inversion of the overdetermined set of equations was used to update the model, and subsequent iterations were repeated until the RMS travel-time residual converged.

3.4.1 Forward problem

The velocity model for ray tracing was parameterized in terms of slowness with nodes arranged in a rectangular grid that aligned with the trend of the rise axis. Ray paths were calculated using the shortest-path ray tracing method [*Moser*, 1991]. The model was overlain by

a water layer and included seafloor topography by vertically shearing columns of nodes [*Toomey et al.*, 1994]. Based on previous active source tomography experiments designed to image upper crustal structure between 0 – 2 km [*Barclay et al.*, 1998; *Dunn et al.*, 2000], and on source-receiver spacing, a uniform grid spacing of 200 m was chosen for the ray tracing model.

Following *Dunn et al.* [2005], anisotropic slowness was parameterized on the slowness grid as:

$$u(r) = \frac{u_{iso}(r)}{1 + A(r)\cos[2\theta(r)] + B(r)\sin[2\theta(r)]} \tag{4}$$

where u_{iso} is the isotropic slowness, r is the position, θ is the ray path azimuth, and A and B are scale terms that control the magnitude and orientation of the fast direction of anisotropy, which are given by $2(A^2 + B^2)^{0.5}$ and $\mathrm{atan}(B/A)/2$, respectively. This parameterization allowed for explicit inversion of three-dimensional variations in the orientation and percent anisotropy instead of fixing these parameters as constants and solving for isotropic slowness.

Implicit in the parameterization of (4) is the assumption that *P*-wave anisotropy results from a hexagonal symmetry system. This system is appropriate for media where anisotropy results from aligned vertical cracks [*Crampin*, 1993], which has been widely accepted as the primary mechanism for seismic anisotropy in the upper oceanic crust [*Barclay et al.*, 1998; *Dunn and Toomey*, 2001; *Seher et al.*, 2010a]. In this system, *P*-wave velocities in the symmetry planes perpendicular to the crack plane can be expressed as a linear combination of cos(2θ) and cos(4θ) terms. Furthermore, assumed in (4) is that liquid-filled cracks in the upper crust have an aspect ratio > 0.01 (thinner cracks would yield *P*-wave velocity structure that is primarily modulated by cos(4θ) terms [*Hudson*, 1981]). As discussed below, this assumption is justified by the observed cos(2θ) azimuthal variation in isotropic travel-time residuals.

3.4.2 Inverse problem

Following *Toomey et al.* [1994], the inverse problem was solved using an iterative technique that required the user to set *a priori* model uncertainties and smoothing parameters that operated on perturbational models parameterized for isotropic slowness and anisotropy. The perturbational models comprised rectilinear grids that were denser within 10 km of the central axial valley to reflect the greater number of ray paths; horizontal node spacing was 1 km outside of this region and 0.5 km within. Vertical node spacing was a uniform 0.25 km. Inversions were regularized by penalizing model roughness and size. A jumping strategy was used to seek a final model that was small and smooth rather than to minimize model perturbations [*Shaw and Orcutt*, 1985]. I sought to minimize a functional of the general form:

$$\begin{aligned} s^2 = {} & \Delta t' C_d^{-1} \Delta t + \lambda_p \left(m_0 + \Delta m\right)' C_m^{-1} \left(m_0 + \Delta m\right) \\ & + \lambda_V \left(m_0 + \Delta m\right)' C_V^{-1} \left(m_0 + \Delta m\right) + \lambda_H \left(m_0 + \Delta m\right)' C_H^{-1} \left(m_0 + \Delta m\right) \end{aligned} \tag{5}$$

where Δt is a vector of the differences between observed and calculated travel times; C_d is a diagonal matrix of the data variance composed of the squares of the *Pg* arrival-time uncertainties; m_0 is a vector of the cumulative perturbation to the isotropic slowness and anisotropic model parameters from previous iterations; Δm is the model perturbation for the current iteration; C_m, is a diagonal matrix on the *a priori* model variance; C_V and C_H are matrices that apply vertical and horizontal Gaussian smoothing, respectively, to each model parameter with a characteristic length of the Gaussian equal to the node spacing; and λ_P, λ_V and λ_H are weighting parameters. The inversion procedure allowed separate values of the smoothing weights for isotropic slowness and anisotropic model parameters where λ_{AV} and λ_{AH} are smoothing weights for anisotropic parameters.

Because the solution to the inverse problem is inherently non-unique, my strategy was to explore the parameter space of the weighting parameters using a systematic approach to construct smooth solutions that adequately fit the data according to the function:

$$\chi^2 = \frac{1}{N}\sum_{i=1}^{N}\frac{\Delta t_i^2}{\sigma_i^2} \tag{6}$$

where N is the number of travel time observations and Δt_i and σ_i are the travel time residual and pick uncertainty of the ith travel time, respectively.

3.5 Results

The inversion volume (Figures 11-12) measured 90 km x 120 km x 9 km, was centered on the Endeavour segment and was rotated clockwise 21° so that the y-axis approximately paralleled the spreading axis along the central portion of the Endeavour segment. The starting model for the inversions (Figure 14a) was a smoothed approximation to a one-dimensional crustal model derived from a seismic refraction experiment conducted along the central portion of the Endeavour segment between 47˚55'N and 48˚05'N [*Cudrak and Clowes*, 1993]. I adopted a multi-stage approach to obtaining a preferred model that includes isotropic and anisotropic structure. First, the data was inverted solely for isotropic structure with $\lambda_P = 1$, $\lambda_V = 200$, and $\lambda_H = 300$ while using the smoothed one-dimensional model above as a starting model. A smoothed approximation to the longer wavelength structure was obtained by applying a three-dimensional median filter to the resulting model where the structure was averaged over spatial half-widths of 1 km, 5 km, and 0.6 km in the x, y, and z directions, respectively. A second isotropic inversion was performed using the same smoothing parameters as before but with the spatially smoothed model as the starting point. Lastly, the solution space was explored by including anisotropic smoothing parameters and systematically varying λ_P, λ_V, λ_H, λ_{AV}, and λ_{AH} to find a model that

minimized the misfit function (3) and included both isotropic and anisotropic structure. I assumed *a priori* model uncertainties of 50% and the preferred model does not heavily penalize the model norm (λ_P = 1) but instead penalizes vertical and horizontal roughness for both the isotropic ($\lambda_H = \lambda_V$ = 200) and anisotropic components ($\lambda_{AH} = \lambda_{AV}$ = 400). Varying the values of horizontal smoothing had a much larger impact on the final misfit than varying vertical smoothing. Larger values for spatial smoothing gave smoother models with lower amplitude anomalies while smaller values yielded models higher amplitude fine-scale features. The preferred model is the smoothest model that achieved a χ^2 value close to unity (1.04) and thus, fit the travel time data to the estimated picking uncertainty.

My strategy for testing the resolution of the preferred model involved analyzing the spatial distribution of ray paths within the experiment geometry, and conducting inversions of travel times obtained from synthetic slowness and anisotropy models. The results are discussed in Appendix A.

3.5.1 Isotropic structure

Average depth-velocity profiles (Figure 14a) for well resolved regions reveal large differences in upper crustal structure between the flanks of the segment center and the ends of the segment near the OSCs, including the adjacent relict Middle Valley segment (blue and red boxes, respectively, Figure 12). Upper crustal velocities in the Cobb OSC, the E-WV OSC, and the southern end of Middle Valley are uniformly slower than the starting model, with Middle Valley displaying the lowest velocities of the three at all depths. In contrast, velocity-depth profiles near the segment center for the eastern and western flanks exhibit similar structure, both with faster velocities than the starting model below 0.5 km depth (Figure 14a). The greatest

difference in velocity between the Middle Valley region and the ridge flanks is 1.5 km/s between 1.2 and 1.4 km depth, and the difference exceeds 1.0 km/s from 0.6 to 2.2 km depth.

The segment-scale velocity structure (Figure 15) is strongly heterogeneous. Beneath the E-WV OSC, a broad low-velocity anomaly is observed at all depths, with a peak velocity anomaly of –0.9 km/s. To the east of the northern Endeavour segment is another broad low-velocity anomaly at all depths that reaches –1.0 km/s and is oriented in a ridge-parallel direction. This anomaly coincides with the south end of the relic Middle Valley segment (Figure 11). At the Cobb OSC there is another broad low-velocity region. However, the peak velocity anomaly in this region (-0.5 km/s) is less than that observed within the E-WV OSC. Low velocities are also observed in the southeast corner of the model to the west of the Northern Symmetric segment in a region that coincides with a failed propagator of the Cobb OSC (Figure 11). The detailed velocity structure is only well constrained in a portion of each OSC due to the spatial limitations of ray coverage and this is reflected in the synthetic checkerboard tests (see Appendix B). However, the OSCs clearly exhibit lower velocities compared to the rest of the segment. In contrast to the ends, the central portion of the Endeavour segment shows a markedly different structure with higher average velocities and substantial lateral heterogeneity (Figures 14a and 15). At depths greater than 1.0 km, the segment center is characterized by a ~50-km-wide high-velocity anomaly with peak velocity variations of 0.5 km/s that appears to extend to the eastern and western limits of the imaged region (Figures 15d-g).

Within the upper 1 km of the central portion of the Endeavour segment is a sequence of banded velocity anomalies that align with the trend of the ridge axis (Figure 16). The bands are about 4 km wide, extend 30 to 40 km along-axis and 10 km to 12 km to either side. It is of interest that none of the low-velocity bands locate directly beneath the bathymetric highs, but are

instead displaced toward the flankward side of the ridge (Figure 17b-d). The ridge-parallel lineations are most prevalent within the upper ~1 km of crust, but the ridge-parallel anomalies persist between 1 – 2 km depth on the east flank (Figure 16c-e). On the west flank, longer wavelength high-velocity bands are visible from 1.2 – 2.4 km depth (Figure 16c-f) but are rotated 15˚ counter-clockwise relative to the ridge. However, synthetic models indicate that these latter features are likely artifacts (see Appendix B).

Within the Endeavour axial valley, there is significant along-axis heterogeneity (Figure 17e). Velocities at 0 to 2 km depth beneath the hydrothermal vent fields are generally higher than velocities found near the ridge axis immediately to the north and south. Velocities are particularly high beneath the northernmost Salty Dawg and Sasquatch vent fields where the anomaly reaches 0.5 km/s at shallow depths. Further south, there is a small low-velocity anomaly that extends to ~0.8 km depth between the Main Endeavour and High Rise vent fields. Below 2.0 km depth and immediately above the AMC, low-velocity anomalies are observed between the Main Endeavour and High Rise vent fields and several kilometers to the north of Sasquatch field.

3.5.2 Anisotropic structure

Figure 18 shows average travel time residuals in 20˚ azimuthal bins for the preferred three-dimensional isotropic model plotted against the azimuth of the Y-axis of the tomography grid for three different depth intervals. The travel-time residuals show a clear cos(2θ) azimuthal variation, which is consistent with faster propagation along ray paths oriented parallel to the trend of the Endeavour segment. The peak-to-peak amplitudes of these azimuthal variations

decrease from 30 ms for rays turning above 2 km depth to 9 ms for those turning between 2 and 3 km depth, indicating the azimuthal dependence is strongest at shallower depths.

The tomographic inversion recovers a substantial component of anisotropic structure, with the percentage anisotropy dependent on both the depth and distance from the ridge axis. The horizontally averaged percentage of anisotropy within 10 km of the ridge axis decreases from over 6% in the upper 1 km to less than 2% at 3 km depth (Figure 19). At all depths, the percentage of anisotropy is highest on the ridge axis and decreases substantially off-axis over a length scale of 5 to 10 km (Figure 20a-c). For example, at 1 km depth the average percentage of anisotropy decreases from about 10% on-axis to 2 to 3% 10 km away (Figure 20b). Synthetic tests (Appendix B) show that this decrease is well resolved, although the models may underestimate anisotropy well off-axis because a portion of the anisotropic signal is mapped into isotropic bands paralleling the 105-km-long refraction lines.

At depths between 1 and 3 km the off-axis decrease in anisotropy is accompanied by increased seismic velocities (Figure 21). At 1 km depth, the 7 – 8% decrease in anisotropy coincides with an increase in mean velocity from 5.1 km/s to 5.4 km/s (Figure 21b). At 2.2 km depth, the percent anisotropy decreases from 4% to 2% while mean velocities increase from 6.2 km/s to 6.5 km/s (Figure 21e). Above 1 km depth, the decrease in anisotropy is not accompanied by a systematic trend in velocities (Figure 21a).

High levels of anisotropy are observed everywhere near the ridge but there is significant along-axis heterogeneity (Figure 20a-c). The highest amplitude signal occurs to the north of the vent fields near Y = 15 km (Figure 20a-c). There, shallow anisotropy values exceed 15% and relatively high values persist to 2 km depth. This strongly anisotropic region is shifted slightly toward the Pacific plate and coincides with the southern extent of the E-WV OSC. Other

localized zones of relatively high anisotropy are also observed near Y = 5 km just north of Sasquatch field, immediately beneath the vent fields, and to the south near Y = -15 km (Figure 20a-c).

As might be expected, the overall direction of the fast axis of anisotropy parallels the central Endeavour segment but there are variations in azimuth that seem to mirror morphological features. In the E-WV OSC, the anisotropy rotates to parallel the curvature of the Endeavour arm of the OSC. Towards the south between Y = -20 km and Y = -30 km the fast direction on either side of the ridge converges to the south, mimicking the converging trends of the abyssal hills. At off-axis distances greater than ~10 km, where the level of the anisotropy is greatly reduced, the fast direction is variable but is less well resolved due to incomplete azimuthal ray path coverage outside of the crustal grid (Appendix B).

3.6 Discussion

3.6.1 Segment-scale isotropic velocity variations

The data indicate that increased fracturing in the OSCs causes low velocities that persist off-axis and record the history of ridge propagation. The broad zone of relatively high velocities in the segment center is bordered by low-velocity regions that coincide closely with the regions influenced by the OSCs (Figure 15). In the southeast corner of the model, low velocities are observed to the east of the Cobb OSC in a region of a failed rift that terminated near 47˚50'N (Figure 11) [*Johnson et al.*, 1983]. To the north, low velocities are observed to the east of the E-WV OSC in Middle Valley and to the west in the vicinity of the Heck Seamounts.

Tomographic studies show that intra-segment variability of upper crustal velocity structure is not exclusive to the Endeavour. Figures 14b-c show average velocity profiles from

this study compared to example profiles for the East Pacific Rise [*Canales et al.*, 2003] and for the Mid-Atlantic Ridge [*Hooft et al.*, 2000]. The vertical velocity functions for the eastern and western flanks of the central Endeavour segment are similar to previously published results from the central Endeavour [*Cudrak and Clowes*, 1993; *Barclay and Wilcock*, 2004], and from the CoAxial Segment of the Juan de Fuca Ridge [*Sohn et al.*, 1997]. They are also quite similar to the structure observed in the center of segments along the Mid-Atlantic Ridge near 35˚N (Figure 4c) [*Hooft et al.*, 2000]. At sites away from segment boundaries on the East Pacific Rise at 8-10˚N (Figure 4b) [*Canales et al.*, 2003] and elsewhere the upper crustal velocities are up to ~0.5 km/s faster than values for the central Endeavour segment [*Grevemeyer et al.*, 1998; *Bazin et al.*, 2001; *Van Avendonk et al.*, 2001]. However, if the profiles from the EPR and Endeavour are scaled relative to the depth of the AMC (~1.6 km on the northern EPR [*Detrick et al.*, 1987; *Kent et al.*, 1993] and ~2.5 km on the Endeavour [*Van Ark et al.*, 2007]) they are quite similar. Thus, the differences may simply reflect the thinning of layer 2 units on the EPR.

There are also strong similarities between velocity profiles at the ends the Endeavour segment and segment boundaries elsewhere. The profiles for the E-WV OSC and the relic OSC on the western EPR [*Canales et al.*, 2003] are nearly identical (Figure 14b). Above 2 km, the E-WV OSC profile is also reasonably similar to the profile obtained by *Hooft et al.* [2000]. Below 2 km, the OH2 profile is markedly faster, likely as a result of thinner crust at the end of this segment [*Hooft et al.*, 2000]. The velocity profile for Middle Valley is most similar to the Oceanographer Fracture Zone above 2 km depth.

Bazin et al. [2001] propose that anomalously low velocities observed in the shallow crust near the 9˚N OSC basin are attributed to thickness variations caused by lavas pooling within the overlap basin. However, this model cannot explain the differences at the Endeavour. The low

velocities at the segment ends extend well below 1 km, the maximum depth to which layer 2A thickness variations map into the tomographic models. At the northern end of the segment, where the velocities are lowest, layer 2A is thin beneath the ridge-axis [*Van Ark et al.*, 2007]. Since the West Valley segment has only been actively spreading for 10-50 kyr [*Davis and Villinger*, 1992], it seems unlikely that a thick layer of extrusive volcanic rocks could have accumulated in the E-WV OSC during this time.

The preferred interpretation of the lower upper crustal velocities observed at the ends of the Endeavour and adjacent Middle Valley segments is that there is increased porosity due to enhanced tectonic fracturing within the OSC. Near large transform faults, depressed seismic velocities are commonly attributed to tectonic fissuring and cracking [*Detrick et al.*, 1993a; *Begnaud et al.*, 1997; *Van Avendonk et al.*, 2001]. Within smaller overlap basins, shearing of the seafloor fabric and rotation of adjacent limbs of the overlap basin [*Christeson et al.*, 1997] can produce porosity increases of ~10%. In addition, vigorous hydrothermal circulation on the central Endeavour may decrease porosity through mineral precipitation [*Lowell et al.*, 1993], which would increase seismic velocities.

The average velocities in the E-WV OSC are lower at all depths by 0.4 – 0.8 km/s than in the Cobb OSC (Figure 14a). This may reflect more intensive tectonic deformation associated with ongoing plate boundary reorganization at the northern end of the Endeavour segment [*Dziak*, 2006]. The lowest velocities in the model are in Middle Valley where they are 0.1 – 0.4 km/s slower than in the E-WV OSC (Figure 14a). Middle valley is blanketed by a significant layer of sediment [*Davis and Villinger*, 1992]. The sediment layer has a low velocity and its insulating effect may depress the velocities of the underlying basement. Ultrasonic measurements on mafic rocks suggest that the partial derivative of *P*-wave velocity with

temperature is -0.4 x 10^{-3} to -0.6 x 10^{-3} km s^{-1} K^{-1} [*Christensen*, 1979; *Kern and Tubia*, 1993] which is equivalent to a decrease in velocities of about 0.1 – 0.2 km/s for a 300°C temperature increase.

3.6.2 Upper crustal formation

The shallow ridge-parallel, alternating velocity anomalies in the segment center are thought to be caused by a combination of normal faults forming the rift valley and volcanic emplacement occurring in a wide zone of accretion. The upper 1 km of crust along the central axial valley and the adjacent bathymetric ridges is characterized by a series of ~4-km-wide linear anomalies that alternate between relatively high and low velocities (Figures 16 & 17). These variations are most simply interpreted in terms of variations in the thickness of layer 2A. The inversions have poor vertical resolution in the uppermost crust (see Appendix B) because rays do not turn in layer 2A, so variations in the thickness of this low velocity layer are mapped into anomalies that extend throughout the upper ~1 km.

At the Endeavour segment, periodic spacing of abyssal hills has been interpreted in terms of alternating episodes of enhanced volcanism and tectonic extension [*Kappel and Ryan*, 1986]. If layer 2A is interpreted as the layer of volcanic extrusives, this model predicts a variable thickness for layer 2A with thicker accumulations beneath the bathymetric ridges and less accumulation in between. Both a small tomographic experiment [*Barclay and Wilcock*, 2004] and MCS data [*Van Ark et al.*, 2007] have shown a thicker layer 2A beneath bathymetric highs. However, the results show a more nuanced structure with the low velocity anomalies centered beneath the outer flanks of the bathymetric highs (Figure 17). This observation is difficult to reconcile with a model in which the axial highs are simple volcanically constructed features.

An alternative model for the abyssal hills is that they formed as a result of inward-facing normal faults that are active during diking events [*Carbotte et al.*, 2006]. This model requires no fluctuations in the rate of volcanism; instead the faults are periodically distributed throughout the axial valley because new faults form only when the existing faults have rifted too far off-axis to be activated by dike-induced stresses. This model is more consistent with the observation that the abyssal hill topography forms along sections of the JdFR that are underlain by a steady-state AMC [*Carbotte et al.*, 2006]. It is also more consistent with observations provided that some volcanic eruptions extend outside the axial valley. Seafloor observations from the Cleft segment along the southern JdFR suggest that eruptions outside the axial valley are quite common [*Stakes et al.*, 2006]. The rotation of the foot wall that would accompany normal faulting would create a sloped seafloor that would lead to eruptions flowing down the outer slopes of the axial valley, thus thickening layer 2A. The magnitudes of the shallow velocity anomalies in the isotropic model require variations in layer 2A thickness of 150 – 200 m.

Another interesting feature of the shallow velocity structure is that it shows no evidence of high velocities on the spreading axis that would indicate a thinner layer 2A on-axis, which is consistent with *Van Ark et al.* [2007] who did not identify a systematic difference between the thicknesses of layer 2A on- and off-axis. In contrast, layer 2A systematically thickens up to a factor of three off-axis along the East Pacific Rise [*Toomey et al.*, 1990; *Detrick et al.*, 1993b; *Harding et al.*, 1993] and the southern Juan de Fuca Ridge [*Canales et al.*, 2005]. Stochastic modeling of dike emplacement and lava flows [*Hooft et al.*, 1996] shows that off-axis 2A thickening can be reconstructed using a narrow zone of accretion and a bimodal distribution of lava flows consisting of short-length, small-volume flows interspersed with high-volume eruptions that flow outside the accretion zone over the axial topography. At the Endeavour, the

lack of thickening of layer 2A near the ridge axis suggests that the axial lava flows presently extend over a region that is similar to the width of the accretion zone. To generate the thickening of layer 2A observed on the outer flanks of the abyssal hills, either the pattern of axial accretion is different than in the past or eruptions occur off-axis in a region that is separated from the axial accretionary zone.

3.6.3 Vent field structure

The data suggest that velocity differences beneath the vent fields are consistent with ongoing fracturing and mineral precipitation within the hydrothermal reaction zone. At 0 – 2 km depth, the velocities beneath the vent fields are on average 0.2 to 0.4 m/s higher than beneath the ridge axis to the north and south (Figure 17e). If the higher velocities result solely from temperature differences, then shallow temperatures would be required to be at least 300˚C lower in the vent fields [*Christensen*, 1979]. Although hydrothermal circulation will draw cold fluids into the crust, this explanation seems unlikely since models of high Rayleigh number hydrothermal circulation suggest that much of the volume infilled by circulation is warm [*Coumou et al.*, 2008]. A more plausible explanation is that the porosity is lower beneath the vent fields due to the effects of clogging by hydrothermal precipitation and alteration [*Lowell et al.*, 1993; *Wilcock and Delaney*, 1996; *Lowell et al.*, 2003]. Interestingly, the lowest velocities at 0 – 2 km depth in the vent field region locate midway between the Main Endeavour and High Rise fields, the two fields with the highest heat fluxes [*Kellogg*, 2011]. This suggests that porosity (and, by inference, permeability) might be higher in this region.

At depths of around 2 km the velocities are also markedly lower beneath the Main Endeavour and High Rise fields than the other fields (Figure 17e). This region lies just above the

AMC and coincides with the hydrothermal heat uptake zone. The low velocities below the Main Endeavour and High Rise fields coincide closely with a region of intense seismicity (Figure 22b) whose characteristics were interpreted in terms of cracking associated with magma chamber inflation [*Wilcock et al.*, 2009]. Thus, the low velocities may reflect enhanced porosity and fracturing in a region where the high rates of seismicity counteract the effects of hydrothermal clogging. Indeed, it is interesting to note that low velocities are also present at ~2 km depth several kilometers north of the vent fields (Y = 7 km in Figure 22b). This is also a region of intense seismicity (Figure 22c) that may be related to stresses induced by the interaction between the West Valley propagator and the Endeavour segment [*Weekly et al.*, 2013]. It is also possible that increased temperatures in the heat uptake zone associated with vigorous hydrothermal circulation may contribute to lower velocities beneath the Main Endeavour and High Rise fields.

3.6.4 Depth variations and cracks in the upper crust

This study is the first to investigate the three-dimensional spatial heterogeneity of anisotropy in the upper crust at a mid-ocean ridge. Previous tomographic studies of crustal anisotropy reported on either azimuthal variations in travel time residuals calculated from an isotropic velocity model or on the depth-dependence of the percentage anisotropy using a prescribed orientation [*Barclay et al.*, 1998; *Dunn and Toomey*, 2001; *Barclay and Wilcock*, 2004; *Tong et al.*, 2004; *Dunn et al.*, 2005]. Only one previous study [*Sohn et al.*, 1997] has reported three-dimensional variations in percent anisotropy, but that study used a fixed orientation.

These results are consistent with models that attribute seismic anisotropy in the upper oceanic crust to cracks aligned parallel to the ridge axis [*Stephen*, 1985; *Shearer and Orcutt*,

1986]. The observed decrease in anisotropy with depth is attributed to pore volume reductions due to crack closures resulting from increased lithostatic pressures while the observed decrease in anisotropy with distance from the ridge is consistent with infilling of cracks by the precipitation of minerals in the near-axis hydrothermal system. A clear azimuthal dependence in travel time residuals is observed in the isotropic inversion whose amplitude decreases with ray-turning depth (Figure 18). Additionally, the average percent anisotropy clearly decreases within the upper 2 km (Figure 19), suggesting that anisotropy is limited to the upper volcanic units and does not extend into the underlying gabbro. These results are similar to earlier tomography studies [*Barclay et al.*, 1998; *Dunn and Toomey*, 2001] that observed an azimuthal dependence in travel time residuals and attributed this relationship to vertical, water-filled cracks with an aspect ratio > 0.01 that align perpendicular to the spreading direction.

3.6.5 Off-axis variations in anisotropy

The observed decrease in anisotropy with distance from the ridge is consistent with infilling of cracks by the precipitation of minerals in the near-axis hydrothermal system. A remarkable feature of the inversion that has not been reported from inversions elsewhere is the rapid decrease in anisotropy away from the ridge axis. Above 2 km depth, the percentage anisotropy decreases to less than half of its value at the ridge axis within 8 km of the ridge axis (crustal ages of ~0.3 Ma) (Figure 20 – 21). At depths below 1 km, this decrease in anisotropy is accompanied by an increase in average isotropic velocities of 0.3 – 0.4 km/s (Figure 21). The inversions do not have good vertical resolution above 1 km since velocity anomalies at these shallow depths are influenced by local variations in the thickness of the low velocity layer 2A.

Using MCS data, *Newman et al.* [2011] found that velocities in the upper few hundred meters of layer 2B increase by an average of 0.8 km/s within 0.5 Ma. This evolution occurs much more rapidly than the increase in layer 2A velocities with age [*Nedimovic et al.*, 2008]. *Newman et al.* [2011] interpret the rapid layer 2B maturation as evidence for the infilling of cracks by the precipitation of minerals in the near-axis hydrothermal system. Our results show that the evolution of layer 2B velocities extends to the base of the sheeted dike layer and is consistent with this interpretation. Indeed, the infilling of ridge-parallel cracks is the only viable mechanism to reduce anisotropy with age. *Newman et al.* [2011] infer that crack infilling occurs in regions of hydrothermal downflow based on the distribution of layer 2B velocities in off-axis regions where the patterns of hydrothermal flow are known. This would lead to the inference that recharge associated with cooling newly formed crust extends several kilometers off-axis.

3.6.6 Along-axis variations in anisotropy

Along-axis variations in both the magnitude and orientation of anisotropy are consistent with tectonic processes. The orientation of the fast direction of anisotropy aligns perpendicular to spreading direction near the segment center but is rotated near segment ends (Figure 20d). There are significant along-axis variations in the magnitude of anisotropy on the spreading axis (Figure 20a-c). The highest values near Y = 15 km lie at the southern end of the E-WV OSC and are consistent with high levels of deformation within the OSC. High anisotropy between Y = 5 km and Y = 10 km coincides reasonably closely with a region of intense seismicity that has persisted following two swarms on the northern Endeavour in 2005. Anisotropy is also high beneath the vent fields (Figure 22a) suggesting that cracks may be strongly aligned along-axis in this region.

At the northern end of the Endeavour, the fast direction mirrors the curvature of the rotated limbs of the E-WV OSC while near the Cobb OSC, the orientation of the fast direction converges to the south, mirroring the decreased spacing of abyssal hills that reflects decreased spreading rates in the OSC. The curvature of adjacent limbs at OSCs towards one another is a common feature of en echelon ridge segments [*Macdonald et al.*, 1987; *Macdonald et al.*, 1991] and is consistent with crack propagation theory [*Pollard and Aydin*, 1984]. Unlike at 9˚03'N OSC along the East Pacific Rise, the orientation of seismic anisotropy is consistent with depth and no rotation in anisotropy between the upper extrusive unit and the underlying dike layer is observed [*Tong et al.*, 2004].

3.7 Conclusions

This tomographic study on the Endeavour segment of the JdFR provides some of the most detailed three-dimensional observations of upper crustal seismic velocity and anisotropy obtained to date over a spreading center. The segment includes both a central portion that hosts a mid-crustal axial magma chamber and vigorous hydrothermal systems and two large overlapping spreading centers at the segment ends. The results thus provide insights into the role of magmatism, tectonism and hydrothermal circulation in constructing the oceanic crust. The primary conclusions of this study are:

- Upper crustal *P*-wave velocities near the center of the Endeavour segment are, on average, 1.0 – 1.5 km/s higher than near the segment ends. These variations are attributed to increased porosities at segment ends due to extensive tectonic fracturing within overlapping spreading centers and possibly the infilling of cracks by precipitation of minerals along the hydrothermally active central portion of the segment.

- The upper 1.0 km of crustal velocity structure near the segment center is imprinted with a pattern of alternating velocity anomalies extending 10–12 km off-axis that are oriented parallel to the ridge axis. The low-velocity bands coincide with the outer flanks of off-axis abyssal hills. This pattern is attributed to localized thickening of the extrusives by eruptions that extend outside the axial valley and flow down the fault tilted blocks that form the abyssal hill topography [*Carbotte et al.*, 2006].
- Velocities are generally higher beneath the hydrothermal vent fields than along the spreading axis to the north and south. This is interpreted as evidence of reduced porosity due to mineral precipitation from hydrothermal circulation.
- Low velocities just above the AMC beneath the High Rise and Main Endeavour fields relative to other vent fields coincide with a region of intense seismicity and may reflect increased porosity and higher temperatures in the heat uptake zone beneath the most vigorous vent fields.
- The percentage of seismic anisotropy decreases, on average, from ~7% in the upper 1 km crust to 2% below 2.5 km depth. Depth-dependent decreases in anisotropy are attributed to the closure of cracks from a combination of lithospheric overburden pressure and hydrothermal mineral precipitation.
- Seismic anisotropy decreases at all crustal depths away from the ridge-spreading axis within 8 km (~0.3 Ma) and is accompanied by an increase in velocities below 1 km depth. This observation is consistent with rapid mineral infilling of cracks within layer 2B due to hydrothermal circulation near the ridge axis [*Newman et al.*, 2011].
- The magnitude of seismic anisotropy is greatest in a region located at the southern limit of the E-WV OSC, where the percentage of anisotropy exceeds 15% in the shallow crust.

Localized variations in anisotropy are attributed to intense deformation within the upper crust related to earthquake faulting and cracking.

- The fast direction of anisotropy is oriented ridge-parallel along the central Endeavour. This is consistent with the orientation of minimal compressive stress being aligned perpendicular to spreading direction. However, near the OSCs, the orientation of anisotropy reflects the tectonic fabric of the seafloor and is influenced by the interaction of stresses from adjacent limbs of the OSC.

Figure 11. Bathymetric map of the Endeavour segment with the primary tectonic and volcanic features labeled and showing the traces of the Northern Symmetric, Endeavour and West Valley segments and the failed Middle Valley segment (bold black lines), an elevated region centered on the central portion of the Endeavour Ridge (faint black box), the outline of the inversion area for the tomography experiment (bold black dashed box) and the area shown in Figure 15 (bold black dotted box).

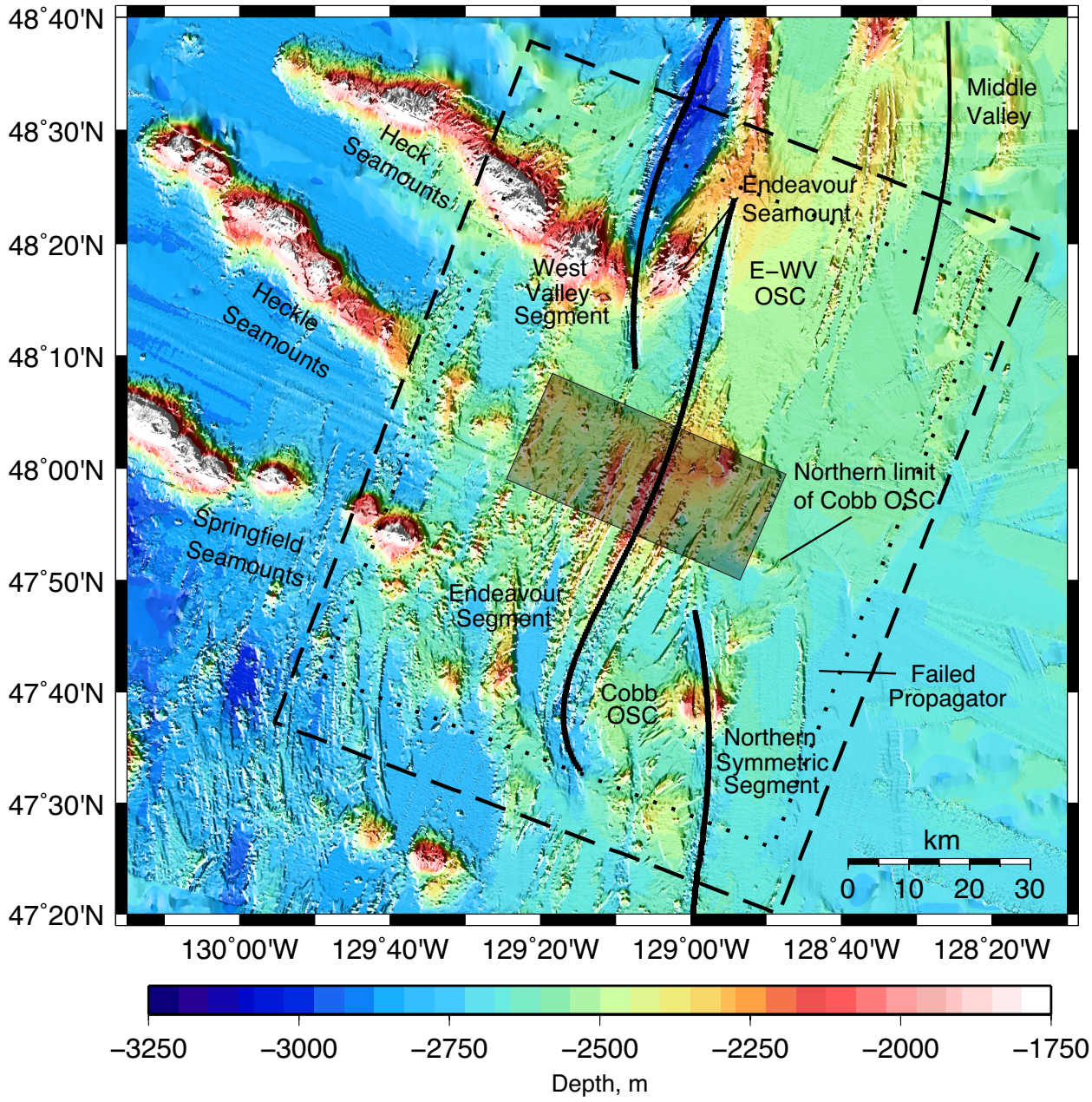

Figure 12. Configuration of the tomography experiment showing the location of over 5,500 shots from the 36-element airgun array of the *R/V Marcus G. Langseth* (black dots) and 64 sites at which OBS from the U.S. Ocean Bottom Seismograph Instrument Pool were deployed (white circles and triangles denote instruments operated by Scripps Institution of Oceanography and Woods Hole Oceanographic Institution, respectively). Three bold solid black lines and a filled black circle show shots and an OBS, respectively, for the record sections displayed in Figure 13. Rectangles show locations of averaged vertical velocity profiles displayed in Figure 14 for the flanks of the central Endeavour (blue) and the segment ends (red). The bold black dashed line shows the outline of the inversion area also shown in Figure 11.

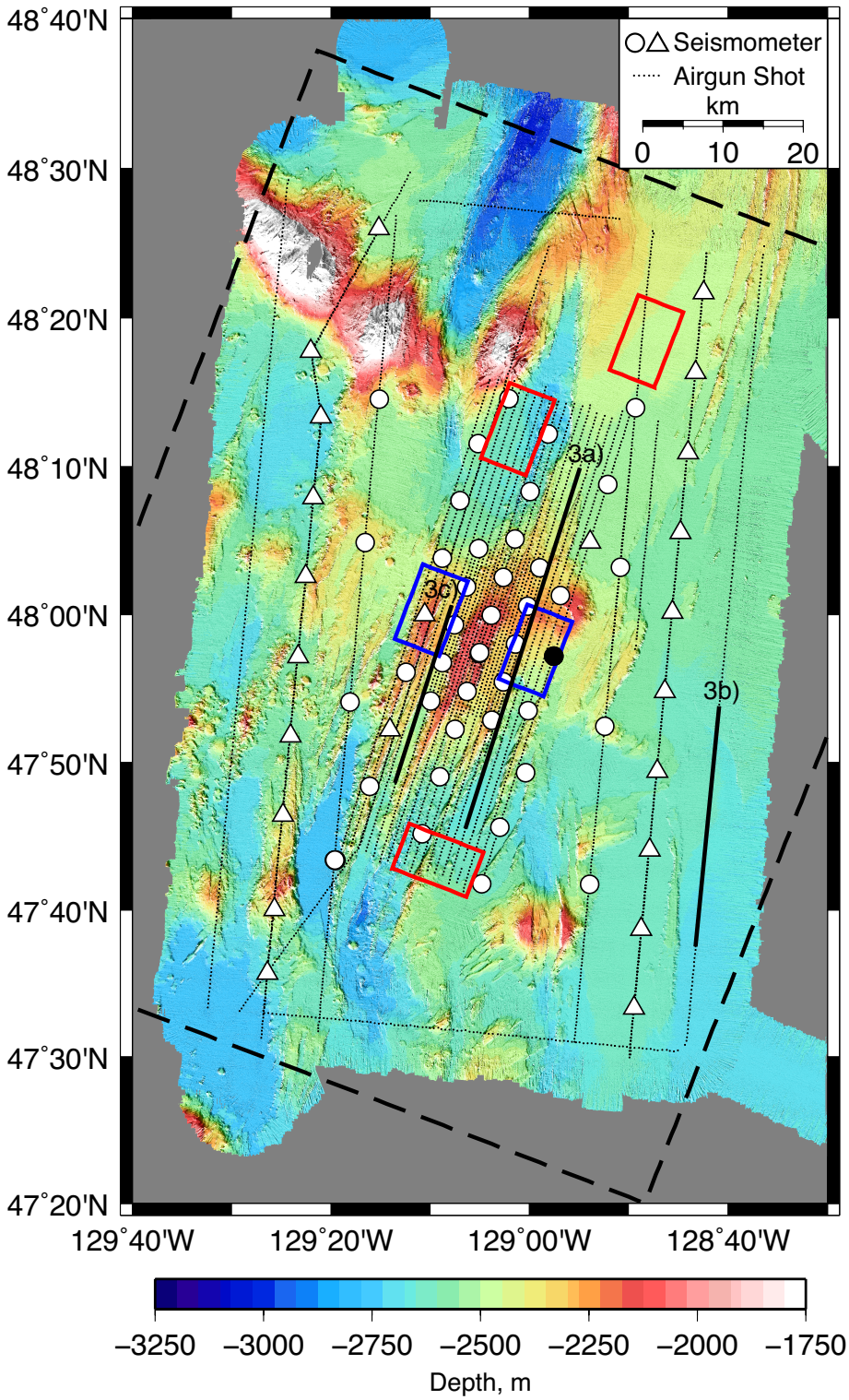

Figure 13. Example record sections with *Pg* travel time picks (red lines with dotted lines showing assigned picking errors) used for tomographic inversions. Waveform data recorded from the shot lines indicated on Figure 12 are bandpass filtered between 4 and 30 Hz. The shots are spaced uniformly 500 m apart along the shot lines, the horizontal axis is labeled with the shot-receiver range and a reduction velocity of 6 km/s is applied. (a-b) For non-ridge-crossing lines, the most impulsive arrivals are observed at ranges less than 15 km (a) but picks can often be obtained to ranges exceeding 30 km (b). (c) Ridge-crossing lines show more complicated arrivals with lower signal to noise, particularly beyond 15 km, and are typically picked to shorter ranges and with higher uncertainties.

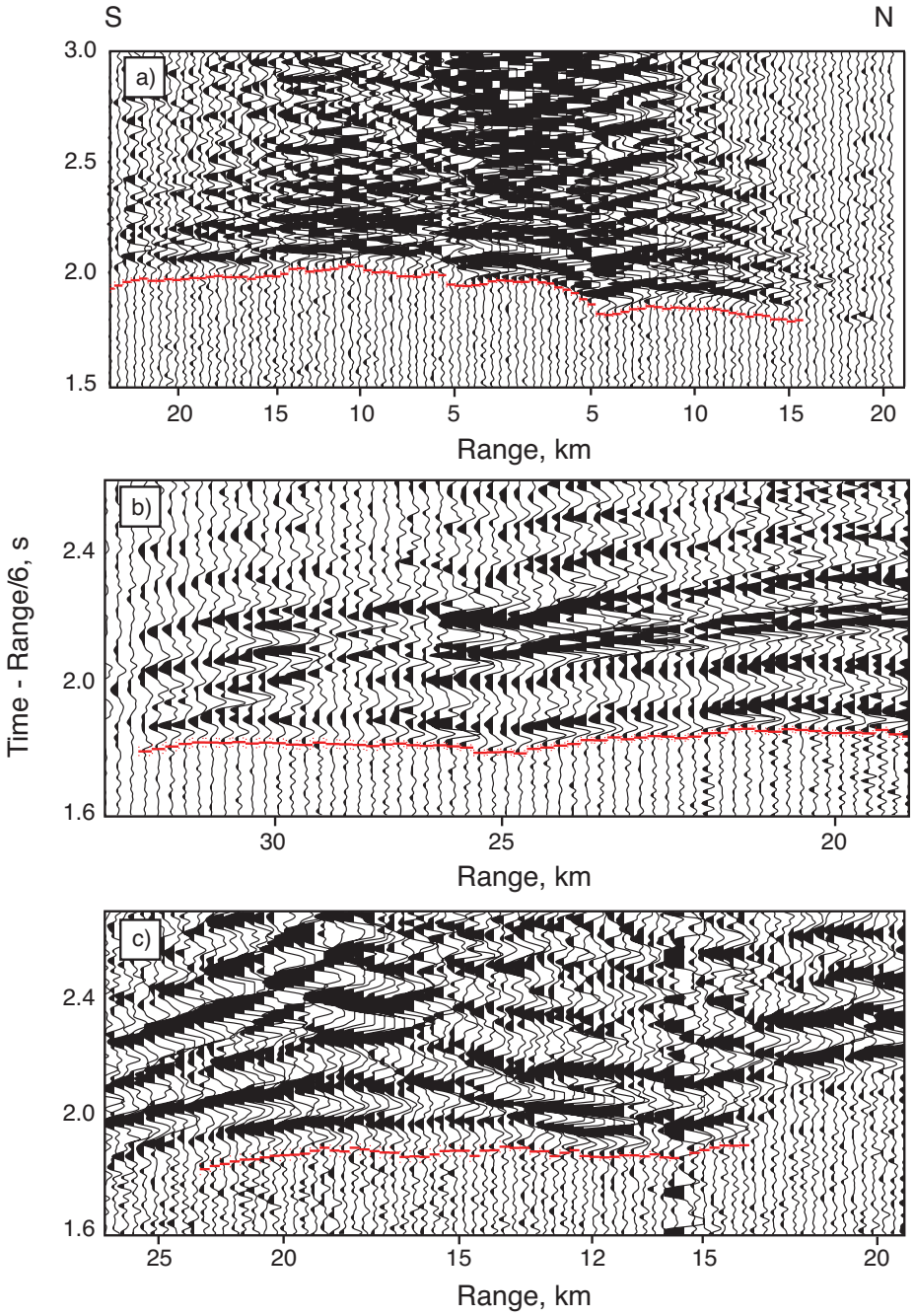

Figure 14. (a) The starting one-dimensional velocity model for the inversions (black dashed), derived from *Cudrak and Clowes* [1993], the horizontal average of the preferred isotropic model used to plot anomalies (black solid), and vertical profiles for the flanks of the central Endeavour (blue) and for the overlapping spreading centers and southern end of Middle Valley (red) obtained from horizontal averaging the 5-by-10 km regions shown by boxes in Figure 12. (b) Comparison of velocity profiles from this study with example velocity profiles obtained from 8°-10°N on the East Pacific Rise (EPR) [*Canales et al.*, 2003] (green). Profiles from *Canales et al.* [2003] are for the west flank of the EPR near 9°10'N in the wake of the 9°03'N OSC and for the east flank near 9°50'N away from segment boundaries. (c) Comparison of velocity profiles from this study with example profiles obtained from three segments lying between the Oceanographer and Hayes Fracture Zones (33°30'N – 35°30'N) on the Mid-Atlantic Ridge [*Hooft et al.*, 2000] (green). Profiles from *Hooft et al.* [2000] are from the center of the OH1 segment, the northern end of the OH2 segment and just south of the Oceanographer Fracture Zone (labeled OFZ).

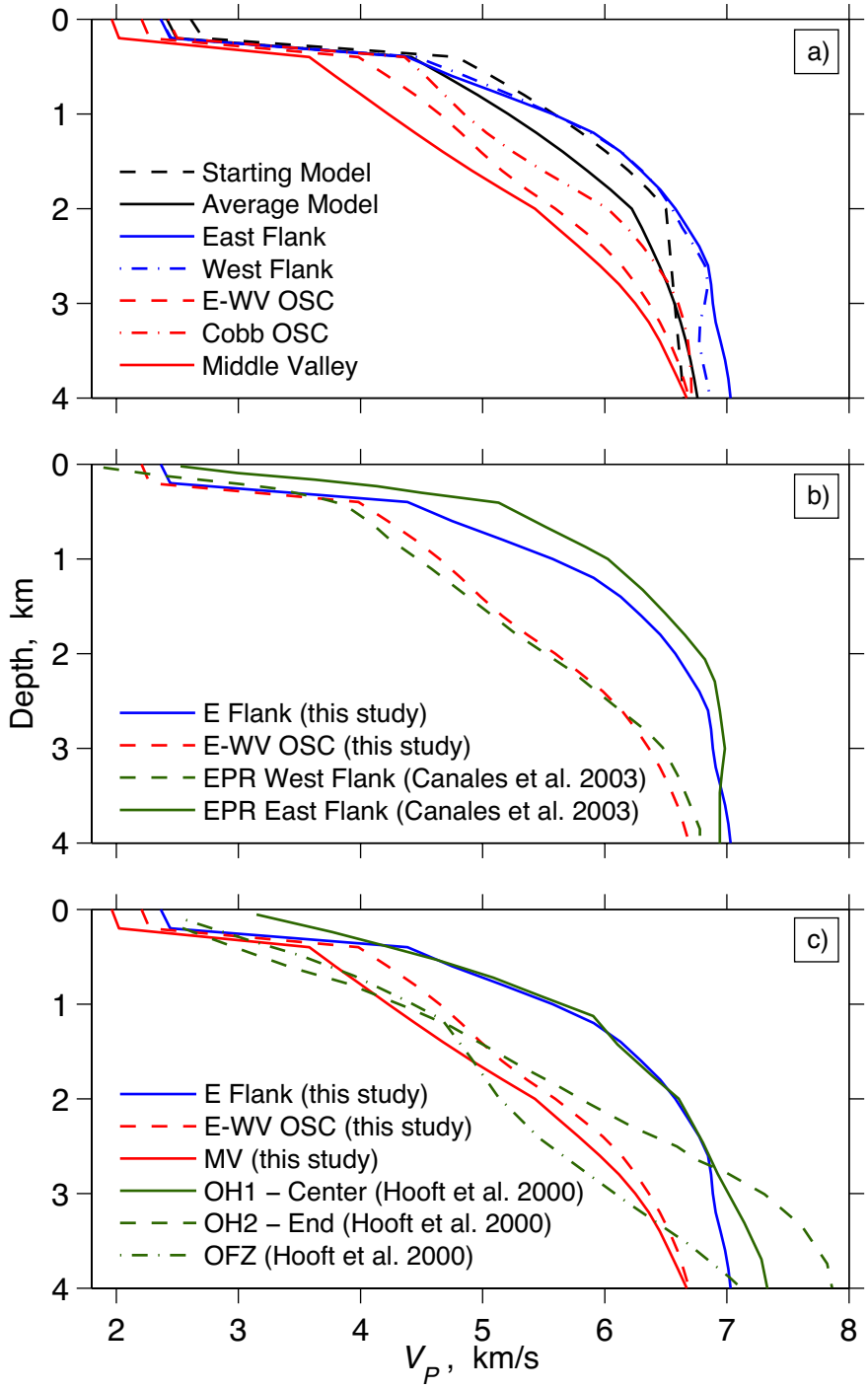

Figure 15. (a-g) Map view sections of three-dimensional segment-scale isotropic velocity anomalies relative to the horizontally averaged model (black solid line in Figure 14a). The area covered by the plots is shown by a dotted line in Figure 11. Horizontal slices of the inversion volume are presented at 0.4 km depth intervals and masked in regions where the derivative weight sum (DWS) is less than 10 (see Appendix B). The contour interval for velocity perturbations is 0.2 km/s. The traces of the segments are shown by bold black lines and the vent fields by green stars. (h) Shaded bathymetric map of the area shown in a-g showing the location of high-temperature vent fields (green stars). Red and blue boxes show regions used for calculating the average vertical velocity profiles in Figure 14a and the black dashed box shows the area covered by Figure 16.

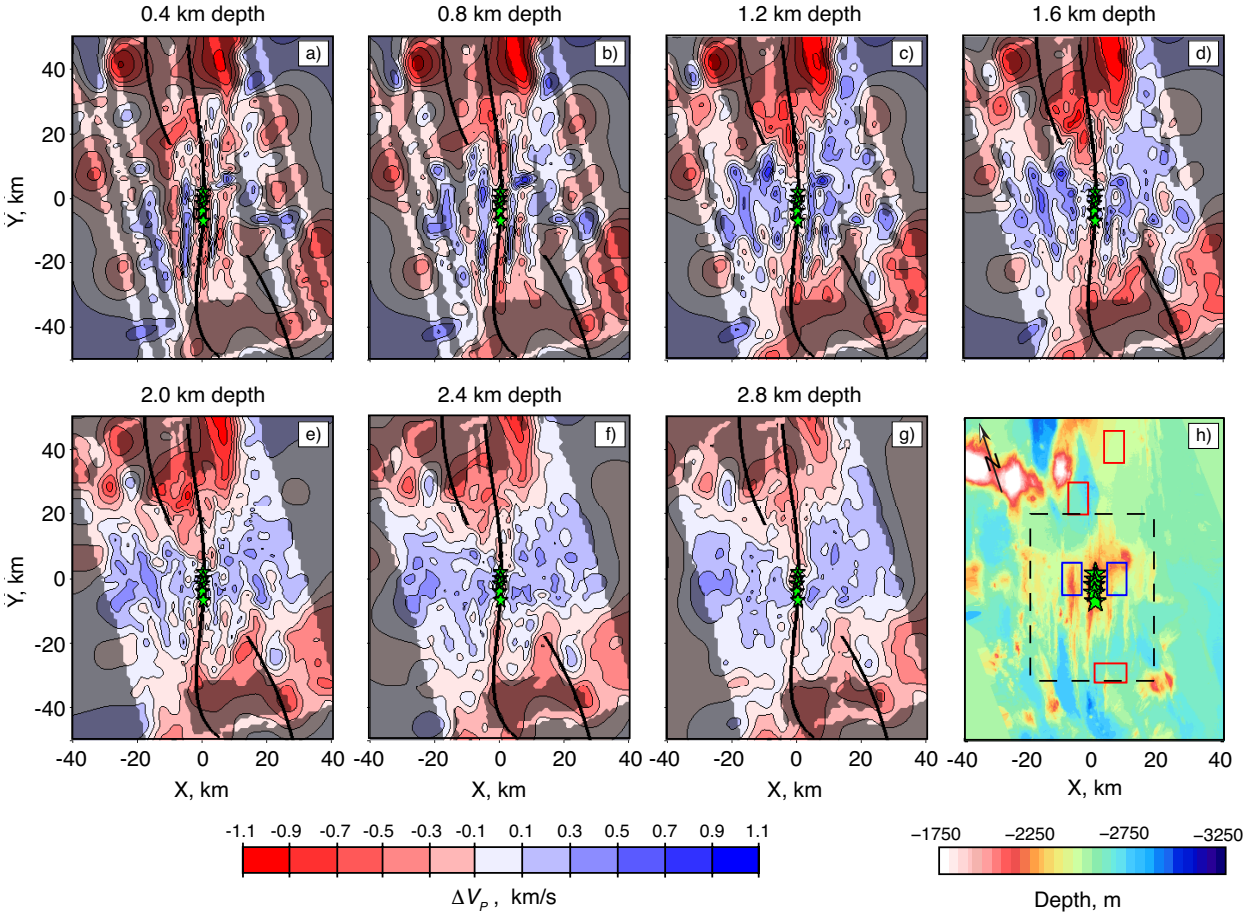

Figure 16. Velocity anomalies and bathymetry within the central portion of the Endeavour segment plotted with the same conventions as in Figure 15.

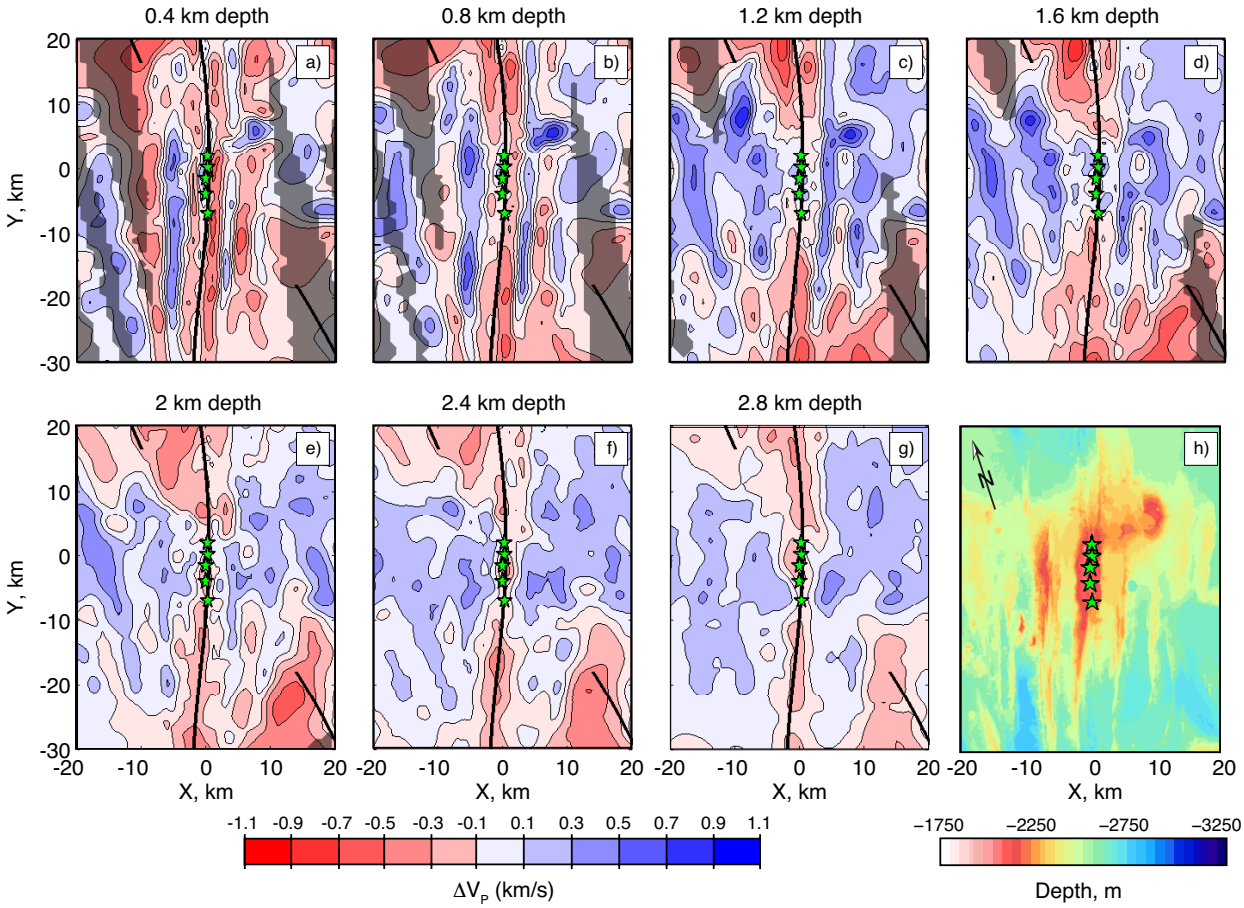

Figure 17. Vertical sections showing velocity anomalies for the central portion of the Endeavour. (a) Shaded bathymetric map showing the locations of the vertical sections (dashed lines) and vent fields (labeled green stars). (b-d) Vertical sections crossing the ridge-axis at (b) Y = -6 km near the Mothra field, (c) Y = -2 km near the Main Endeavour field, and (d) Y = 2 km near the Sasquatch field. (e) Vertical section along the ridge-axis showing vent fields (green stars) and the position of the AMC (shaded region) obtained by converting two way travel times to the AMC [*Van Ark et al.*, 2007] to depth assuming the starting velocity model for the inversions.

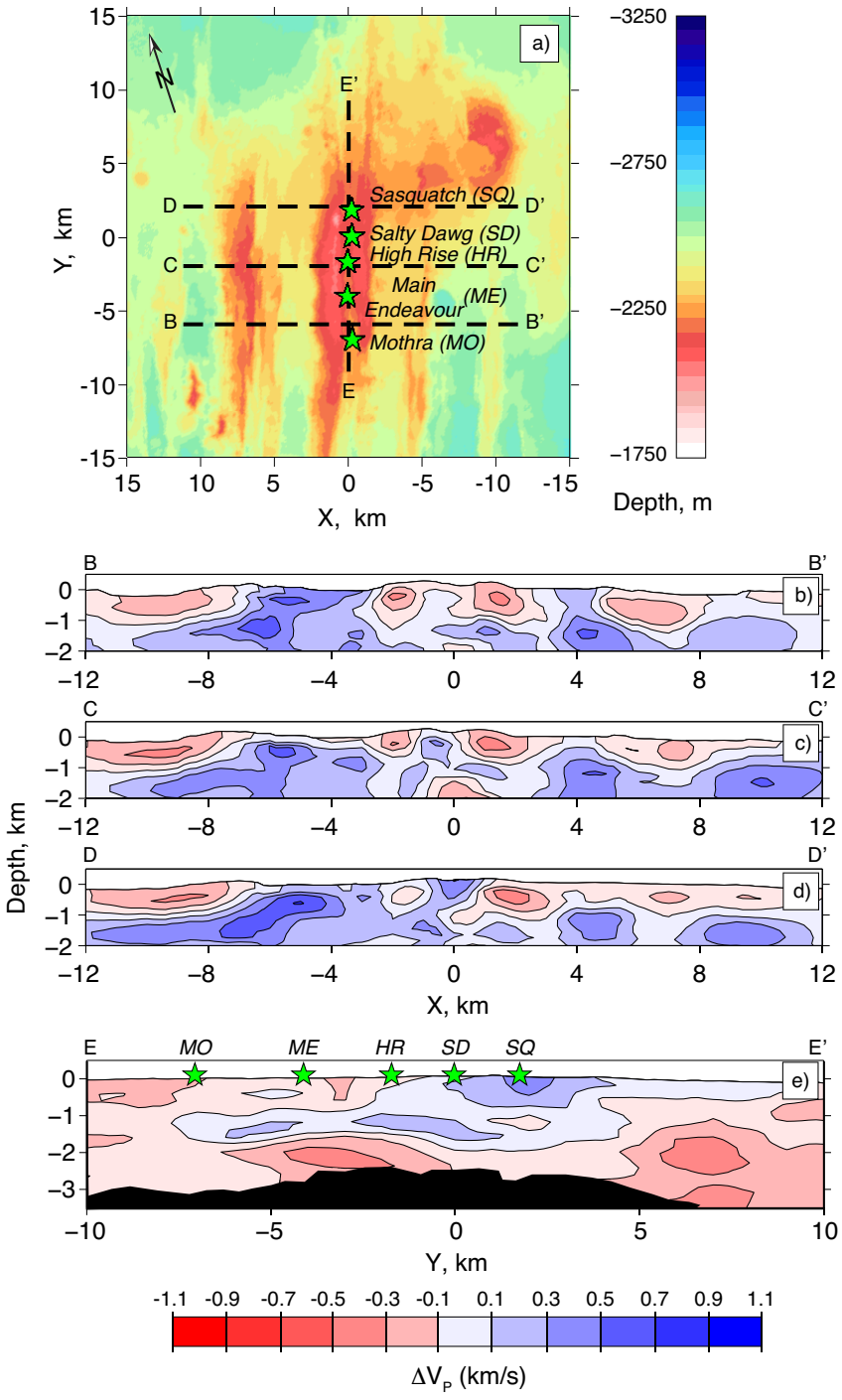

Figure 18. Mean travel time residuals for the preferred isotropic model plotted against azimuth for rays turning between (a) 0 – 1 km depth, (b) 1 – 2 km depth, and (c) 2 – 3 km depth. Residuals are averaged in 20˚ azimuth bins and error bars show the 1-σ standard error of the mean. Azimuths are plotted as degrees clockwise from the y-axis of the inversion grid, which is parallel to the strike of the central Endeavour and rotated 21˚ clockwise from north). Solid lines depict cosine curves of the form $a \cos(2\theta + b)$ that have been fit to the data using a least-squares approach.

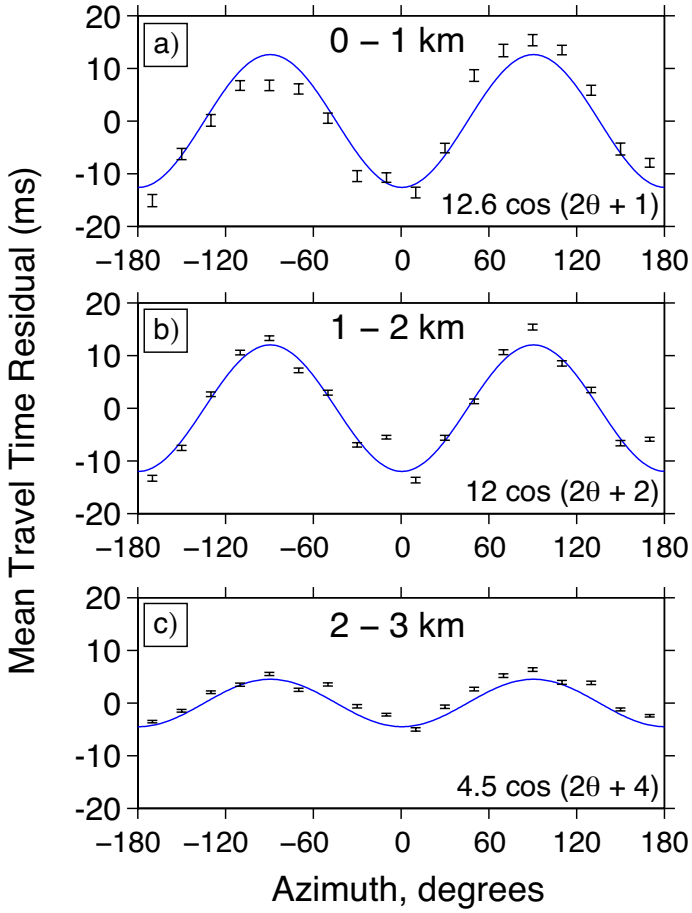

Figure 19. Average vertical profile of percent anisotropy recovered by the inversion within 10 km of either side of the ridge-axis and between Y = -20 km and Y = 20 km.

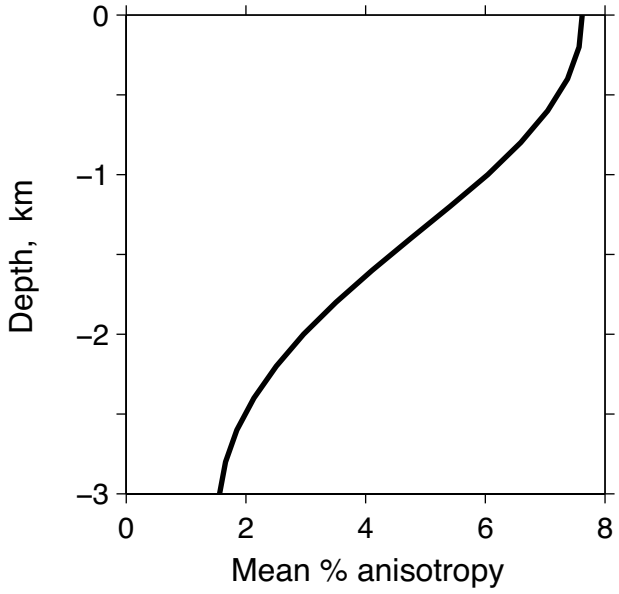

Figure 20. Map-view sections of the central Endeavour showing the magnitude of anisotropy at (a) 0.4 km depth, (b) 1.0 km depth, and (c) 1.6 km depth. Images are contoured at 2% intervals. (d) Map of the central Endeavour segment showing orientation and magnitude of seismic anisotropy at 0.4 km depth with ticks showing the fast direction and tick lengths scaled to the magnitude of anisotropy. The traces of segments (bold cyan lines in a-c and black lines in d) and vent fields (green stars) are also shown.

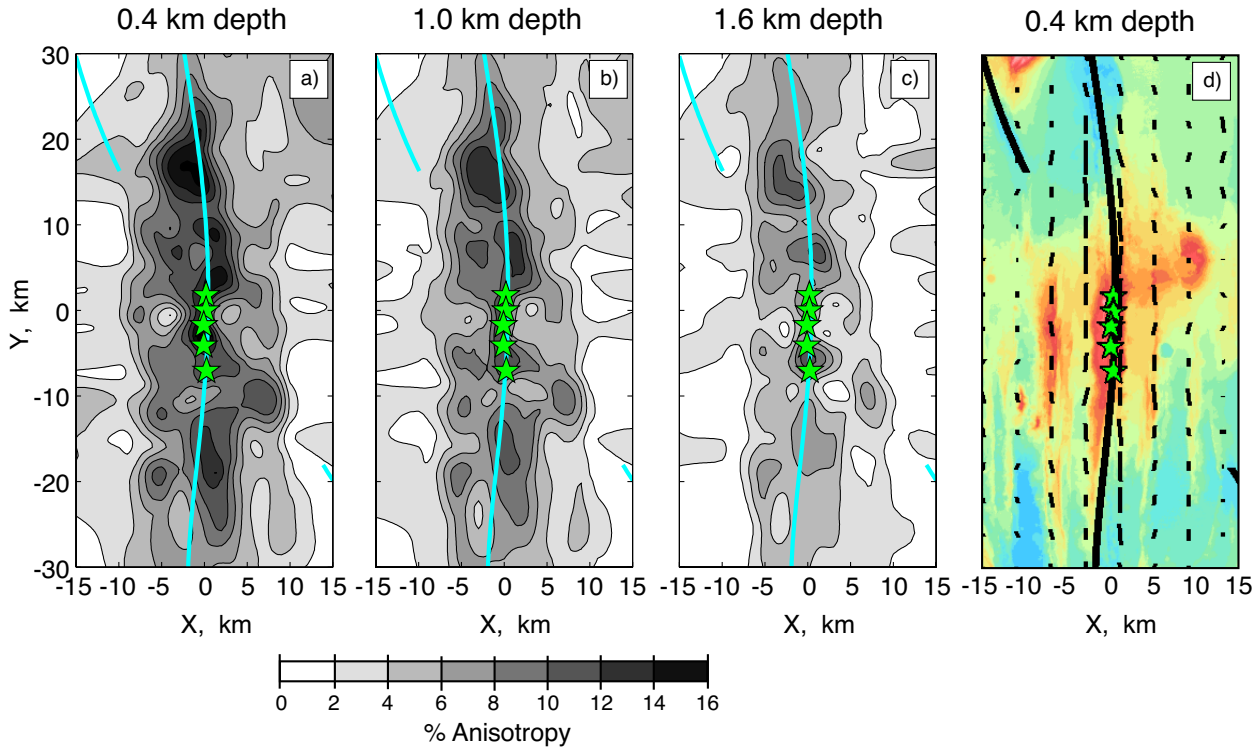

Figure 21. Plots showing the change in average isotropic velocity (blue lines) and magnitude of anisotropy (red lines) away from the ridge-axis of the central Endeavour at six depths (labeled). Average values were calculated at each depth within 40-km-long sections oriented in a ridge-parallel direction (-20 km < Y < 20 km).

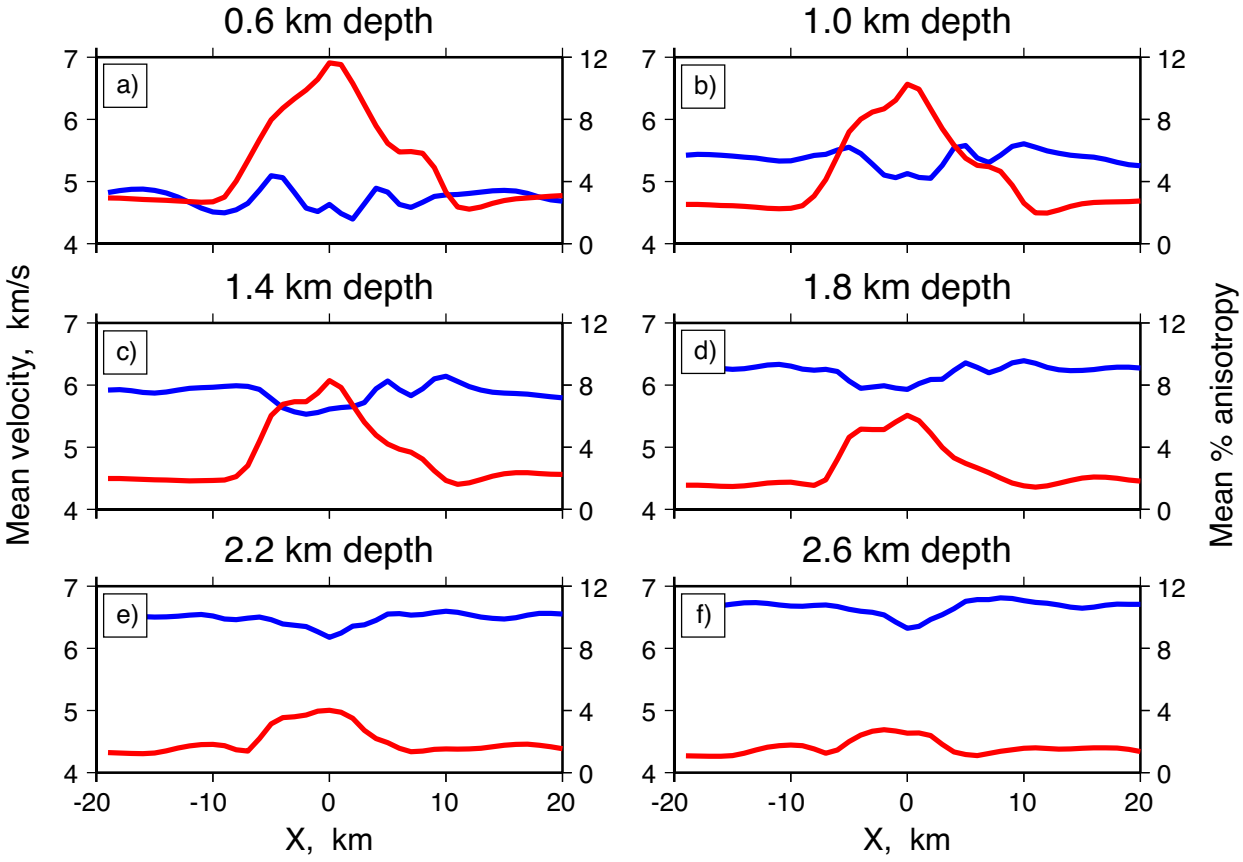

Figure 22. (a) Along-axis (X = 0 km) vertical cross-section showing the percentage anisotropy for the region extending from Y = -10 to Y = 10 km. Locations of earthquakes between 2003 and 2004 (red dots) were obtained using double-difference techniques [*Wilcock et al.*, 2009]. The gray shaded region shows structure located below the roof of the AMC. (b) As for (a), but with the magnitude of isotropic velocity anomalies for the preferred model plotted relative to the average velocity structure shown in Figure 14a. (c) Histogram of ~6,000 earthquakes from 2003 – 2006 located within 2 km of the ridge [*Weekly et al.*, 2013]. The earthquakes are binned in 0.5 km increments along the Y-axis.

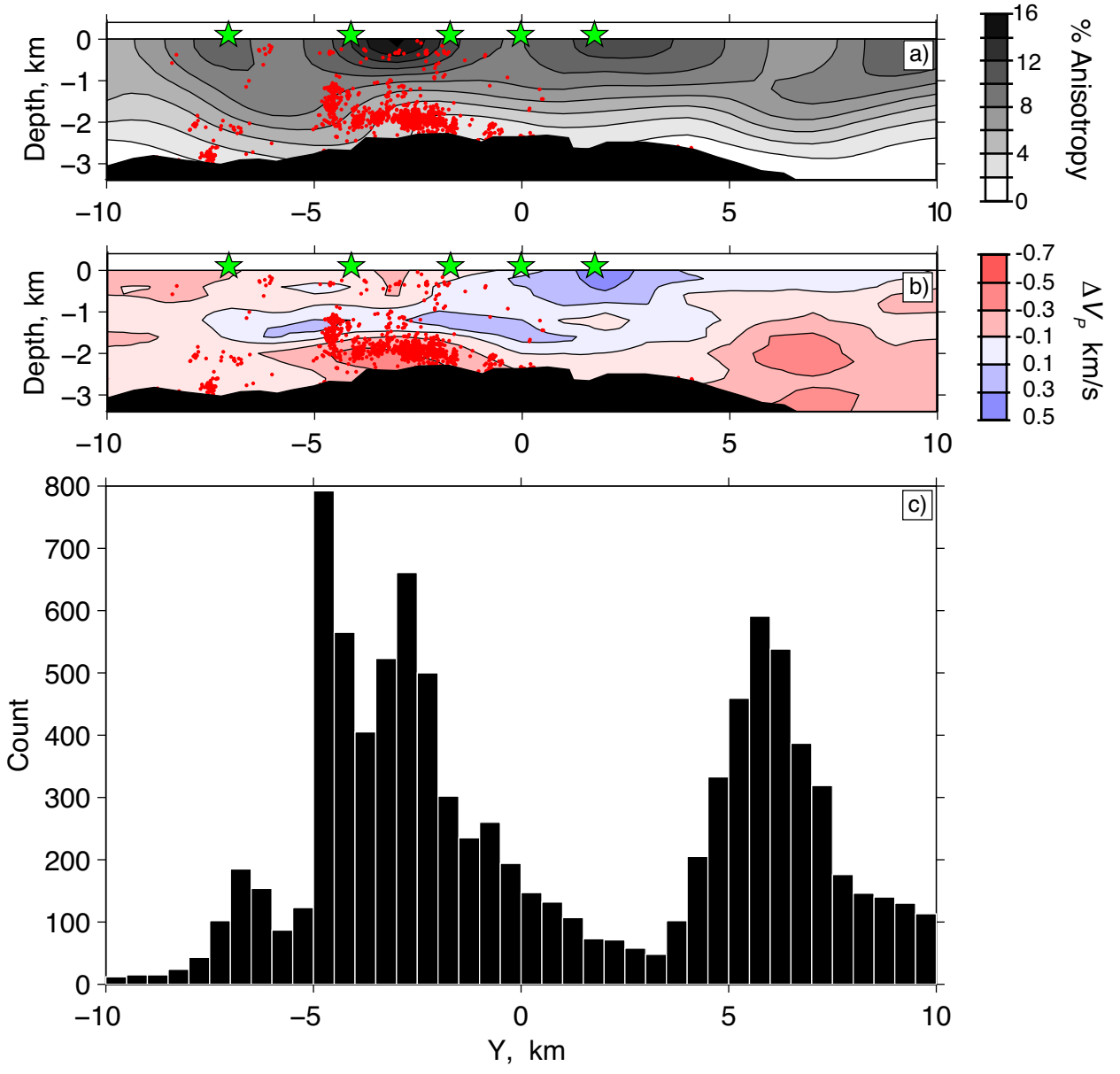

Chapter 4

CONCLUSIONS

The previous chapters report observations of seismicity and shallow crustal seismic structure from the Endeavour segment of the Juan de Fuca Ridge. The results are interpreted in the context of how tectonic extension, episodic magmatism, and hydrothermal circulation influence crustal accretion at an intermediate-spreading rate mid-ocean ridge segment. A three-year catalog of seismicity between 2003-2006 is one of the largest marine earthquake datasets collected to date and features the first *in-situ* recording of a magmatic spreading event along the Endeavour segment captured by an ocean-bottom seismometer network. The segment-scale active source tomography experiment conducted in 2009 produced segment-scale images of the three-dimensional isotropic and, for the first time, anisotropic velocity structure. These experiments allowed me to answer the following questions related to mid-ocean ridges:

- What are the roles of volcanic and tectonic processes in the formation of ocean crust?
- How do relative contributions of these processes to crustal accretion vary along a spreading segment?
- How do geological processes focus hydrothermal heat loss at a mid-ocean ridge segment?

4.1 Endeavour seismicity from 2003 – 2006

A catalog of earthquakes documenting seismic activity along the Endeavour segment from 2003 – 2006 includes two large regional seismic swarms in January and February 2005 that mark an episode of magmatic intrusion associated with ridge-spreading. Based on previous hydroacoustic studies of regional seismicity, similar types of spreading events may repeat on a decadal timescale [*Dziak et al.*, 2011]. The complex rupture patterns associated with the swarms

are attributed to extensive triggered seismicity along adjacent limbs of the Endeavour – West Valley OSC and the ambiguous partitioning of magmatic spreading between the southern extension of the West Valley segment and the northern Endeavour segment. The duration of the swarms, the southward migration of epicenters during the February swarm, and the lack of a discernible mainshock are consistent with intrusive magmatic activity. Based on the epicentral migration direction, it is highly unlikely that the magma was sourced from the AMC associated with the elevated central portion of the Endeavour segment [*Van Ark et al.*, 2007], and alternatively, could have originated from the magma source associated with the Heck Seamounts at the northern end of the segment.

The earthquake catalog contains extensive seismic triggering occurring over a wide range of spatial and temporal scales that lead to long-term changes in seismicity rates along the Endeavour segment. During both the January and February swarms, seismicity is observed in multiple regions along the northern Endeavour, southern West Valley, and vent field regions. Following the February 2005 swarm, the average post-swarm seismicity rate along the Endeavour segment decreased to ~15% of pre-swarm levels. In addition, seismicity rates at the ends of the Endeavour segment decreased to nearly zero while rates along the adjacent limbs of the respective OSCs remained unchanged. The potential for dynamic stress transfer contributing to changes in seismicity rates is explored, but ultimately discounted, due to decreased seismic activity observed at the ends of the Endeavour segment following the 2005 swarms. Instead, changes in post-swarm seismicity rates are attributed to negative static stress transfer along the entire Endeavour segment and reflect segment-scale relief of extensional stresses associated with ridge-spreading.

4.2 Seismic velocity structure of the Endeavour segment

Travel-time data from crustal refraction phases are inverted to investigate the three-dimensional isotropic and anisotropic velocity structure of an intermediate-spreading rate mid-ocean ridge segment for the first time. The tomographic images represent a time-integrated history of crustal accretion along the Endeavour segment extending up to ~1 Ma away from the ridge-axis.

The isotropic velocity structure includes anomalously low velocities near the segment ends that are > 1.0 km/s slower than velocities found near the segment center. These anomalies are indicative of increased fracturing of the oceanic crust within the OSCs compared to the magmatic central portion of the segment. Within the upper ~1 km of crust, a series of ridge-parallel banded anomalies extend 10 – 12 km away from the axial valley to the adjacent set of abyssal bathymetric ridges. The lowest velocities locate on the flankward side of these ridges and are interpreted as localized thickening of seismic layer 2A. Crustal accretion models favoring episodic periods of relatively high magma supply to the ridge crest would predict thickening of layer 2A directly beneath the bathymetric highs [*Kappel and Ryan*, 1986]. Instead, the offset between peak low-velocity anomalies and the bathymetric apex favors a model where layer 2A thickens from off-axis magmatic eruptions that are emplaced near the peak of the ridge and subsequently flow down the fault-tilted blocks that form the abyssal hill topography [*Carbotte et al.*, 2006].

Images of the three-dimensional anisotropic seismic structure provide new constraints on the distribution and evolution of cracks that pervade the upper oceanic crust. The average one-dimensional anisotropic structure decreases, on average, from ~7% in the upper 1 km crust to 2% below 2.5 km depth. This depth-dependent decrease is attributed to the closure of cracks within

the upper volcanic layers from a combination of lithospheric overburden pressure. The three-dimensional anisotropic structure of the central Endeavour segment is characterized by a ~15-km-wide (0.2 – 0.3 Ma) zone of high anisotropy (>10%) that shows significant along-axis variation. Outside of this narrow region, the average percentage of anisotropy rapidly decreases to ~2% at all depths. Coincidentally, this decrease in anisotropy is accompanied by a 0.3 – 0.4 km/s increase in isotropic seismic velocities at depths below 1 km. The changes related to isotropic and anisotropic structure at depth are associated with crack closure and cementation of the low-porosity intrusive dike layer. These observations are consistent with a recent multichannel seismic investigation that attributed increased velocities in seismic layer 2B within 0.5 Ma of the ridge axis to infilling of cracks in the near-axis hydrothermal system to mineral precipitation [*Newman et al.*, 2011].

4.3 Investigating crustal cracking using microearthquake monitoring and tomography

The experiments described within this dissertation provide a unique opportunity to investigate the interaction between subsurface geologic processes that contribute to crustal accretion using distinct marine seismological datasets that were collected along a common spreading segment. One of the more remarkable results to emerge from these studies is the correlation between seismic activity, slow isotropic velocities, and high anisotropy. Two regions of the study area where this relationship is particularly evident are the northern E–WV OSC and the hydrothermal vent fields within the axial valley. The broad area near the southern extension of the West Valley segment marks the termination of the February 2005 seismic swarm, a zone of anomalously low crustal velocities, and a locus of high anisotropy. These observations are all consistent with the notion that oceanic crust formed at OSCs is more highly fractured and has a

higher permeability than oceanic crust formed elsewhere. Similarly, the extensive seismicity, low velocities, and high amounts of anisotropy beneath the Main Endeavour and High Rise vent fields indicate ongoing cracking at shallow depths above the AMC. An additional constraint is provided by correlating the seismic activity to thermal output measured at each of the vent fields. Generally, the higher seismicity rates are observed beneath the Main Endeavour and High Rise vent fields, which also exhibit the highest heat flux [*Kellogg*, 2011]. The seismic and hydrographic data thus strongly suggest that cracking the upper crust by stresses induced by plate-spreading is a critical control on the permeability of young oceanic crust and plays a vital role in maintaining hydrothermal fluid circulation and extracting heat from the magma chamber.

4.4 Future Work

While the merit of this research can stand on its own right, there are several avenues of potential future research that could be explored using these results as a basis. With the advent of cabled seafloor observatories that utilize ocean bottom seismometers, such as the Regional Scale Nodes and Neptune Canada, there will be an acute need for efficient, rapid processing of marine earthquake data and the automated algorithm described in chapter 2 has strong potential to fulfill this need. The unique geometry of the tomography experiment described in chapter 3 has the capacity to image seismic structure extending much deeper than the shallow crust. The isotropic velocity model can be used as a starting point for exploring variations in crustal thickness and the anisotropic structure of the mantle. There is also great scientific potential to be realized in combining these datasets. Questions still remain about the rupture sequence of the 2005 seismic swarms, and using double-difference relocation techniques with a three-dimensional velocity model may illuminate patterns in the distribution of epicenters that the techniques described in

this dissertation are unable to resolve. Lastly, performing a joint inversion of the hypocenter and travel time data could effectively reduce some of the systematic biases that result from processing these datasets separately.

BIBILOGRAPHY

Barclay, A. H., and W. S. D. Wilcock (2004), Upper crustal seismic velocity structure and microearthquake depths at the Endeavour segment, Juan de Fuca Ridge, *Geochem. Geophys. Geosyst.*, *5*, Q01004, doi:10.1.1029/2003GC000604.

Barclay, A. H., D. R. Toomey, and S. C. Solomon (1998), Seismic structure and crustal magmatism at the Mid-Atlantic Ridge, 35˚N, *J. Geophys. Res*, *103*(B8), 17827-17844, doi:10.1029/98JB01275.

Barclay, A. H., D. R. Toomey, and S. C. Solomon (2001), Microearthquake characteristics and crustal V_P/V_S structure at the Mid-Atlantic Ridge, 35°N, *J. Geophys. Res.*, *106*(B2), 2017-2034.

Bazin, S., H. van Avendonk, A. J. Harding, J. A. Orcutt, J. P. Canales, R. S. Detrick, and M. Grp (1998), Crustal structure of the flanks of the East Pacific Rise: Implications for overlapping spreading centers, *Geophys. Res. Lett.*, *25*(12), 2213-2216, doi:10.1029/98GL51590.

Bazin, S., et al. (2001), Three-dimensional shallow crustal emplacement at the 9°03'N overlapping spreading center on the East Pacific Rise: Correlations between magnetization and tomographic images, *J. Geophys. Res.*, *106*(B8), 16101-16117, doi:10.1029/2001JB000371.

Begnaud, M. L., J. S. McCain, G. A. Barth, J. A. Orcutt, and A. J. Harding (1997), Structure of the eastern Clipperton ridge-transform intersection, East Pacific Rise from three-dimensional seismic tomography, *Eos Trans. AGU*, *78*(46, Suppl.), 675-675.

Bohnenstiehl, D. R., M. Tolstoy, R. P. Dziak, C. G. Fox, and D. K. Smith (2002), Aftershock sequences in the mid-ocean ridge environment: an analysis using hydroacoustic data, *Tectonophysics*, *354*(1-2), 49-70, doi:10.1016/S0040-1951(02)00289-5.

Bohnenstiehl, D. R., R. P. Dziak, M. Tolstoy, C. G. Fox, and M. Fowler (2004), Temporal and spatial history of the 1999-2000 Endeavour Segment seismic series, Juan de Fuca Ridge, *Geochem. Geophys. Geosyst.*, *5*(9), Q09003, doi:09010.01029/02004gc000735.

Brodsky, E. E., and S. G. Prejean (2005), New constraints on mechanisms of remotely triggered seismicity at Long Valley Caldera, *J. Geophys. Res.*, *110*(B4), B04032, doi:04010.01029/02004JB003211.

Brune, J. N. (1970), Tectonic stress and the spectra of seismic shear waves from earthquakes, *J. Geophys. Res.*, *75*(26), 4997-5009, doi:10.1029/JB075i026p04997.

Buck, W. R., S. M. Carbotte, and C. Mutter (1997), Controls on extrusion at mid-ocean ridges, *Geology*, *25*(10), 935-938.

Butterfield, D. A., R. E. McDuff, M. J. Mottl, M. D. Lilley, J. E. Lupton, and G. J. Massoth (1994), Gradients in the composition of hydrothermal fluids from the Endeavour Segment vent field - Phase-separation and brine loss, *J. Geophys. Res.*, *99*(B5), 9561-9583, doi:10.1029/93JB03132.

Canales, J. P., R. S. Detrick, D. R. Toomey, and W. S. D. Wilcock (2003), Segment-scale variations in the crustal structure of 150-300 kyr old fast spreading oceanic crust (East Pacific Rise, 8˚15'N-10˚5'N) from wide-angle seismic refraction profiles, *Geophys. J. Int.*, *152*(3), 766-794, doi:10.1046/j.1365-246X.2003.01885.x.

Canales, J. P., R. S. Detrick, S. M. Carbotte, G. M. Kent, J. B. Diebold, A. Harding, J. Babcock, M. R. Nedimovic, and E. Van Ark (2005), Upper crustal structure and axial topography at intermediate spreading ridges: Seismic constraints from the southern Juan de Fuca Ridge, *J. Geophys. Res.*, *110*(B12), 23537-23555, doi:10.1029/2005jb003630.

Canales, J. P., H. Carton, S. M. Carbotte, J. C. Mutter, M. R. Nedimovic, M. Xu, O. Aghaei, M. Marjanovic, and K. Newman (2012), Network of off-axis melt bodies at the East Pacific Rise, *Nature Geosci.*, *5*, 279-283, doi:10.1038/ngeo1377.

Carbotte, S. M., J. C. Mutter, and L. Q. Xu (1997), Contribution of volcanism and tectonism to axial and flank morphology of the southern East Pacific Rise, 17˚10' - 17˚40'S, from a study of layer 2A geometry, *J. Geophys. Res.*, *102*(B5), 10165-10184, doi:10.1029/96JB03910.

Carbotte, S. M., J. P. Canales, M. R. Nedimovic, H. Carton, and J. C. Mutter (2012), Recent Seismic Studies at the East Pacific Rise 8˚20' - 10˚10' N and Endeavour Segment: Insights into Mid-Ocean Ridge Hydrothermal and Magmatic Processes, *Oceanography*, *25*(1), 100-112, doi:10.5670/oceanog.2012.08.

Carbotte, S. M., M. R. Nedimovic, J. P. Canales, G. M. Kent, A. J. Harding, and M. Marjanovic (2008), Variable crustal structure along the Juan de Fuca Ridge: Influence of on-axis hot spots and absolute plate motions, *Geochem. Geophys. Geosyst.*, *9*, Q08001, doi:10.1029/2007GC001922.

Carbotte, S. M., R. S. Detrick, A. Harding, J. P. Canales, J. Babcock, G. Kent, E. Van Ark, M. Nedimovic, and J. Diebold (2006), Rift topography linked to magmatism at the intermediate spreading Juan de Fuca Ridge, *Geology*, *34*(3), 209-212, doi:10.1130/G21969.1.

Christensen, N. I. (1979), Compressional wave velocities in rocks at high temperatures and pressures, critical thermal gradients, and crustal low-velocity zones, *J. Geophys. Res.*, *84*, 6849-6857, doi:10.1029/JB084iB12p06849.

Christeson, G. L., P. R. Shaw, and J. D. Garmany (1997), Shear and compressional wave structure of the East Pacific Rise, 9˚-10˚ N, *J. Geophys. Res.*, *102*, 7821-7835, doi:10.1029/96JB03901.

Coumou, D., T. Driesner, and C. A. Heinrich (2008), The structure and dynamics of mid-ocean ridge hydrothermal systems, *Science*, *321*(5897), 1825-1828, doi:10.1126/Science.1159582.

Cowen, J. P., E. T. Baker, and R. W. Embley (2004), Detection of and response to mid-ocean ridge magmatic events: implications for the subsurface biosphere, in *The Subseafloor Biosphere at Mid-Ocean Ridges*, edited by W. S. D. Wilcock, E. F. DeLong, D. S. Kelley, J. A. Baross and S. C. Cary, AGU, Washington, DC.

Cowie, P. A., C. H. Scholz, M. Edwards, and A. Malinverno (1993), Fault strain and seismic coupling on mid-ocean ridges, *J. Geophys. Res.*, *98*(B10), 17911-17920, doi:10.1029/93JB01567.

Crampin, S. (1993), A review of the effects of crack geometry on wave propagation through aligned cracks, *Can. J. Explor. Geophys.*, *29*, 3-17.

Creager, K. C., and L. R. M. Dorman (1982), Location of instruments on the seafloor by joint adjustment of instrument and ship positions, *J. Geophys. Res.*, *87*(B10), 8379-8388, doi:10.1029/JB087iB10p08379.

Crone, T. J., W. S. D. Wilcock, and R. E. McDuff (2010), Flow rate perturbations in a black smoker hydrothermal vent in response to a mid-ocean ridge earthquake swarm, *Geochem. Geophys. Geosyst.*, *11*(3), Q03012, doi:03010.01029/02009gc002926.

Crone, T. J., M. Tolstoy, and D. F. Stroup (2011), Permeability structure of young ocean crust from poroelastically triggered earthquakes, *Geophys. Res. Lett.*, *38*, L05305, doi: 05310.01029/02011gl046820.

Cudrak, C. F., and R. M. Clowes (1993), Crustal structure of Endeavour Ridge Segment, Juan de Fuca Ridge, from a detailed seismic refraction survey, *J. Geophys. Res.*, *98*(B4), 6329-6349, doi:10.1029/92JB02860.

Cummings, W. C., and P. O. Thompson (1971), Underwater sounds from the Blue Whale, Balaenoptera musculus, *J. Acoust. Soc. Am.*, *50*(4), 1193-1198, doi:10.1121/1.1912752.

Davis, E. E., and C. R. B. Lister (1977), Heat flow measured over the Juan de Fuca Ridge: Evidence for widespread hydrothermal circulation in a highly heat transportive crust, *J. Geophys. Res.*, *82*, 4845-4860, doi:10.1029/JB082i030p04845.

Davis, E. E., and J. L. Karsten (1986), On the cause of asymmetric distribution of seamounts about the Juan de Fuca ridge: Ridge crest migration over a heterogeneous asthenosphere, *Earth Planet. Sci. Lett.*, *79*, 385-396, doi:10.1016/0012-821X(86)90194-9.

Davis, E. E., and H. Villinger (1992), Tectonic and Thermal Structure of the Middle Valley Sedimented Rift, Northern Juan de Fuca Ridge, *Proceedings of the Ocean Drilling Program, Initial Report*, *139*, 9-41.

Davis, E. E., K. Wang, K. Becker, and R. E. Thomson (2000), Formation-scale hydraulic and mechanical properties of oceanic crust inferred from pore pressure response to periodic seafloor loading, *J. Geophys. Res.*, *105*(B6), 13423-13435, doi:10.1029/2000JB900084.

Davis, E. E., K. Wang, R. E. Thomson, K. Becker, and J. F. Cassidy (2001), An episode of seafloor spreading and associated plate deformation inferred from crustal fluid pressure transients, *J. Geophys. Res.*, *106*(B10), 21953-21963, doi:10.1029/2000JB000040.

Davis, E. E., K. Becker, R. Dziak, J. Cassidy, K. Wang, and M. Lilley (2004), Hydrological response to a seafloor spreading episode on the Juan de Fuca Ridge, *Nature*, *430*, 335-338, doi:10.1038/nature02755.

Delaney, J. R., V. Robigou, R. E. McDuff, and M. K. Tivey (1992), Geology of a vigorous hydrothermal system on the Endeavour segment, Juan de Fuca Ridge, *J. Geophys. Res.*, *97*(B13), 19663-19682, doi:10.1029/92JB00174.

Delaney, J. R., D. S. Kelley, M. D. Lilley, D. A. Butterfield, J. A. Baross, W. S. D. Wilcock, R. W. Embley, and M. Summit (1998), The quantum event of oceanic crustal accretion: Impacts of diking at mid-ocean ridges, *Science*, *281*(5374), 222-230, doi:10.1126/science.281.5374.222.

deMartin, B. J., R. A. Sohn, J. P. Canales, and S. E. Humphris (2007), Kinematics and geometry of active detachment faulting beneath the Trans-Atlantic Geotraverse (TAG) hydrothermal field on the Mid-Atlantic Ridge, *Geology*, *35*(8), 711-714.

DeMets, C., R. G. Gordon, D. F. Argus, and S. Stein (1994), Effect of recent revisions to the geomagnetic reversal time-scale on estimates of current plate motions, *Geophys. Res. Lett.*, *21*(20), 2191-2194.

Detrick, R. S., R. S. White, and G. M. Purdy (1993a), Crustal Structure of North-Atlantic Fracture-Zones, *Rev. Geophys.*, *31*(4), 439-458, doi:10.1029/93rg01952.

Detrick, R. S., J. C. Mutter, P. Buhl, and I. I. Kim (1990), No evidence from multichannel reflection data for a crustal magma chamber in the MARK area on the Mid-Atlantic Ridge, *Nature*, *347*, 61-64.

Detrick, R. S., A. J. Harding, G. M. Kent, J. A. Orcutt, J. C. Mutter, and P. Buhl (1993b), Seismic Structure of the Southern East Pacific Rise, *Science*, *259*(5094), 499-503, doi:10.1126/Science.259.5094.499.

Detrick, R. S., P. Buhl, E. Vera, J. Mutter, J. Orcutt, J. Madsen, and T. Brocher (1987), Multichannel seismic imaging of a crustal magma chamber along the East Pacific Rise, *Nature*, *326*(6108), 35-41, doi:10.1038/326035a0.

Detrick, R. S., S. Carbotte, E. V. Ark, J. P. Canales, G. Kent, A. Harding, J. Diebold, and M. Nedimovic (2002), New multichannel seismic constraints on the crustal structure of the Endeavour segment, Juan de Fuca Ridge: Evidence for a crustal magma chamber, *Eos Trans. AGU*, *83*(47), Fall Meet. Suppl., Abstract T12B-1316.

Dunn, R. A., and D. R. Toomey (2001), Crack-induced seismic anisotropy in the oceanic crust across the East Pacific Rise (9˚ 30'N), *Earth Planet. Sci. Lett.*, *189*(1-2), 9-17, doi:10.1016/S0012-821X(01)00353-3.

Dunn, R. A., D. R. Toomey, and S. C. Solomon (2000), Three-dimensional seismic structure and physical properties of the crust and shallow mantle beneath the East Pacific Rise at 9˚30'N, *J. Geophys. Res.*, *105*(B10), 23537-23555, doi:10.1029/2000JB900210.

Dunn, R. A., V. Lekic, R. S. Detrick, and D. R. Toomey (2005), Three-dimensional seismic structure of the Mid-Atlantic Ridge (35˚N): Evidence for focused melt supply and lower crustal dike injection, *J. Geophys. Res.*, *110*(B9), doi:10.1029/2004JB003473.

Durant, D. T., and D. R. Toomey (2009), Evidence and implications of crustal magmatism on the flanks of the East Pacific Rise, *Earth Planet. Sci. Lett.*, *287*(1-2), 130-136, doi:10.1016/j.epsl.2009.08.003.

Dziak, R. P. (2006), Explorer deformation zone: Evidence of a large shear zone and reorganization of the Pacific-Juan de Fuca-North American triple junction, *Geology*, *34*(3), doi:10.1130/g22164.22161.

Dziak, R. P., and C. G. Fox (1999a), The January 1998 earthquake swarm at Axial Volcano, Juan de Fuca Ridge: Hydroacousitc evidence for seafloor volcanic activity, *Geophys. Res. Lett.*, *26*(23), 3429-3432.

Dziak, R. P., and C. G. Fox (1999b), Long-term seismicity and ground deformation at Axial Volcano, Juan de Fuca Ridge, *Geophys. Res. Lett.*, *26*(24), 3641-3644.

Dziak, R. P., C. G. Fox, and A. E. Schreiner (1995), The June-July 1993 seismo-acoustic event at CoAxial segment, Juan de Fuca Ridge: Evidence for a lateral dike injection, *Geophys. Res. Lett.*, *22*(2), 135-138.

Dziak, R. P., S. R. Hammond, and C. G. Fox (2011), A 20-year hydroacoustic time series of seismic and volcanic events in the Northeast Pacific Ocean, *Oceanography*, *24*(3), 280-293, doi:10.5670/oceanog.2011.79.

Dziak, R. P., D. R. Bohnenstiehl, J. P. Cowen, E. T. Baker, K. H. Rubin, J. H. Haxel, and M. J. Fowler (2007), Rapid dike emplacement leads to eruptions and hydrothermal plume release during seafloor spreading events, *Geology*, *35*(7), doi:10.1130/G23476a.23471.

Dziak, R. P., D. K. Smith, D. R. Bohnenstiehl, C. G. Fox, D. Desbruyeres, H. Matsumoto, M. Tolstoy, and D. J. Fornari (2004), Evidence of a recent magma dike intrusion at the slow spreading Lucky Strike segment, Mid-Atlantic Ridge, *J. Geophys. Res.*, *109*(B12), B12102, doi:12110.11029/12004jb003141.

Ebinger, C., A. Ayele, D. Keir, J. Rowland, G. Yirgu, T. Wright, M. Belachew, and I. Hamling (2010), Length and Timescales of Rift Faulting and Magma Intrusion: The Afar Rifting Cycle from 2005 to Present, *Ann. Rev. Earth Planet. Sci.*, *38*, 10.1146/annurev-earth-040809-152333.

Fisher, A. T. (1998), Permeability within basaltic oceanic crust, *Rev. Geophys.*, *36*(2), 143-182.

Fox, C. G., and D. P. Dziak (1998), Hydroacoustic Detection of Volcanic Activity on the Gorda Ridge, February-March 1996, *Deep-Sea Res. Part II*, *45*(12), 2513-2530.

Freed, A. M. (2005), Earthquake triggering by static, dynamic, and postseismic stress transfer, *Ann. Rev. Earth Planet. Sci.*, *33*, doi:10.1146/annurev.earth.1133.092203.122505.

Freed, A. M., and J. Lin (1998), Time-dependent changes in failure stress following thrust earthquakes, *J. Geophys. Res.*, *103*(B10), 24393-24409.

Freed, A. M., and J. Lin (2001), Delayed triggering of the 1999 Hector Mine earthquake by viscoelastic stress transfer, *Nature*, *411*, 180-183.

Glickson, D. A., D. S. Kelley, and J. R. Delaney (2007), Geology and hydrothermal evolution of the Mothra hydrothermal field, Endeavour Segment, Juan de Fuca Ridge, *Geochem. Geophys. Geosyst.*, *8*(6), Q06010, doi:06010.01029/02007GC001588.

Gomberg, J., P. A. Reasenberg, P. Bodin, and R. A. Harris (2001), Earthquake triggering by seismic waves following the Landers and Hector Mine earthquakes, *Nature*, *411*(6836), 462-466.

Grandin, R., A. Socquet, C. Doubre, E. Jacques, and G. C.P. King (2012), Elastic thickness control of lateral dyke intrusion at mid-ocean ridges, *Earth Planet. Sci. Lett.*, *319-320*(2012), doi:10.1016/j.epsl.2011.1012.1011.

Grevemeyer, I., W. Weigel, and C. Jennrich (1998), Structure and ageing of oceanic crust at 14˚S on the East Pacific Rise, *Geophys. J. Int.*, *135*(2), 573-584, doi:10.1046/j.1365-246X.1998.00673.x.

Hanks, T. C., and M. Wyss (1972), The use of body-wave spectra in the determination of seismic-source parameters, *Bull. Seismol. Soc. Am.*, *62*(2), 561-589.

Hanks, T. C., and H. Kanamori (1979), Moment magnitude scale, *J. Geophys. Res.*, *84*(B5), 2348-2350.

Hardebeck, J. L., J. J. Nazareth, and E. Hauksson (1998), The static stress change triggering model: Constraints from two southern California aftershock sequences, *J. Geophys. Res.*, *103*(B10), 24427-24437.

Harding, A. J., G. M. Kent, and J. A. Orcutt (1993), A Multichannel Seismic Investigation of Upper Crustal Structure at 9˚N on the East Pacific Rise - Implications for Crustal Accretion, *J. Geophys. Res.*, *98*(B8), 13925-13944, doi:10.1029/93jb00886.

Harris, R. A., and R. W. Simpson (1992), Changes in static stress on Southern California faults after the 1992 Landers earthquake, *Nature*, *360*(6401), 251-254.

Haymon, R. M., D. J. Fornari, M. H. Edwards, S. M. Carbotte, D. Wright, and K. C. Macdonald (1991), Hydrothermal vent distribution along the East Pacific Rise crest (9°09'-54'N) and its relationship to magmatic and tectonic processes on fast-spreading mid-ocean ridges, *Earth Planet. Sci. Lett.*, *102*, 513-534.

Haymon, R. M., et al. (1993), Volcanic eruption of the mid-ocean ridge along the East Pacific Rise crest at 9°45-52'N: Direct submersible observations of seafloor phenomena associated with an eruption event in April, 1991, *Earth Planet. Sci. Lett.*, *119*, 85-101.

Hey, R. N., and D. S. Wilson (1982), Propagating Rift Explanation for the Tectonic Evolution of the Northeast Pacific - the Pseudo-Movie, *Earth Planet. Sci. Lett.*, *58*(2), 167-188, doi:10.1016/0012-821x(82)90192-3.

Hill, D. P., et al. (1993), Seismicity remotely triggered by the magnitude 7.3 Landers, California, earthquake, *Science*, *260*(5114), 1617-1623.

Hirth, G., and D. L. Kohlstedt (1996), Water in the oceanic upper mantle: implications for rheology, melt extraction and the evolution of the lithosphere, *Earth Planet. Sci. Lett.*, *144*, 93-108.

Hirth, G., J. Escartin, and J. Lin (1998), The rheology of the lower oceanic crust; implications for lithospheric deformation at mid-ocean ridges, *Geophysical Monograph*, *106*, 291-303.

Hooft, E. E. E., H. Schouten, and R. S. Detrick (1996), Constraining crustal emplacement processes from the variation in seismic layer 2A thickness at the East Pacific Rise, *Earth Planet. Sci. Lett.*, *142*(3-4), 289-309, doi:10.1016/0012-821x(96)00101-x.

Hooft, E. E. E., R. S. Detrick, D. R. Toomey, J. A. Collins, and J. Lin (2000), Crustal thickness and structure along three contrasting spreading segments of the Mid-Atlantic Ridge, 33.5˚-35˚N, *J. Geophys. Res.*, *105*(B4), 8205-8226, doi:10.1029/1999JB900442.

Hooft, E. E. E., et al. (2010), A seismic swarm and regional hydrothermal and hydrologic perturbations: The northern Endeavour segment, February 2005, *Geochem. Geophys. Geosyst.*, *11*(12), Q12015, doi:12010.11029/12010GC003264.

Huang, P. Y., S. C. Solomon, E. A. Bergman, and J. L. Nabelek (1986), Focal depths and mechanisms of Mid-Atlantic Ridge earthquakes from body wave-form inversion, *J. Geophys. Res.*, *91*(B1), 579-598.

Hudson, J. A. (1981), Wave speeds and attenuation of elastic waves in material containing cracks, *Geophys. J. R. Astr. Soc.*, *64*, 133-150, doi:10.1111/j.1365-246X.1981.tb02662.x.

Hussenoeder, S. A., J. A. Collins, G. M. Kent, R. S. Detrick, A. J. Harding, J. A. Orcutt, J. C. Mutter, and P. Buhl (1996), Seismic analysis of the axial magma chamber reflector along the southern East Pacific Rise from conventional reflection profiling, *J. Geophys. Res.*, *101*(B10), 22087-22105, doi:10.1029/96JB01907.

Hyndman, R. D., R. P. Riddihough, and R. Herzer (1979), The Nootka fault zone - a new plate boundary off western Canada, *Geophys. J. Roy. Astron. Soc.*, *58*, 667-683.

Jacobson, R. S. (1992), Impact of crustal evolution on changes of the seismic properties of the uppermost ocean crust, *Rev. Geophys.*, *30*, 23-42, doi:10.1029/91RG02811.

Johnson, H. P., J. L. Karsten, J. R. Delaney, E. E. Davis, R. G. Currie, and R. L. Chase (1983), A detailed study of the Cobb Offset on the Juan de Fuca Ridge: Evolution of the propagating rift, *J. Geophys. Res.*, *88*, 2297-2315, doi:10.1029/JB088iB03p02297.

Johnson, H. P., M. Hutnak, R. P. Dziak, C. G. Fox, I. Urcuyo, J. P. Cowen, J. Nabalek, and C. Fisher (2000), Earthquake-induced changes in a hydrothermal system on the Juan de Fuca Ridge mid-ocean ridge, *Nature*, *407*, 174-177, doi:10.1038/35025040.

Kappel, E. S., and W. B. F. Ryan (1986), Volcanic episodicity and a non-steady state rift valley along Northeast Pacific spreading centers: Evidence from Sea MARC I, *J. Geophys. Res.*, *91*, 13925-13940, doi:10.1029/JB091iB14p13925.

Kappus, M. E., A. J. Harding, and J. A. Orcutt (1995), A baseline for upper crustal velocity variations along the East Pacific Rise at 13˚N, *J. Geophys. Res.*, *100*, 6143-6161, doi:10.1029/94JB02474.

Karson, J. A., et al. (1987), Along-axis variations in seafloor spreading in the MARK area, *Nature*, *328*, 681-685.

Karsten, J. L., and J. R. Delaney (1989), Hot spot-ridge crest convergence in the Northeast Pacific, *J. Geophys. Res.*, *94*(B1), 700-712, doi:10.1029/JB094iB01p00700.
Karsten, J. L., S. R. Hammond, E. E. Davis, and R. G. Currie (1986), Detailed geomorphology and neotectonics of the Endeavour Segment, Juan de Fuca Ridge - New results from Seabeam swath mapping, *Geol. Soc. Am. Bull.*, *97*(2), 213-221.
Karsten, J. L., J. R. Delaney, J. M. Rhodes, and R. A. Liias (1990), Spatial and temporal evolution of magmatic systems beneath the Endeavour segment, Juan de Fuca Ridge: Tectonic and petrologic constraints, *J. Geophys. Res.*, *95*(B12), 19,235-219,256.
Kelley, D. S., J. R. Delaney, and D. R. Yoerger (2001), Geology and venting characteristics of the Mothra hydrothermal field, Endeavour Segment, Juan de Fuca Ridge, *Geology*, *29*(10), 959-962.
Kelley, D. S., J. A. Baross, and J. R. Delaney (2002), Volcanoes, fluids, and life at mid-ocean ridge spreading centers, *Ann. Rev. Earth Planet. Sci.*, *30*, 385-491, doi:10.1146/annurev.earth.30.091201.141331.
Kelley, D. S., et al. (2012), Endeavour Segment of the Juan de Fuca Ridge: One of the most remarkable places on Earth, *Oceanography*, *25*(1), 44-61, doi:10.5670/oceanog.2012.03.
Kellogg, J. P. (2011), Temporal and spatial variability of hydrothermal fluxes within a mid-ocean ridge segment, *PhD thesis*, University of Washington, Seattle.
Kent, G. M., A. J. Harding, and J. A. Orcutt (1990), Evidence for a Smaller Magma Chamber beneath the East Pacific Rise at 9-Degrees-30' N, *Nature*, *344*(6267), 650-653, doi:10.1038/344650a0.
Kent, G. M., A. J. Harding, and J. A. Orcutt (1993), Distribution of Magma beneath the East Pacific Rise between the Clipperton Transform and the 9˚17' N Deval from Forward Modeling of Common Depth Point Data, *J. Geophys. Res.*, *98*(B8), 13945-13969, doi:10.1029/93jb00705.
Kent, G. M., A. J. Harding, J. A. Orcutt, R. S. Detrick, J. C. Mutter, and P. Buhl (1994), Uniform accretion of oceanic crust south of the Garrett transform at 14˚15' S on the East Pacific Rise, *J. Geophys. Res.*, *99*, 9097-9116, doi:10.1029/93JB02872.
Kent, G. M., et al. (2000), Evidence from three-dimensional seismic reflectivity images for enhanced melt supply beneath mid-ocean-ridge discontinuities, *Nature*, *406*(6796), 614-618.
Kern, H., and J. M. Tubia (1993), Pressure and Temperature-Dependence of P-Wave and S-Wave Velocities, Seismic Anisotropy and Density of Sheared Rocks from the Sierra Alpujata Massif (Ronda Peridotites, Southern Spain), *Earth Planet. Sci. Lett.*, *119*(1-2), 191-205, doi:10.1016/0012-821x(93)90016-3.
Kilb, D., J. Gomberg, and P. Bodin (2000), Triggering of earthquake aftershocks by dynamic stresses, *Nature*, *408*(6812), 570-574.
King, G. C. P., R. S. Stein, and J. Lin (1994), Static stress changes and the triggering of earthquakes, *Bull. Seismol. Soc. Am.*, *84*(3), 935-953.
Klein, F. W. (2002), User's guide to HYPOINVERSE-2000, a Fortran program to solve for earthquake locations and magnitudes, *U. S. Geol. Surv. Open File Rep. Rep. 02-171*, 123 pp..
Kreemer, C., R. Govers, K. P. Furlong, and W. E. Holt (1998), Plate boundary deformation between the Pacific and North America in the Explorer region, *Tectonophysics*, *293*, 225-238.

Kushiro, I. (2001), Partial melting experiments on peridotite and origin of mid-ocean ridge basalt, *Ann. Rev. Earth Planet. Sci.*, *29*, 71-107, doi:Doi 10.1146/Annurev.Earth.29.1.71.
Lilley, M. D., D. A. Butterfield, J. E. Lupton, and E. J. Olson (2003), Magmatic events can produce rapid changes in hydrothermal vent chemistry, *Nature*, *422*, 878-881, doi:10.1038/nature01569.
Lilley, M. D., D. A. Butterfield, E. J. Olson, J. E. Lupton, S. A. Macko, and R. E. McDuff (1993), Anomalous CH4 and NH4+ concentrations at an unsedimented mid-ocean-ridge hydrothermal system, *Nature*, *364*(6432), 45-47.
Lowell, R. P., and L. N. Germanovich (1994), On the temporal evolution of high-temperature hydrothermal systems at ocean ridge crests, *J. Geophys. Res.*, *99*(B1), 565-575.
Lowell, R. P., P. Van Cappellen, and L. N. Germanovich (1993), Silica precipitation in fractures and the evolution of permeability in hydrothermal upflow zones, *Science*, *260*, 192-194, doi:10.1126/science.260.5105.192.
Lowell, R. P., Y. Yao, and L. N. Germanovich (2003), Anhydrite precipitation and the relationship between focused and diffuse flow in seafloor hydrothermal systems, *J. Geophys. Res.*, *108*(B9), doi:10.1029/2002jb002371.
Macdonald, K. C. (1998), Linkages between faulting, volcanism, hydrothermal activity and segmentation on fast spreading centers, in *Faulting and magmatism at mid-ocean ridges*, edited by W. R. Buck, P. T. Delaney, J. A. Karson and Y. Lagabrielle, American Geophysical Union, Washington, D.C..
Macdonald, K. C. (2001), *Mid-Ocean Ridge Tectonics, Volcanism and Geomorphology*, Academic Press, San Diego.
Macdonald, K. C., D. S. Scheirer, and S. M. Carbotte (1991), Mid-ocean ridges: Discontinuities, segments and giant cracks, *Science*, *253*, 986-994, doi:10.1126/science.253.5023.986.
Macdonald, K. C., J. C. Sempere, P. J. Fox, and R. Tyce (1987), Tectonic Evolution of Ridge-Axis Discontinuities by the Meeting, Linking, or Self-Decapitation of Neighboring Ridge Segments, *Geology*, *15*(11), 993-997, doi:10.1130/0091-7613(1987)15.
Magde, L. S., A. H. Barclay, D. R. Toomey, R. S. Detrick, and J. A. Collins (2000), Crustal magma plumbing within a segment of the Mid-Atlantic Ridge, 35˚N, *Earth Planet. Sci. Lett.*, *175*, 55-67, doi:10.1016/S0012-821X(99)00281-2.
McClain, J. S., M. L. Begnaud, M. A. Wright, J. Fondrk, and G. K. Von Damm (1993), Seismicity and tremor in a submarine hydrothermal field: The northern Juan de Fuca Ridge, *Geophys. Res. Lett.*, *20*(17), 1883-1886, doi:10.1029/93GL01872.
Moser, T. J. (1991), Shortest path calculation of seismic rays, *Geophysics*, *56*, 59-67, doi:10.1190/1.1442958.
Mutter, J. C. (1992), Seismic imaging of sea-floor spreading, *Science*, *258*, 1442-1443.
Mutter, J. C., S. M. Carbotte, W. S. Su, L. Q. Xu, P. Buhl, R. S. Detrick, G. M. Kent, J. A. Orcutt, and A. J. Harding (1995), Seismic Images of Active Magma Systems beneath the East Pacific Rise between 17-Degrees-05' and 17-Degrees-35's, *Science*, *268*(5209), 391-395, doi:Doi 10.1126/Science.268.5209.391.
Nedimovic, M. R., S. M. Carbotte, J. B. Diebold, A. J. Harding, J. P. Canales, and G. M. Kent (2008), Upper crustal evolution across the Juan de Fuca ridge flanks, *Geochem. Geophys. Geosyst.*, *9*, Q09006, doi:10.1029/2008gc002085.
Newman, K. R., M. R. Nedimovic, J. P. Canales, and S. M. Carbotte (2011), Evolution of seismic layer 2B across the Juan de Fuca Ridge from hydrophone streamer 2-D

traveltime tomography, *Geochem. Geophys. Geosyst.*, *12*, Q05009, doi:10.1029/2010gc003462.
Nostro, C., M. Cocco, and M. E. Belardinelli (1997), Static stress changes in extensional regimes: An application to southern Apennines (Italy), *Bull. Seismol. Soc. Am.*, *87*(1), 234-248.
Nostro, C., A. Piersanti, and M. Cocco (2001), Normal fault interaction caused by coseismic and postseismic stress changes, *J. Geophys. Res.*, *106*(B9), 19391-19410.
Parmentier, E. M., and J. Phipps Morgan (1990), Spreading rate dependence of three-dimensional structure in oceanic spreading centers, *Nature*, *348*, 325-328.
Phipps Morgan, J., and Y. J. Chen (1993a), Dependence of ridge-axis morphology on magma supply and spreading rate, *Nature*, *364*, 706-708.
Phipps Morgan, J., and Y. J. Chen (1993b), The genesis of oceanic crust: Magma injection, hydrothermal circulation, and crustal flow, *J. Geophys. Res.*, *98*, 6283-6297.
Pollard, D. D., and A. Aydin (1984), Propagation and linkage of oceanic ridge segments, *J. Geophys. Res.*, *89*(B12), 17-28, doi:10.1029/JB089iB12p10017.
Prejean, S. G., D. P. Hill, E. E. Brodsky, S. E. Hough, M. J. S. Johnston, S. D. Malone, D. H. Oppenheimer, A. M. Pitt, and K. B. Richards-Dinger (2004), Remotely triggered seismicity from the United States west coast following the M_w 7.9 Denali Fault Earthquake, *Bull. Seismol. Soc. Am.*, *94*(6), 348-359.
Purdy, G. M., L. S. L. Kong, G. L. Christeson, and S. C. Solomon (1992), Relationship between spreading rate and the seismic structure of mid-ocean ridges, *Nature*, *355*(6363), 815-817, doi:10.1038/355815a0.
Qin, R., and W. R. Buck (2008), Why meter-wide dikes at oceanic spreading centers?, *Earth Planet. Sci. Lett.*, *265*(3-4), doi:10.1016/j.epsl.2007.1010.1044.
Robigou, V., J. R. Delaney, and D. S. Stakes (1993), Large massive sulfide deposits in a newly discovered active hydrothermal system, the High-Rise field, Endeavour segment, Juan de Fuca Ridge, *Geophys. Res. Lett.*, *20*(17), 1887-1890.
Rohr, K. M. M. (1994), Increase of seismic velocities in upper oceanic crust and hydrothermal circulation on the Juan de Fuca plate, *Geophys. Res. Lett.*, *21*, 2163-2166, doi:10.1029/94GL01913.
Romanowicz, B., D. Stakes, D. Dolenc, D. Neuhauser, P. McGill, R. Uhrhammer, and T. Ramirez (2006), The Monterey Bay broadband ocean bottom seismic observatory, *Ann. Geophys.*, *49*(2-3), 607-623.
Rubin, K. H. (2006), Geochronology and composition of the 2005-06 volcanic eruptions of the East Pacific Rise, 9 degrees 46'-56'N, *Eos Trans. AGU*, *87*(Suppl.), Abstract V23B-0602.
Rubin, K. H., J. D. Macdougall, and M. R. Perfit (1994), ^{210}Po-^{210}Pb dating of recent volcanic-eruptions on the sea-floor, *Nature*, *368*(6474), 841-844, doi:10.1038/368841a0.
Seewald, J., A. Cruse, and P. Saccocia (2003), Aqueous volatiles in hydrothermal fluids from the Main Endeavour Field, northern Juan de Fuca Ridge: temporal variability followig earthquake activity *Earth Planet. Sci. Lett.*, *216*(4), doi:10.1016/s0012-1821x(1003)00543-00540.
Seher, T., S. C. Singh, W. C. Crawford, and J. Escartin (2010a), Upper crustal velocity structure beneath the central Lucky Strike Segment from seismic refraction measurements, *Geochem. Geophys. Geosyst.*, *11*, Q05001, doi:10.1029/2009gc002894.
Seher, T., W. C. Crawford, S. C. Singh, M. Cannat, V. Combier, and D. Dusunur (2010b), Crustal velocity structure of the Lucky Strike segment of the Mid-Atlantic Ridge at 37

degrees N from seismic refraction measurements, *J. Geophys. Res.*, *115*, B03103, doi:10.1029/2009jb006650.
Seyfried, W. E., Jr., J. S. Seewald, M. E. Berndt, K. Ding, and D. I. Foustoukos (2003), Chemistry of hydrothermal vent fluids from the Main Endeavour Field, northern Juan de Fuca Ridge: Geochemical controls in the aftermath of the June 1999 seismic events, *J. Geophys. Res.*, *108*(B9), 2429, doi:2410.1029/2002JB001957.
Shaw, P. R., and J. A. Orcutt (1985), Waveform inversion of seismic refraction data and applications to young Pacific crust, *Geophys. J. R. Astr. Soc.*, *82*, 375-414, doi:10.1111/j.1365-246X.1985.tb05143.x.
Shearer, P. M., and J. A. Orcutt (1986), Compressional and shear wave anistropy in the oceanic lithosphere- the Ngendei seismic refraction experiment, *Geophys. J. R. Astron. Soc.*, *87*, 967-1003, doi:10.1111/j.1365-246X.1986.tb01979.x.
Shi, Y., and B. A. Bolt (1982), The Standard Error of the Magnitude-Frequency B-Value, *Bull. Seismol. Soc. Am.*, *72*(5), 1677-1687.
Shoberg, T., S. Stein, and J. Karsten (1991), Constraints on rift propagation history at the Cobb Offset, Juan de Fuca Ridge, from numerical modeling of tectonic fabric, *Tectonophys.*, *197*, 295-308, doi:10.1016/0040-1951(91)90047-V.
Sigmundsson, F. (2006), *Iceland geodynamics; crustal deformation and divergent plate tectonics*, Praxis Publishing: Chichester, United Kingdom.
Singh, S. C., G. M. Kent, J. S. Collier, A. J. Harding, and J. A. Orcutt (1998), Melt to mush variations in crustal magma properties along the ridge crest at the southern East Pacific Rise, *Nature*, *394*(6696), 874-878, doi:10.1038/29740.
Sinton, J. M., and R. S. Detrick (1992), Mid-ocean ridge magma chambers, *J. Geophys. Res.*, *97*(B1), 197-216, doi:10.1029/91JB02508.
Smith, D. K., and J. R. Cann (1992), The role of seamount volcanism in crustal construction at the Mid-Atlantic Ridge (24˚- 30˚N), *J. Geophys. Res.*, *97*(B2), 1645-1658, doi:10.1029/91JB02507.
Smith, D. K., and J. R. Cann (1993), Building the crust at the Mid-Atlantic Ridge, *Nature*, *365*, 707-715, doi:10.1038/365707a0.
Sohn, R. A., J. A. Hildebrand, and S. C. Webb (1998a), Postrifting seismicity and a model for the 1993 diking event on the CoAxial segment, Juan de Fuca Ridge, *J. Geophys. Res.*, *103*(B5), 9867-9877, doi:10.1029/98JB00391.
Sohn, R. A., W. C. Crawford, and S. C. Webb (1999a), Local seismicity following the 1998 eruption of Axial Volcano, *Geophys. Res. Lett.*, *26*(23), 3433-3436, doi:10.1029/1999GL900505.
Sohn, R. A., J. A. Hildebrand, and S. C. Webb (1999b), A microearthquake survey of the high-temperature vent fields on the volcanically active East Pacific Rise, *J. Geophys. Res.*, *104*, 25367-25377, doi:10.1029/1999JB900263.
Sohn, R. A., A. H. Barclay, and S. C. Webb (2004), Microearthquake patterns following the 1998 eruption of Axial Volcano, Juan de Fuca Ridge: Mechanical relaxation and thermal strain, *J. Geophys. Res.*, *109*(B1), B01101, doi:01110.01029/02003jb002499.
Sohn, R. A., S. C. Webb, J. A. Hildebrand, and B. D. Cornuelle (1997), Three-dimensional tomographic velocity structure of upper crust, CoAxial segment, Juan de Fuca Ridge: Implications for on-axis evolution and hydrothermal circulation, *J. Geophys. Res.*, *102*, 17679-17695, doi:10.1029/97JB00592.

Sohn, R. A., D. J. Fornari, K. L. Von Damm, J. A. Hildebrand, and S. C. Webb (1998b), Seismic and hydrothermal evidence for a cracking event on the East Pacific rise crest at 9º50'N, *Nature*, *396*, 159-161, doi:10.1038/24146.

Soule, S. A., D. J. Fornari, M. R. Perfit, and K. H. Rubin (2007), New insights into mid-ocean ridge volcanic processes from the 2005-2006 eruption of the East Pacific Rise, 9˚46'N-9˚56'N, *Geology*, *35*(12), doi:10.1130/G23924A.23921, doi:1079-1082.

Spera, F. J. (2000), *Physical properties of magmas*, 171-190 pp., Academic Press : San Diego, CA, United States, United States.

Stakes, D. S., J. McClain, T. VanZandt, P. McGill, and M. Begnaud (1998), Corehole seismometer development for low-noise seismic data in a long-term seafloor observatory, *Geophys. Res. Lett.*, *25*(14), 2745-2748.

Stakes, D. S., M. R. Perfit, M. A. Tivey, D. W. Caress, T. M. Ramirez, and N. Maher (2006), The Cleft revealed: Geologic, magnetic, and morphologic evidence for construction of upper oceanic crust along the southern Juan de Fuca Ridge, *Geochem. Geophys. Geosyst.*, *7*, Q04003, doi:10.1029/2005gc001038.

Stakes, D. S., B. Romanowicz, M. L. Begnaud, K. C. McNally, J. P. Montagner, E. Stutzmann, and M. Pasyanos (2002), The MBARI margin seismology experiment: A Propotype seafloor observatory, in *Science-technology synergy for research in the marine environment: Challanges for the XXI century*, edited by L. Bernazoli, P. Favali and G. Smriglio, pp. 93-110, Elsevier, Amsterdam, The Netherlands.

Stein, R. S., A. A. Barka, and J. H. Dieterich (1997), Progressive failure on the North Anatolian fault since 1939 by earthquake stress triggering, *Geophys. J. Int.*, *128*(3), 594-604.

Stephen, R. A. (1985), Seismic anisotropy in the upper oceanic crust, *J. Geophys. Res.*, *90*, 11383-11396, doi:10.1029/JB090iB13p11383.

Stroup, D. F., M. Tolstoy, T. J. Crone, A. Malinverno, D. R. Bohnenstiehl, and F. Waldhauser (2009), Systematic along-axis tidal triggering of microearthquakes observed at 9 degrees 50'N East Pacific Rise, *Geophys. Res. Lett.*, *36*, L18302, doi:18310.11029/12009gl039493.

Takanami, T., and G. Kitagawa (1988), A new efficient procedure for the estimation of onset times of seismic-waves, *J. Phys. Earth*, *36*(6), 267-290, doi:10.4294/jpe1952.36.267.

Thurber, C. H. (1983), Earthquake locations and three-dimensional crustal structure in the Coyote Lake Area, Central California, *J. Geophys. Res.*, *88*, 8226-8236, doi:10.1029/JB088iB10p08226.

Tolstoy, M. (2008), Seismological constraints on magmatic and hydrothermal proceses at mid-ocean ridges, in *Modeling hydrothermal processes at oceanic spreading centers*, edited by R. P. Lowell, J. S. Seewald, A. Metaxas and M. R. Perfit, American Geophys. Union, Washington, DC.

Tolstoy, M., F. Waldhauser, D. R. Bohnenstiehl, R. T. Weekly, and W. Y. Kim (2008), Seismic identification of along-axis hydrothermal flow on the East Pacific Rise, *Nature*, *451*(7175), doi:10.1038/Nature06424, doi:10.1038/nature06424.

Tolstoy, M., et al. (2006), A sea-floor spreading event captured by seismometers, *Science*, *314*(5807), doi:10.1126/Science.1133950.

Tong, C. H., R. S. White, M. R. Warner, and A. W. Grp (2004), Effects of tectonism and magmatism on crack structure in oceanic crust: A seismic anisotropy study, *Geology*, *32*(1), 25-28, doi:10.1130/G19962.1.

Toomey, D. R., and G. R. Foulger (1989), Tomographic inversion of local earthquake data from the Hengill-Grensdalur Central Volcano Complex, Iceland, *J. Geophys. Res.*, *94*, 17497-17510, doi:10.1029/JB094iB12p17497.

Toomey, D. R., S. C. Solomon, and G. M. Purdy (1988), Microearthquakes beneath median valley of the Mid-Atlantic Ridge near 23ºN: Tomography and tectonics, *J. Geophys. Res.*, *93*(B8), 9093-9112.

Toomey, D. R., S. C. Solomon, and G. M. Purdy (1994), Tomographic imaging of the shallow crustal structure of the East Pacific Rise at 9˚30'N, *J. Geophys. Res.*, *99*(B12), 24135-24157, doi:10.1029/94JB01942.

Toomey, D. R., S. C. Solomon, G. M. Purdy, and M. H. Murray (1985), Microearthquakes beneath the median valley of the Mid-Atlantic Ridge near 23˚N: Hypocenters and focal mechanisms, *J. Geophys. Res.*, *90*(B7), 5443-5458.

Toomey, D. R., G. M. Purdy, S. C. Solomon, and W. S. D. Wilcock (1990), The three-dimensional seismic velocity structure of the East Pacific Rise near latitude 9˚30' N, *Nature*, *347*(6294), 639-645, doi:10.1038/347639a0.

Toomey, D. R., D. Jousselin, R. A. Dunn, W. S. D. Wilcock, and R. S. Detrick (2007), Skew of mantle upwelling beneath the East Pacific Rise governs segmentation, *Nature*, *446*(7134), 409-414, doi:10.1038/nature05679.

Tréhu, A. M., and S. C. Solomon (1983), Earthquakes in the Orozco transform zone: Seismicity, source mechanisms, and tectonics,, *J. Geophys. Res.*, *88*, 8203-8225.

Turcotte, D. L., and G. Schubert (2002), *Geodynamics: Applications of continuum mechanics to geological problems*, 2nd Edition ed., 456 pp., Cambridge University Press, New York, NY.

Van Ark, E. M., R. S. Detrick, J. P. Canales, S. M. Carbotte, A. J. Harding, G. M. Kent, M. R. Nedimovic, W. S. D. Wilcock, J. B. Diebold, and J. M. Babcock (2007), Seismic structure of the Endeavour Segment, Juan de Fuca Ridge: Correlations with seismicity and hydrothermal activity, *J. Geophys. Res.*, *112*(B2), B02401, doi:10.1029/2005jb004210.

Van Avendonk, H. J. A., A. J. Harding, J. A. Orcutt, and J. S. McClain (2001), Contrast in crustal structure across the Clipperton transform fault from travel time tomography, *J. Geophys. Res.*, *106*, 10961-10981, doi:10.1029/2000JB900459.

Watkins, W. A., P. Tyack, and K. E. Moore (1987), The 20-Hz signals of finback whales (Balaenoptera physalus), *J. Acoust. Soc. Am.*, *82*(6), 1901-1912, doi:10.1121/1.395685.

Weekly, R. T., W. S. D. Wilcock, D. R. Toomey, E. E. E. Hooft, and A. Wells (2011), Upper- to Mid-Crustal Velocity Structure of the Endeavour Segment: Implications for Crustal Construction, *Eos Trans. AGU*, Fall Meet. Suppl., Abstract V11E-2552.

Weekly, R. T., W. S. D. Wilcock, E. E. E. Hooft, P. R. McGill, and D. S. Stakes (2013), Termination of a 6 year ridge-spreading event observed using a seafloor seismic network on the Endeavour Segment, Juan de Fuca Ridge, *Geochem. Geophys. Geosyst.*, *14*, doi:10.1002/2012GC004249.

West, M., W. Menke, M. Tolstoy, S. C. Webb, and R. A. Sohn (2001), Magma storage beneath Axial Volcano on the Juan de Fuca mid-ocean ridge, *Nature*, *413*, 833-836, doi:10.1038/35101581.

Wiemer, S., and M. Wyss (2002), Mapping spatial variability of the frequency-magnitude distribution of earthquakes, *Adv. Geophys.*, *45*, 259-302.

Wilcock, W. S. D., and J. R. Delaney (1996), Mid-ocean ridge sulfide deposits: Evidence for heat extraction from magma chambers or cracking fronts?, *Earth Planet. Sci. Lett.*, *145*, 49-64, doi:10.1016/S0012-821X(96)00195-1.

Wilcock, W. S. D., and A. McNabb (1996), Estimates of crustal permeability on the Endeavour segment of the Juan de Fuca mid-ocean ridge, *Earth Planet. Sci. Lett.*, *138*(1-4), 83-91, doi:10.1016/0012-821X(95)00225-2.

Wilcock, W. S. D., and A. T. Fisher (2004), Geophysical constraints on the sub-seafloor environment near mid-ocean ridges, in *The subseafloor biosphere at mid-ocean ridges*, edited by W. S. D. Wilcock, et al., pp. 51-74, AGU Geophysical Monograph.

Wilcock, W. S. D., S. D. Archer, and G. M. Purdy (2002), Microearthquakes on the Endeavour segment of the Juan de Fuca Ridge, *J. Geophys. Res.*, *107*(B12), 2336, doi:2310.1029/2001JB000505.

Wilcock, W. S. D., E. E. E. Hooft, D. R. Toomey, P. R. McGill, A. H. Barclay, D. S. Stakes, and T. M. Ramirez (2009), The role of magma injection in localizing black smoker activity, *Nature Geosciences*, doi:10.1038/NGEO1550.

Wilcock, W. S. D., P. R. McGill, E. E. E. Hooft, D. R. Toomey, H. M. Patel, D. S. Stakes, A. H. Barclay, T. M. Ramirez, and R. T. Weekly (2007), The deployment of a long-term seismic network on the Juan de Fuce Ridge, presented at 2007 Oceans 2007, Vancouver, Canada, Sept. 29 - Oct, 1..

Wilson, D. S. (1993), Confidence-intervals for motion and deformation of the Juan de Fuca Plate, *J. Geophys. Res.*, *98*(B9), 16053-16071, doi:10.1029/93JB01227.

Wolfe, C. J., G. M. Purdy, D. R. Toomey, and S. C. Solomon (1995), Microearthquake characteristics and crustal velocity structure at 29°N on the Mid-Atlantic Ridge: The architecture of a slow spreading segment, *J. Geophys. Res.*, *100*(B12), 24449-24472, doi:10.1029/95JB02399.

Appendix A

AUTOMATED EARTHQUAKE DETECTION AND LOCATION ALGORITHM

A.1 Development of algorithm

Because of the large number of earthquakes in the data set, I developed a Matlab-based algorithm to automatically pick *P*- and *S*-wave arrival times and locate earthquakes along the Endeavour segment using *Hypoinverse* [*Klein*, 2002]. The logic used to detect and locate earthquakes is outlined in Figure A1 and includes steps of finding events, eliminating whale calls, making picks, determining hypocentral locations, and then iteratively refining the picks and locations. First, I apply a 5 Hz high-pass filter and calculate the ratio of the root-mean-square (RMS) of the demeaned signal using short- and long-term average windows (STA and LTA, respectively) spanning 0.25 and 30 seconds, respectively. I identify triggers when the STA/LTA ratio exceeds a threshold of three after being below that threshold for a period of at least ten seconds. This constraint limits the capability to detect closely spaced earthquakes, but prevents duplicate detections of the same earthquake. Individual triggers are grouped into an "event" when the algorithm triggers on at least four distinct stations within a 2.5 s window. Since the network contains extensive recordings of blue and fin whale vocalizations at frequencies ~20 Hz [*Cummings and Thompson*, 1971; *Watkins et al.*, 1987], I eliminate whale calls by calculating the percentage of spectral energy between 15 and 30 Hz for a 2 s window starting 0.5 s before each trigger, and discarding an event if the median value for triggers associated with the event is greater than 45%.

My approach to picking *P*-waves is to initially allow multiple *P*-wave picks for each

station; *P*-waves with low signal-to-noise are common and the algorithm often incorrectly picks spurious early arrivals or higher-amplitude later arrivals when restricted to making a single *P*-wave pick for each station. To make *P*-wave picks I compute the running RMS value of a 0.2-s-long window and normalize each value by taking its ratio to the RMS value in a 0.5-s-long window ending 0.2 s before the 0.2-s-long window. The picking threshold for this ratio is set to one-tenth of the maximum value (which makes the pick threshold independent of signal-noise-ratio) but with a minimum value of 7.5 (a value based on experience to avoid picking signals with very low signal-noise-ratio). Picks are made when the ratio exceeds the threshold and no other picks are present less than 0.7 s beforehand. Since typical *S*-minus-*P* times for local earthquakes are ~0.6 s, this last step reduces the possibility of erroneously picking the S-wave arrival as the *P*-wave. *P*-waves are assigned weights based on maximum amplitude of the RMS ratio with amplitudes ≤10, between 10 and 50, and ≥50 and assigned weights of 0.25, 0.5 and 1, respectively.

To make preliminary *S*-wave picks, I filter the seismic traces on the horizontal channels using a 5-12 Hz bandpass filter, sum the RMS amplitudes of the station's horizontal channels, apply a Gaussian smoothing operator with a 0.1 s half-width to the summed RMS signal, and pick the *S*-wave onset at 50% of the peak RMS. *S*-waves were assigned weights based on the ratio of peak smoothed RMS amplitude to the median smoothed RMS amplitude in a 1-s window before the pick. Ratios of ≤5, between 5 and 10, and ≥10 are assigned weights of 0.25, 0.5 and 1, respectively.

Figure A2 shows examples of waveforms and corresponding *P*- and *S*-wave picks for a typical local (Figure A2a) and regional (Figure A2b) earthquake on a single station. Figures A3 and A4 show waveforms and picks of local and regional events, respectively, for all stations.

For *S*-waves, a visual inspection of picks indicates that this technique tends to pick *S*-waves later than an analyst. Ideally, the algorithm would pick them earlier by using a smaller threshold than 50% of peak RMS. However a higher threshold was necessary to avoid erroneously picking *S*-*P* converted phases on a significant portion of waveforms, particularly for regional events (Figure A2b and A4).

Earthquake locations are obtained by minimizing the weighted squares of the travel-time residuals using *Hypoinverse* [*Klein*, 2002]. I use a 33-layer one-dimensional velocity model (Figure 2) that includes a low-velocity region in the uppermost 400 m. The *P*-wave velocity model is based on an earlier seismic refraction experiment [*Cudrak and Clowes*, 1993] while *S*-wave velocities were derived assuming $V_P/V_S = 3.0$ above 0.4 km depth and $V_P/V_S = 1.72$ below 0.4 km [*Wilcock et al.*, 2002]. The minimum location requirements include 6 total *P*- and *S*-wave arrivals comprised of at least 2 *P*-waves and 2 *S*-waves and recorded on at least 4 stations. *S*-waves were down-weighted by a factor of 0.5 to reflect increased picking uncertainty. Epicenters that locate more than 3 km away from all stations are constrained to a fixed depth of 3 km; this value is consistent with the typical depth of off-axis earthquakes in the region [*Wilcock et al.*, 2002].

My approach is to first attempt to locate the earthquake using only *P*- or *S*-waves and if this is successful, expand the hypocentral solution to include both phases (Figure A1). I start with *P*-waves, and iteratively remove picks with large residuals until either the weighted sum of squared residuals is less than 0.1 s or there are fewer than 4 *P*-wave picks. If this initial attempt is unsuccessful, then I attempt to locate the earthquake using all permutations of *P*-waves. If a location is found, I then attempt to maximize the number of *P*-wave picks by forward modeling arrival times and adding automatically picked *P*-waves to the location that occurs within 0.1 s of

the predicted arrival time. If a *P*-wave location cannot be obtained, I use similar logic to locate the earthquake using only *S*-waves. Assuming a successful single-phase location, I then attempt to locate the event using both *P*- and *S*-wave picks. As before, I iteratively remove picks with large residuals until the weighted sum of squared residuals is less than 0.2 s or I cannot satisfy the minimum criteria.

All *P*- and *S*-wave picks used in successful two-phase locations are refined using an autoregressive (AR) technique that has been shown to accurately pick the onset of *P*- and *S*-waves automatically [*Takanami and Kitagawa*, 1988]. This technique decomposes the seismic waveform into two locally stationary AR models, one for the seismic signal and one for the noise preceding the body wave onset, and picks the arrival time as the boundary that best fits the waveform as determined by minimizing the Akaike Information Criterion [*Takanami and Kitagawa*, 1988]. Since this technique can become computationally expensive with large amounts of data or higher model order, I restrict the times about the initial *P*- and *S*-wave picks to 0.6 s and 1.0 s, respectively, while using an AR model order of 5. Visual inspection shows that the *P*-wave picks made using the AR method are consistently better than the RMS-threshold based picks. However, it was visually unclear if initial *S*-wave picks were significantly improved using the AR method.

To resolve which *S*-wave picking method produced higher quality locations I considered earthquakes located with a minimum of 8 arrivals using the AR-based *P*-wave picks and either the RMS-based or AR-based *S*-wave picks. For earthquakes located using the RMS-based S picks, the weighted RMS residual for *S*-waves is 165 ms while the value for the AR-based S picks is 210 ms. Due to the smaller residual for hypocentral solutions that included the RMS-based *S*-wave picks, I decided to use these locations in the final catalog.

To estimate hypocentral uncertainties, *Hypoinverse* [*Klein*, 2002] requires a value for the picking (or reading) error, σ, of a fully weighted *P*-wave arrival. Following [*Sohn et al.*, 1998a], I calculate this value according to

$$\sigma^2 = \frac{\sum_{i=1}^{n}\sum_{j}^{m_i} w_{i,j}^2 \Delta t_{i,j}^2}{\sum_{i=1}^{n}(m_i - p)} \qquad (1)$$

where *i* and *j* are indices of the earthquake and arrival time observation, respectively, *n* is the number of earthquakes, *p* is either 3 or 4 depending on whether the earthquake depth remains fixed during location, *m* is the number of arrival time observations for a particular earthquake, Δt is the travel time residual, and *w* is the weight assigned to an arrival (the product of the pick weight, phase weight and any down weighting applied by *Hypoinverse*). I obtain a value of 95 ms for the full catalog.

To account for local variations in upper crustal structure beneath each receiver, station corrections (Table A1) were determined by iteratively relocating earthquakes with at least 10 arrivals, and iteratively adjusted the correction for each station and phase based on the mean residual with the additional constraint that the mean correction for *P*- and *S*-waves equals zero. The station corrections converged after ~40 iterations. All the additive station corrections for *P*-waves are positive values while all but two are negative for the *S*-wave corrections. This is consistent with the observation that the automatic *S*-wave picks tend to be late but may also be indicative of errors in the assumed velocity model.

A.2 Comparison of automatic and manual catalogs

To evaluate the performance of the algorithm, I compared the catalog generated by the

automated algorithm with catalogs of subsets of the data picked by analysts. The first analyst catalog comprises proximal earthquakes recorded during the first year of the Keck network [*Wilcock et al.*, 2009]. The second comprises earthquakes recorded by the Keck network during the February 2005 swarm [*Hooft et al.*, 2010]. The third comprises larger events (M_W > ~2.5) located with land-based stations of the Canadian National Seismograph Network (CNSN).

A.2.1 Vent-field earthquakes: 8 August 2003 – 1 August 2004

During the first year of the experiment, student analysts located 3,222 proximal earthquakes using at least 4 arrivals and 1 *P*- and 1 *S*-wave [*Wilcock et al.*, 2009]. The automatic algorithm successfully located 2,340 of these earthquakes (73%) (Figure A5a) as well as an additional 1,970 earthquakes not included in the analyst catalog (Figure A5b). If only higher quality locations with at least 10 arrivals are considered, then the algorithm successfully locates 1,367 of 1,521 (90%) and an additional 1,021 not located by the analyst.

I calculate the median difference of pick times and their median deviation for *P*- and *S*-waves for each station using 1,969 earthquakes with at least 8 arrivals (Table A2). Histograms of pick differences for station KENE are shown in Figure A6a-b. The algorithm typically picked the onset of *S*-waves 70-100 ms later than the analyst did, while it picked *P*-waves ~20 ms earlier. The late *S*-wave picks result from the conservatively high picking threshold used to avoid picking converted phases prior to the *S*-wave arrival. The median offset between collocated epicenters after applying station corrections is 0.6 km, which is comparable to the median location uncertainties for earthquakes in this region (Table 2). The automatically located earthquakes are offset, on average, 200 m west and 140 m south of the analyst locations (median offsets are 100 m west and 60 m south).

A.2.2 February 2005 swarm

I use 5,612 regional swarm earthquakes from the period 21 February through 5 March 2005 that were manually picked by *Hooft et al.* [2010] to evaluate the performance of the algorithm for events that are well outside the Keck network. The algorithm successfully located 3,042 of these events (55%) (Figure A5c) and an additional 1,919 earthquakes that were not picked by the analyst (Figure A5d). The lower detection rate compared to the manual catalog is not unexpected because the swarms effectively increase background noise levels and it is difficult to automatically separate closely spaced earthquakes.

The *S*-waves are again picked systematically later than the analyst picks with median differences on the order of 200-300 ms for each station (Figure A6 and Table A2). The larger misfit for regional *S*-waves is a result of the less impulsive onset of this phase compared to the proximal earthquakes. For *P*-waves, the pick time differences have a larger scatter than for proximal earthquakes (Figure A6c) but the median differences are smaller and only ~10 ms (Table A2). For earthquakes in the Southwest Endeavour Valley region, the median offset between collocated epicenters is 2.9 km, which is larger than the median location uncertainties for this region (Table 2). Furthermore, the algorithm tends to systematically locate earthquakes 2.4 km south and 500 m east, on average of the analyst locations. This discrepancy is likely partially a result of slightly different *S*-wave velocity models used in the two studies but also reflects the significant offset in *S*-wave pick times.

A.2.3 Comparison with the Canadian National Seismograph Network

During deployment of the Keck array, the Canadian National Seismograph Network

(CNSN) (http://earthquakescanada.nrcan.gc.ca/index-eng.php) located a total of 70 earthquakes along the Endeavour ranging in moment magnitude (M_W) from 2.2 to 5.4; four of the larger events are included in the Global Centroid Moment Tensor catalog (http://www.globalcmt.org). The automated algorithm successfully located 35 of the 70 CNSN events (50%), with most of the earthquakes located during the February 2005 swarm. The missed earthquakes generally have emergent body wave arrivals and a poor signal-noise ratio, which made it difficult to identify a clear first arrival. During peak swarm activity, closely spaced events were especially difficult to locate due to the overlapping *P*- and *S*-wave codas. In these cases, the algorithm attempted to only pick the earlier event. Times and locations of the missed events were added to the catalog after manually picking *P*- and *S*-waves from the Keck seismic data. For each event, I was typically able to pick at least 4 *P*-waves and 2 *S*-waves, but there were seven events with clipped waveforms that were located with only *P*-waves.

Compared to the CNSN catalog, the algorithm produces a smaller range of earthquake magnitudes with the largest events being underestimated by up to two orders of magnitude and smaller events slightly overestimated (Figure A7). It is to be expected that the algorithm would underestimate the magnitudes for larger events because some waveforms clip and corner frequencies are likely to be substantially less than the 10 Hz cutoff frequency used for the magnitude calculation. The source of the overestimate for smaller events is harder to explain but might reflect the different frequencies and methods used to make the calculations. I substituted the earthquake magnitudes reported by the CNSN for the calculated magnitudes for all earthquakes in the CNSN catalog.

Figure A1. Flowchart summarizing the earthquake detection and location process. Only locations that include both *P*- and *S*-waves are included in the final hypocentral catalog.

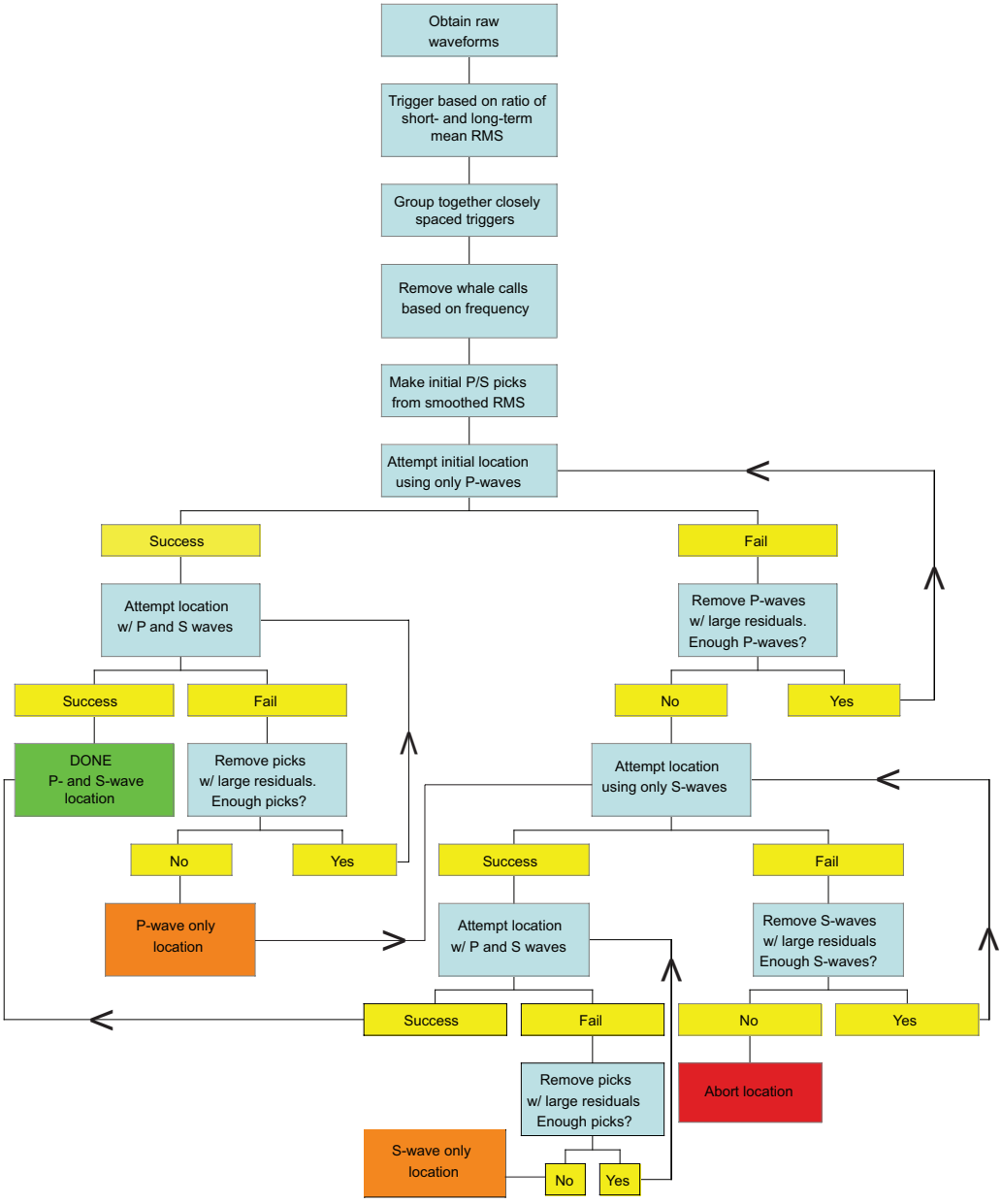

Figure A2. Examples of preliminary automatic *P*- and *S*-wave picks (red lines) for (a) a local earthquake with high signal to noise ratio and an impulsive *S*-wave arrival, and (b) a regional earthquake with a lower signal to noise ratio and an emergent *S*-wave arrival. The algorithm successfully identified the onset of the *P*- and *S*-wave for the local earthquake. The regional earthquake illustrates how a lower signal to noise ratio can result in an erroneous second *P*-wave pick, and how ambiguities associated with a non-monotonic ramp up in RMS values (possibly related to *P*-to-*S* converted arrivals) contribute to uncertainties in the *S*-wave pick.

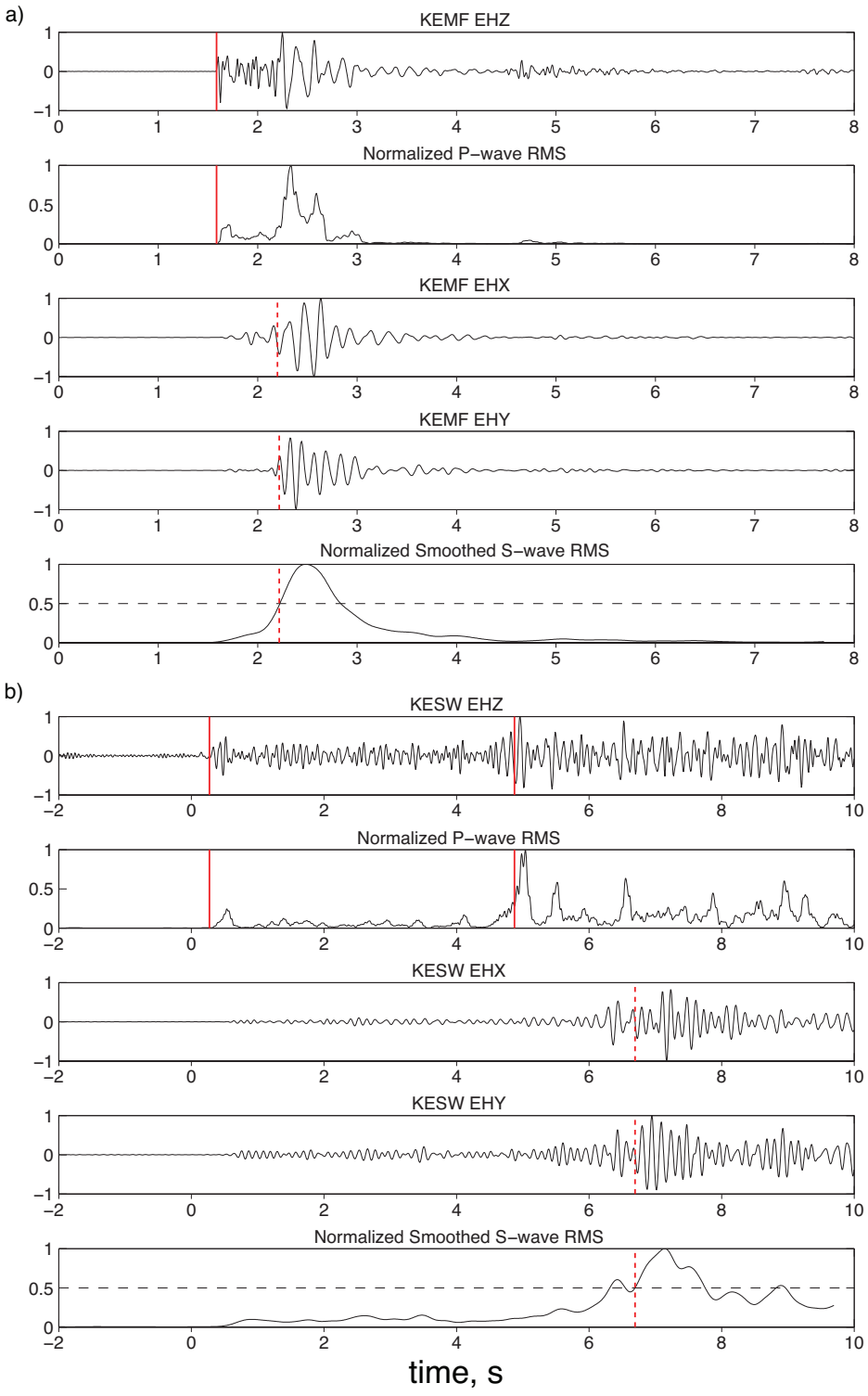

Figure A3. Waveforms for a typical event located within the network. Automatic *P*- (red) and *S*-wave (green) picks were made for all stations.

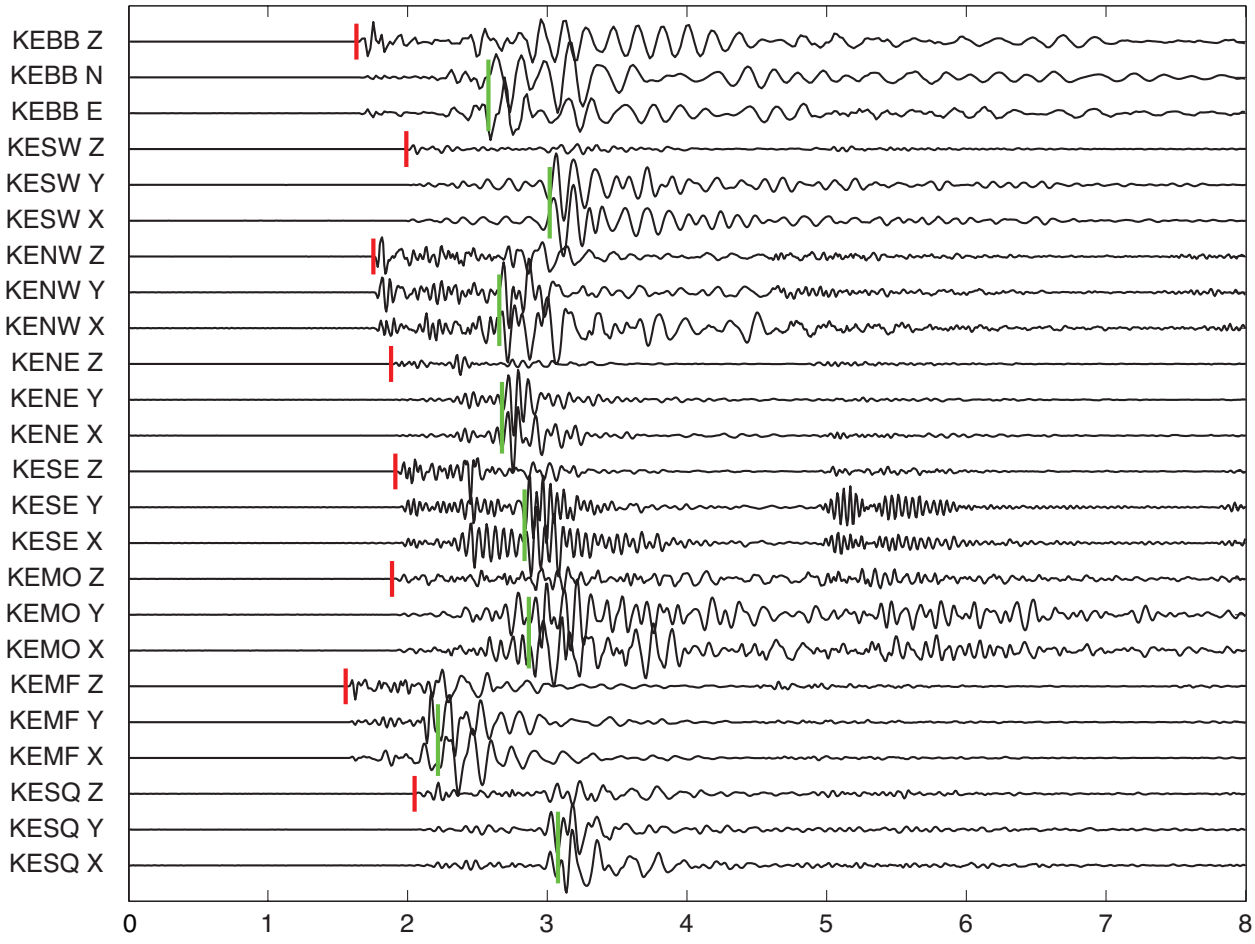

Figure A4. Waveforms for typical "regional" event located within the Endeavour-West Valley OSC. *P*-waves (red) were automatically picked for all stations, but *S*-waves (green) were only picked for 5 of the 8 stations.

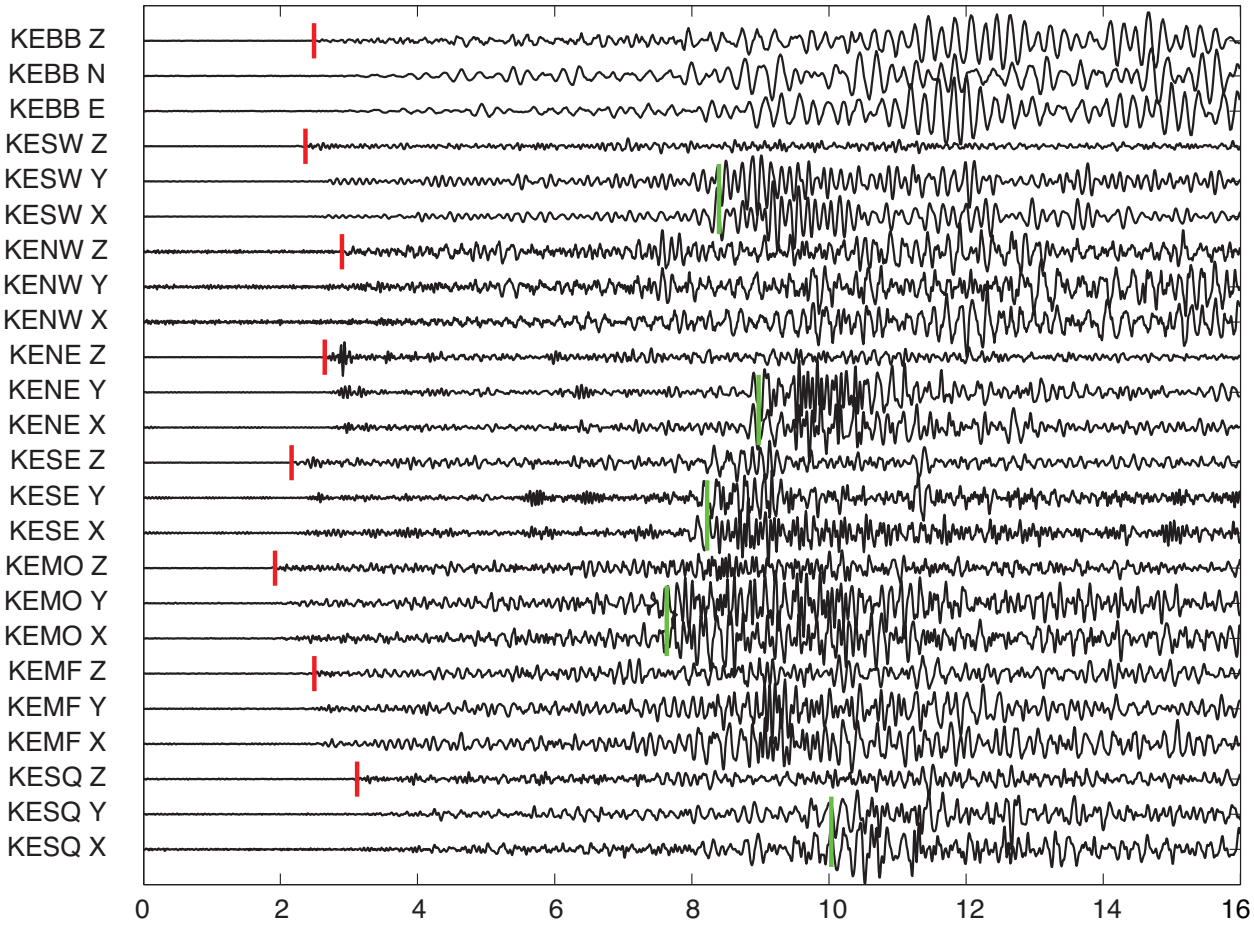

Figure A5. (a) Histogram of local earthquakes in 2003-4 located by analysts [*Wilcock et al.*, 2009] as a function of the number of analyst-picked arrivals (red) showing the subset of these events located by the automatic algorithm (blue). (b) Earthquakes located by the automatic algorithm during the same period as (a) as a function of the number of automatic picks (blue) showing the subset of these earthquakes located by the analysts (red). (c-d) As for (a-b) except using regional events located by [*Hooft et al.*, 2010] during the February 2005 swarm.

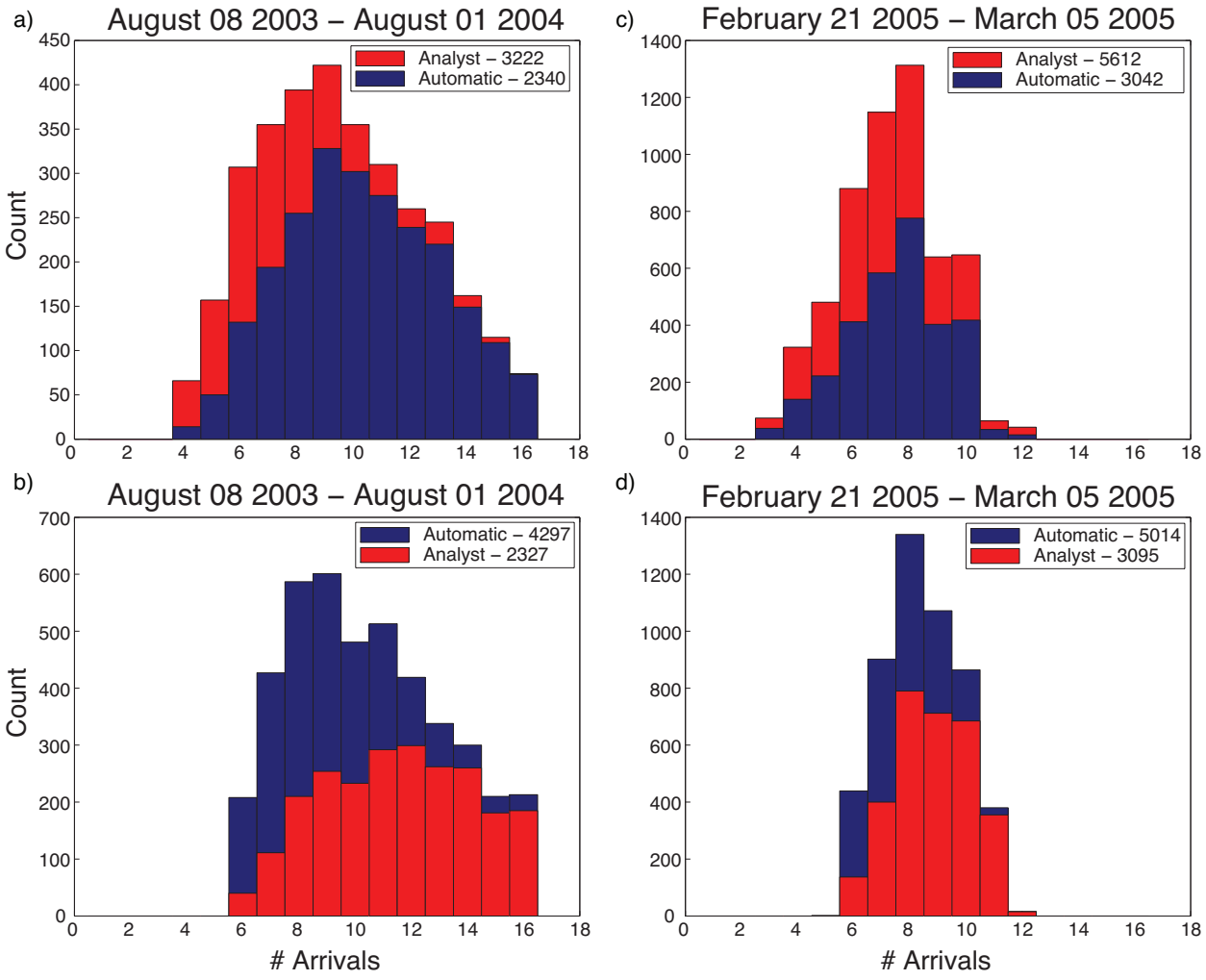

Figure A6. Histograms of the difference between automatic and analyst picks for station KENE for (a-b) local earthquakes in the vent fields in 2003-4 [*Wilcock et al.*, 2009] and (c-d) regional events in the February 2005 swarm [*Hooft et al.*, 2010]. The median (Δt) and the median absolute deviation ($\hat{\sigma}$) of the misfit are listed.

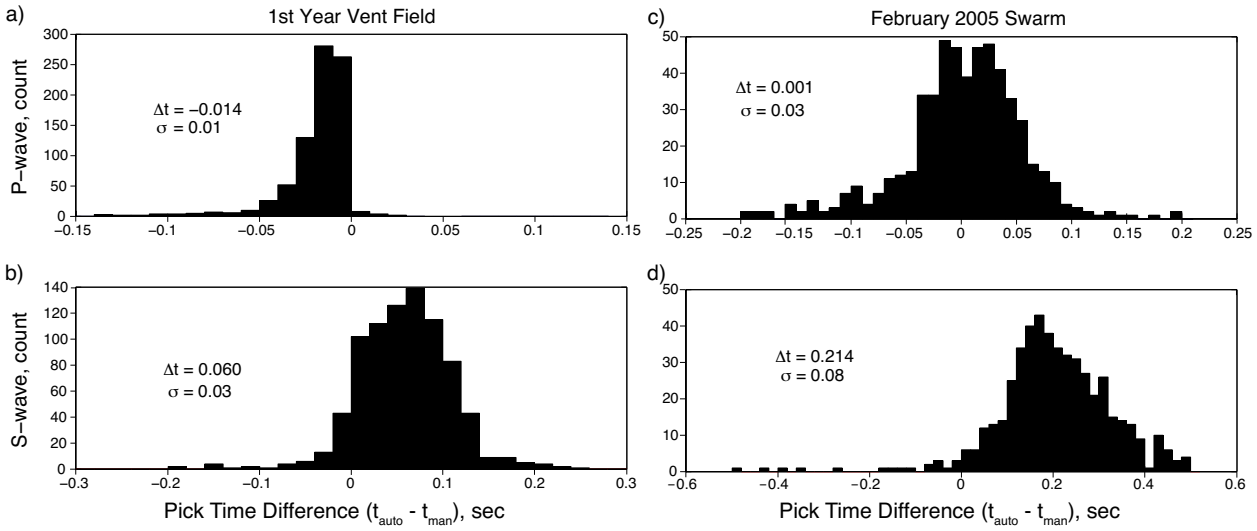

Figure A7. Local magnitudes (M_L) calculated for larger earthquakes using the Keck catalog plotted against magnitudes listed in the Canadian National Seismograph Network catalog.

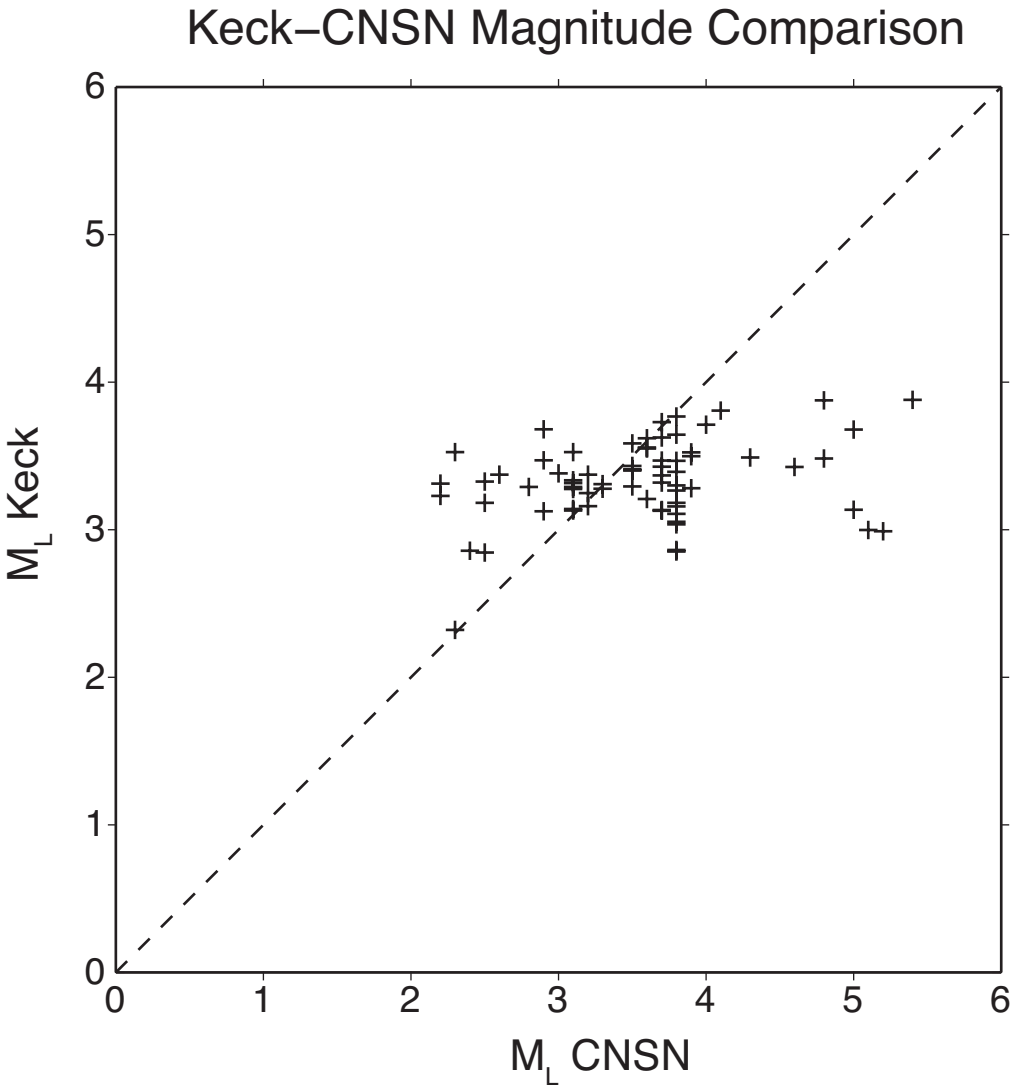

Table A1: *P*- and *S*-wave station corrections.

Station	P (sec)	S (sec)
KESQ	0.1387	0.0023
KEMF	0.0643	0.0096
KEMO	0.1391	-0.0533
KESE	0.1135	-0.0968
KENE	0.1415	0.0009
KENW	0.1035	-0.1770
KESW	0.1138	-0.1925
KEBB	0.1356	-0.2775

Station corrections were calculated using earthquakes with a minimum of 10 arrivals and were iteratively calculated until the difference between iterations was negligible. Values converged after ~40 iterations.

Table A2: Comparison of automatic and analyst picks

Station	1st-year vent field				February 2005 swarm			
	Δt_P	σ_P	Δt_S	σ_S	Δt_P	σ_P	Δt_S	σ_S
KESQ	-0.024	.01	0.064	.03	N/A	N/A	N/A	N/A
KEMF	-0.015	.01	0.048	.03	N/A	N/A	N/A	N/A
KEMO	-0.024	.01	0.075	.07	N/A	N/A	N/A	N/A
KESE	-0.019	.01	-0.009	.03	-0.010	.04	0.244	.10
KENE	-0.014	.01	0.060	.03	0.001	.03	0.214	.08
KENW	-0.014	.01	0.043	.03	0.010	.03	0.227	.08
KESW	-0.032	.02	0.066	.03	0.006	.03	0.243	.08
KEBB	-0.007	.02	0.137	.07	0.001	.04	0.301	.12

Median misfit values, Δt, and median absolute deviations, σ, for P- and S-waves, in seconds, for 2,632 events from the first year of vent-field earthquakes and 1,937 events from the February 2005 swarm all with at least 8 arrivals. A negative Δt indicates that the automatically picked arrival was systematically picked early compared to the analyst pick. N/A indicates that the station was not in operation or recorded an insufficient number of arrivals.

Appendix B

SYNTHETIC RESOLUTION TESTS FOR SEISMIC STRUCTURE

B.1 Derivative weight sum

To delimit the volume in which the preferred model might be well resolved I analyzed the spatial distribution of ray paths. A spatial measure of the distribution of *Pg* ray paths within the experiment footprint is given by the derivative weight sum (DWS) [*Thurber*, 1983; *Toomey and Foulger*, 1989], which calculates the weighted sum of path lengths influencing each node in the perturbational grid. In short, DWS is a unitless number that describes the influence of ray path density on perturbational grid nodes, and interpretations drawn from results lying below a DWS threshold should be avoided. From inspection of the checkerboard tests (see below), I set a DWS threshold of 10 for masking models. Selecting a precise value was somewhat subjective and depended on the wavelength of the feature of interest, but DWS increased rapidly inside the minimum contour in most of the model space (Figure B1). Ray path distribution in the upper crust was sparse at the outer edges of the experiment and dense within the centralized crustal grid to depths of ~3 km. There was a paucity of ray paths sampling crustal structure below 3 km depth near the central Endeavour segment. This data-limited region of the model resulted from the presence of the AMC located 2 – 3 km beneath the central axial valley [*Van Ark et al.*, 2007], which limited the range that *Pg* could be easily identified.

B.2 Synthetic isotropic inversions

To assess the resolution of the results, I used reconstructions of several types of synthetic models. For all synthetic models, I calculated predicted *Pg* travel-times for the same station-

receiver pairs as in the experiment, added 10 ms of uncertainty to each arrival time, and inverted the data using the same parameters as in the preferred solutions.

I tested the resolution of isotropic structure by constructing synthetic models of checkerboard pattern velocity anomalies that consisted of 5% velocity perturbations applied to the average one-dimensional velocity structure (solid black line in Figure 14a) and alternated between positive and negative anomalies. All the checkerboard tests show that the tomographic inversion has a tendency to underestimate the magnitude of velocity anomalies even in the best resolved regions.

To evaluate the resolution of segment-scale features, I used columnar checkerboard tiles measuring 10, 15, and 20 km on a side in which the polarity of the perturbations did not alternate with model depth. Figure B2 shows map-view sections of the reconstructed anomalies for the 10-km–by-10-km tiles. The tests demonstrate that structural features on the order of ~10 km in size are generally well resolved between 0.5 and 2.5 km depth. The checkerboard pattern is best recovered between 1 – 2 km depth (Figure B2b), where the tiles are more clearly outlined and the percentage recovery is highest. At these depths, I am able to resolve anomalies near the E-WV and Cobb OSCs with greater resolution and a higher percentage recovery than at depths shallower than 1 km or deeper than 2 km (Figure B2a and B2c, respectively). A broad distribution of ray paths near the intersection of the overlapping limbs enables good recovery of the velocity perturbations, but a lack of ray paths at the distal ends of the OSCs prevents satisfactory recovery of structure in these regions. Similarly, anomalies between 1 km and 2 km depth are better recovered at off-axis distance exceeding ~20 km compared to crustal structure at other depths. This is attributed to the high density and broad azimuthal distribution of *Pg* ray paths turn between 1 km and 2 km depth (Figure B1b).

To evaluate the resolution of features located near the more densely sampled central portion of the segment (Figure B1), I analyzed synthetic checkerboard models with 5-km-by-5-km-by-1-km tiles (Figure B3). Unlike the models of Figure B2, the polarity of the velocity perturbations alternated with depth so the vertical resolution could be assessed. Checkerboard anomalies in the upper 1 km are well recovered within 10 km of the ridge but are poorly recovered at larger ranges where they exhibit some horizontal smearing due to poor ray path coverage in the upper crust (Figure B3a). At 1-2 km depth, anomalies are reasonably well recovered near the ridge axis with no evidence for horizontal smearing observed at shallower depths (Figure B3b). Anomalies out to 20 km off-axis are best recovered at these depths (Figure B3). The recovered amplitude of synthetic anomalies at depths greater than ~2.0 km (Figure B3c) is poor compared to shallower depths, which reflects the small percentage of ray paths turning deeper than ~2 km.

To test the limits of resolution near the hydrothermal fields, I performed inversions of synthetic data from a checkerboard model with 2-km-by-2-km-by-1-km tiles (Figure B4). Recovery of synthetic anomalies indicates that structure near the axial valley is well resolved within the upper 2 km, but the amplitude of the recovered anomalies is higher within the upper 1 km. This synthetic model shows that the resolution of the model is sufficient to resolve features on the scale of the spacing of hydrothermal vents.

B.3 Synthetic anisotropic inversions

I conducted a series of synthetic models to evaluate anisotropic component of the inversions. First, to investigate the tradeoff between isotropic and anisotropic structure in the inversion, I considered a synthetic model in which the isotropic component was the average

vertical velocity structure of the preferred model (solid line, Figure 14a) and the amplitude of ridge-parallel anisotropy decreased from 5% at the seafloor to 0% at 4 km depth (dashed line in Figure B5). Figure B6 shows the difference between the starting model and the synthetic model. The differences tend to be relatively small near the ridge axis, while the isotropic structure on the outer edges of the experiment shows a band of relatively high velocity paralleling the 105-km long shot lines. The banding is particularly apparent from 0.8 – 2.0 km depth and mirrors features observed in the preferred inversion of Figure 15. This is attributed to the tendency for some of the anisotropic signal to be mapped in isotropic velocity anomalies beneath regions where the majority of the ray paths are aligned with the shot lines. I therefore avoid interpreting banding parallel to the outer 105-km-long shot lines in the preferred model. It is noted that there is no indication that the ridge parallel banding in the upper 1 km near the ridge axis (Figure 16) is an artifact of mapping anisotropy into isotropic structure.

The recovered anisotropic signal in this inversion is smaller than in the starting model at all depths (Figure B5) and the magnitude of the anisotropic signal tends to decrease off-axis (Figure B7a-c). In order to assess whether this effect might produce the large decrease in the magnitude of anisotropy observed in the preferred model within 5 to 10 km of the ridge axis (Figure 20-21), a second synthetic anisotropic inversion was conducted that was identical to the first except that the magnitude of anisotropy was doubled within 5 km of the ridge axis. Figure B7d-f shows the recovered magnitude of anisotropy at three depths, which more closely resemble anisotropic structure of the preferred inversion (Figure 20).

Figure B8 shows the change in the average percentage of anisotropy off-axis at different depths for the preferred model and for the two synthetic inversions. It is clear that the synthetic inversion with higher anisotropy near the ridge axis more closely reproduces the change in the

magnitude of anisotropy seen off-axis that the model with constant anisotropy. Indeed, it appears that a doubling of anisotropy near the ride axis is insufficient to reproduce the preferred inversion. Thus, I infer that while the inversions will tend to underestimate the magnitude of anisotropy, particularly well off-axis where anisotropy is clearly mapped into isotropic banding, the large decrease in the magnitude of anisotropy off-axis in the preferred model is a real effect. The preferred inversions also shows significantly larger along axis variations in the magnitude of anisotropy than the synthetic inversion of Figure B7d-f, so I infer that along axis variations are required by the data.

To evaluate the ability of the inversions to resolve variations in the orientation of the fast direction of anisotropy, I used synthetic models with checkerboard patterns of anisotropy in which the magnitude was constant throughout the model but the fast direction varied. Figure B9 shows the recovery for two models with 10-km-by-10-km tiles and a fast direction that is rotated by 90˚ and 45˚ between adjacent tiles. Recovery of the synthetic data shows that variations in the orientation of anisotropy near the central portion of the experiment are well resolved, however, the synthetic models are not as well recovered near the margins of the experiment. In these regions, the recovered azimuths are often intermediate between the values of adjacent tiles. The lack of fine-scale resolution is attributed to the relatively poor azimuthal distribution of ray paths near the edges of the experiment.

Figure B1. Map-view sections of the derivative weight sum (DWS) at (a) 0.5 km, (b) 2.0 km, and (c) 3.5 km depth contoured at 10, 100 and 1000 to show the relative density of rays.

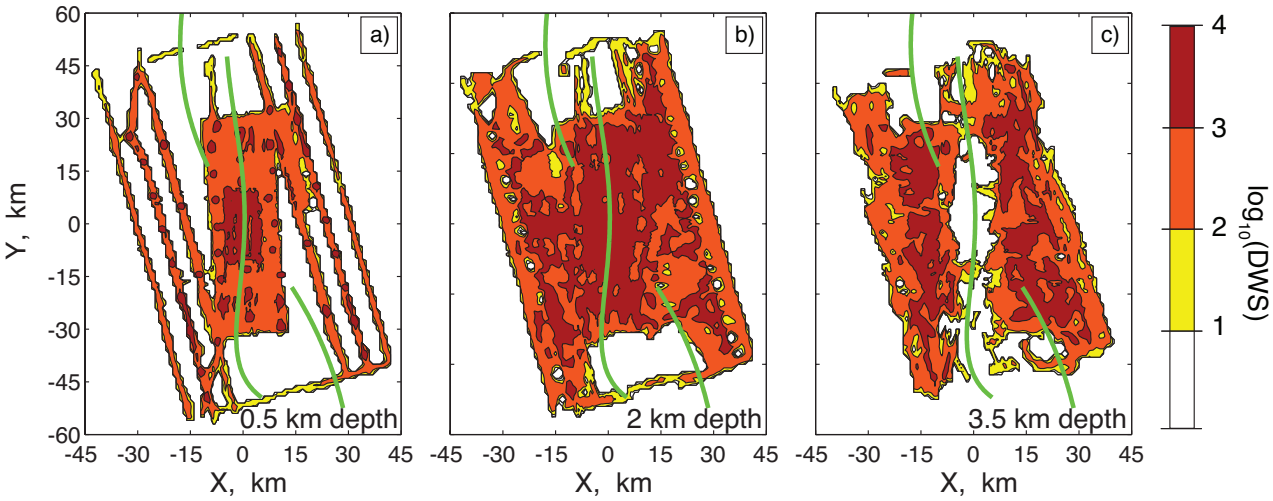

Figure B2. Map-view slices at (a) 0.4 km, (b) 1.4 km, and (c) 2.4 km depths showing results from synthetic isotropic velocity checkerboard tests for columnar 10-km-by-10-km tiles. Velocity perturbations were ±5% from the preferred isotropic model and perturbations did not vary with depth. Green stars show the locations of vent fields. Solid black lines show the traces of the West Valley, Endeavour, and Northern Symmetric segments. The color contours show the percent recovery of the *P*-wave perturbation with a contour interval of 20%.

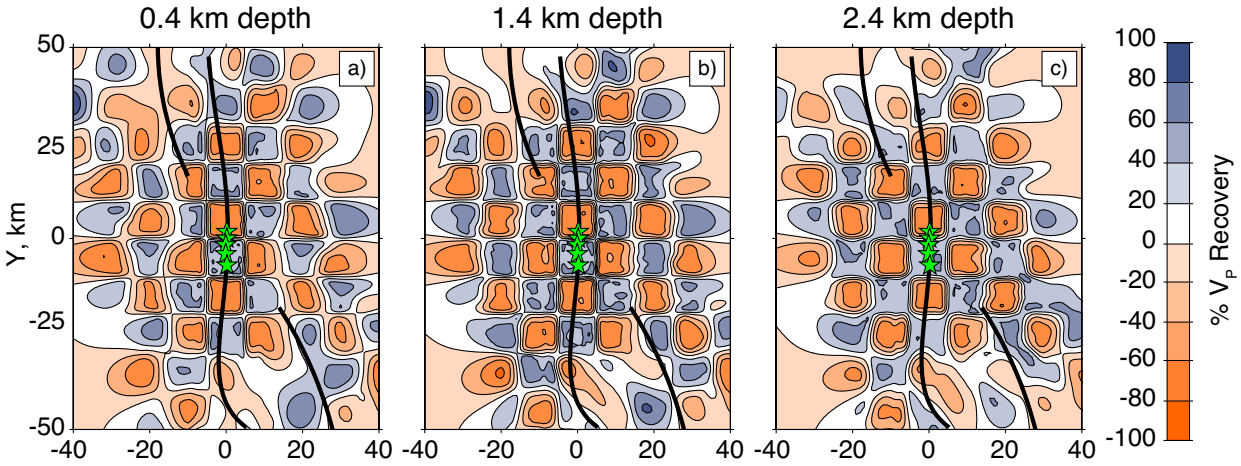

Figure B3. Map-view slices at (a) 0.4 km, (b) 1.4 km, and (c) 2.4 km depths showing results from synthetic isotropic velocity checkerboard tests for 5-km-by-5-km-by-2-km tiles. The same plotting conventions are used as for Figure B2.

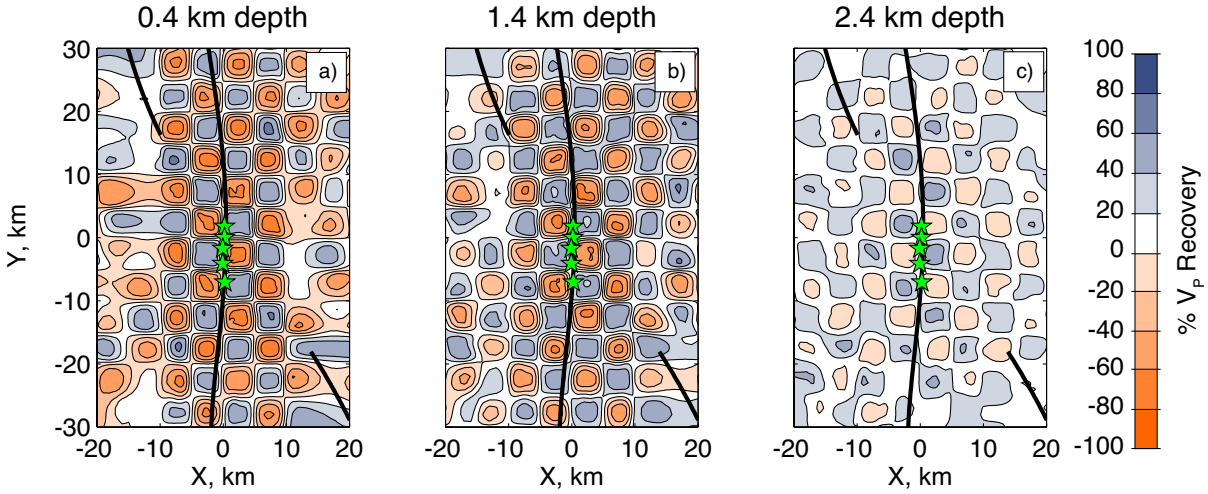

Figure B4. Map-view slices taken at (a) 0.4 km and (b) 1.4 km depths and (c) vertical cross-section through the vent fields (X = 0 km) showing results from synthetic isotropic velocity checkerboard tests for 2-km-by-2-km-by-1-km tiles. The same plotting conventions are used as for Figure B2.

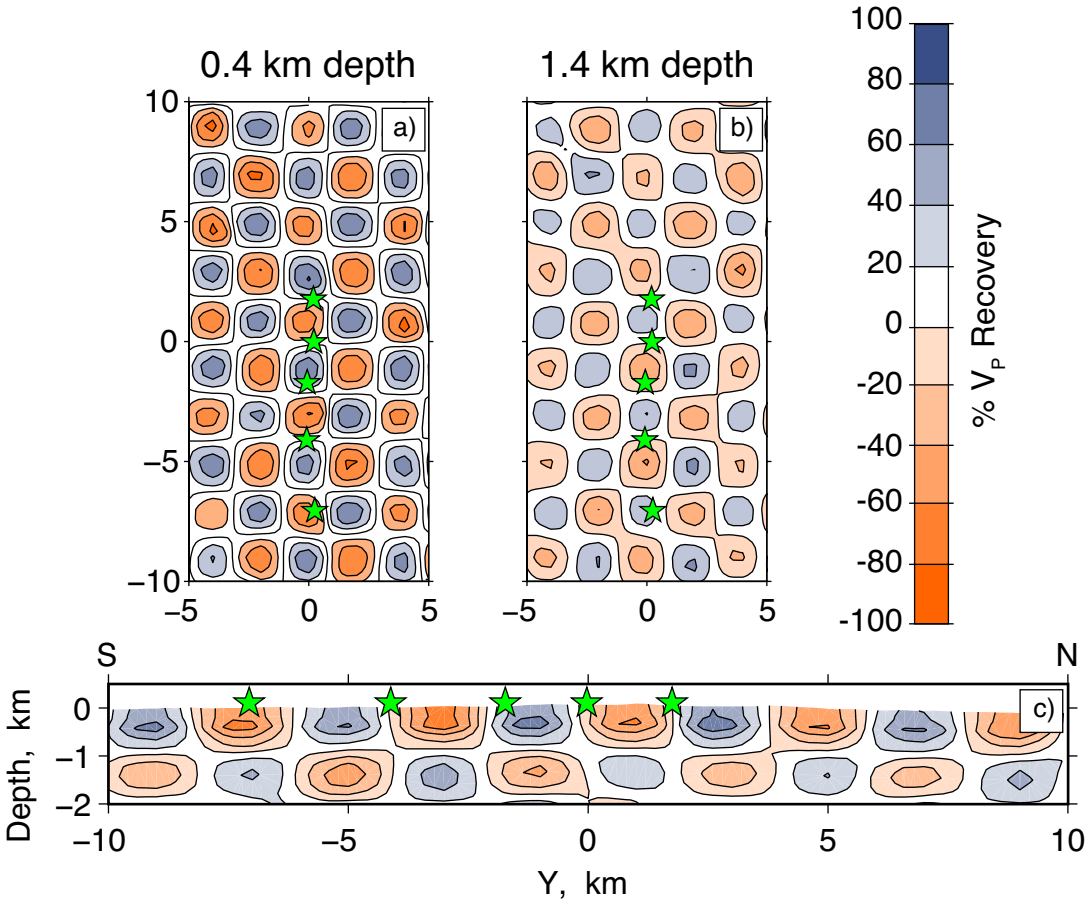

Figure B5. One-dimensional percent anisotropy structure for a synthetic model used to calculate travel times (dashed line) and the vertical average of the model recovered from the inversion in a region extending 10 km to either side of the ridge axis and from Y = -20 km to Y = 20 km (solid line).

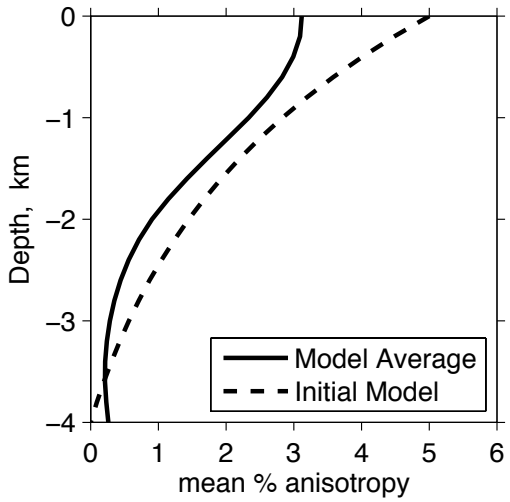

Figure B6. Map-view slices of isotropic velocity anomalies for a synthetic anisotropic inversions that followed the same multi-step inversion procedure described in section 3.5.1 with travel times obtained for a synthetic one-dimensional model with an isotropic component equal to the horizontally averaged model obtained in the inversion (solid black line in Figure 14a) and ridge parallel anisotropy that decreases from 5% at the surface to 0% at 4 km depth (dashed line in Figure B5). The color contours show the difference between the recovered model and the synthetic model. The 105-km long outer shot lines (faint black dots), vent fields (green stars) and traces of the segments (bold black lines) are also shown. Note that regions without ray coverage have positive anomalies because the starting model for the inversion (dashed line in Figure 14a) is faster than the synthetic model.

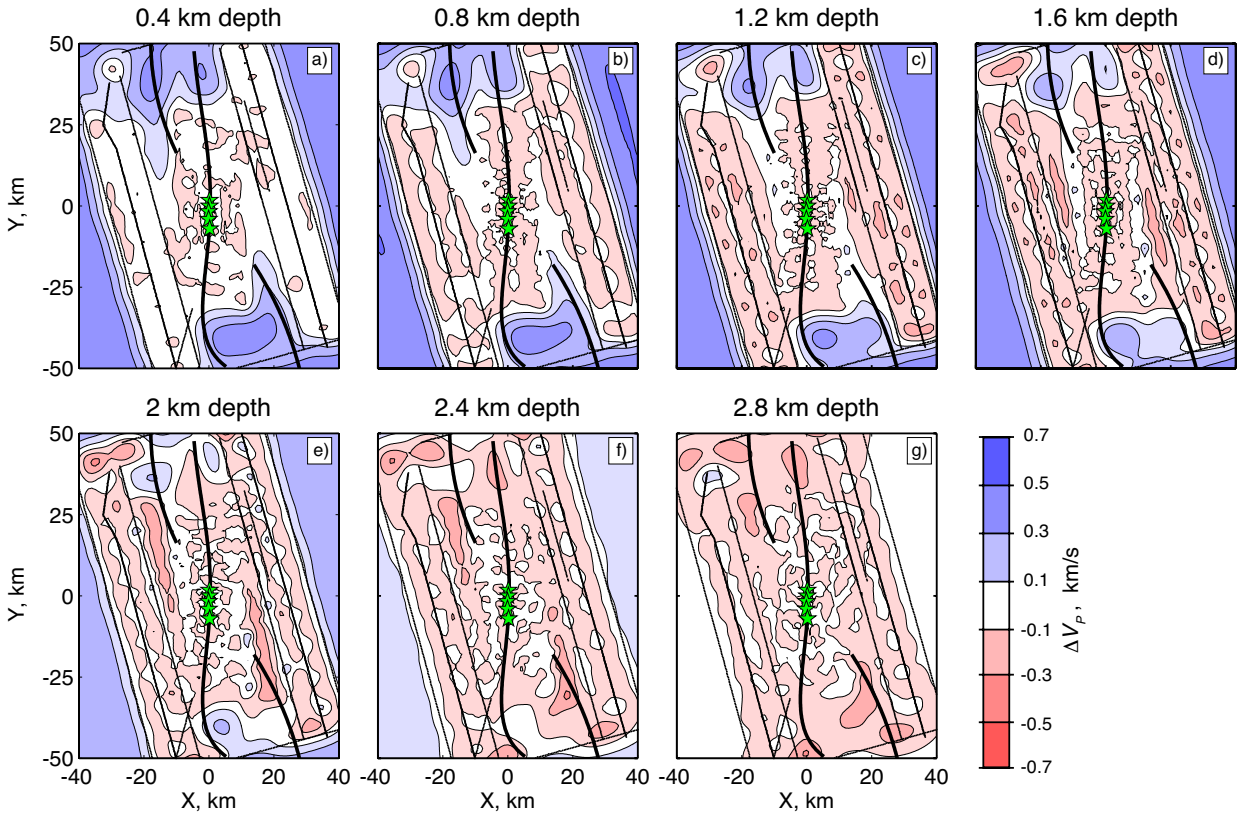

Figure B7. Map-view slices at 0.4 km, 1.2 km and 2 km depths showing the magnitude of anisotropy contoured at 1% intervals for two synthetic inversions. (a–c) Results for the inversion shown in Figure B5-B6 in which the anisotropy in the model used to calculate synthetic travel times varies from 5% at the seafloor to 0% at 4 km depth. (d-f) Results for an inversion in which the model used to calculate synthetic travel times is the same as before except the magnitude of anisotropy is doubled within 5 km of the ridge axis (-5 km < X < 5 km). The vent fields (green stars) and traces of the segments (bold cyan lines) are also shown.

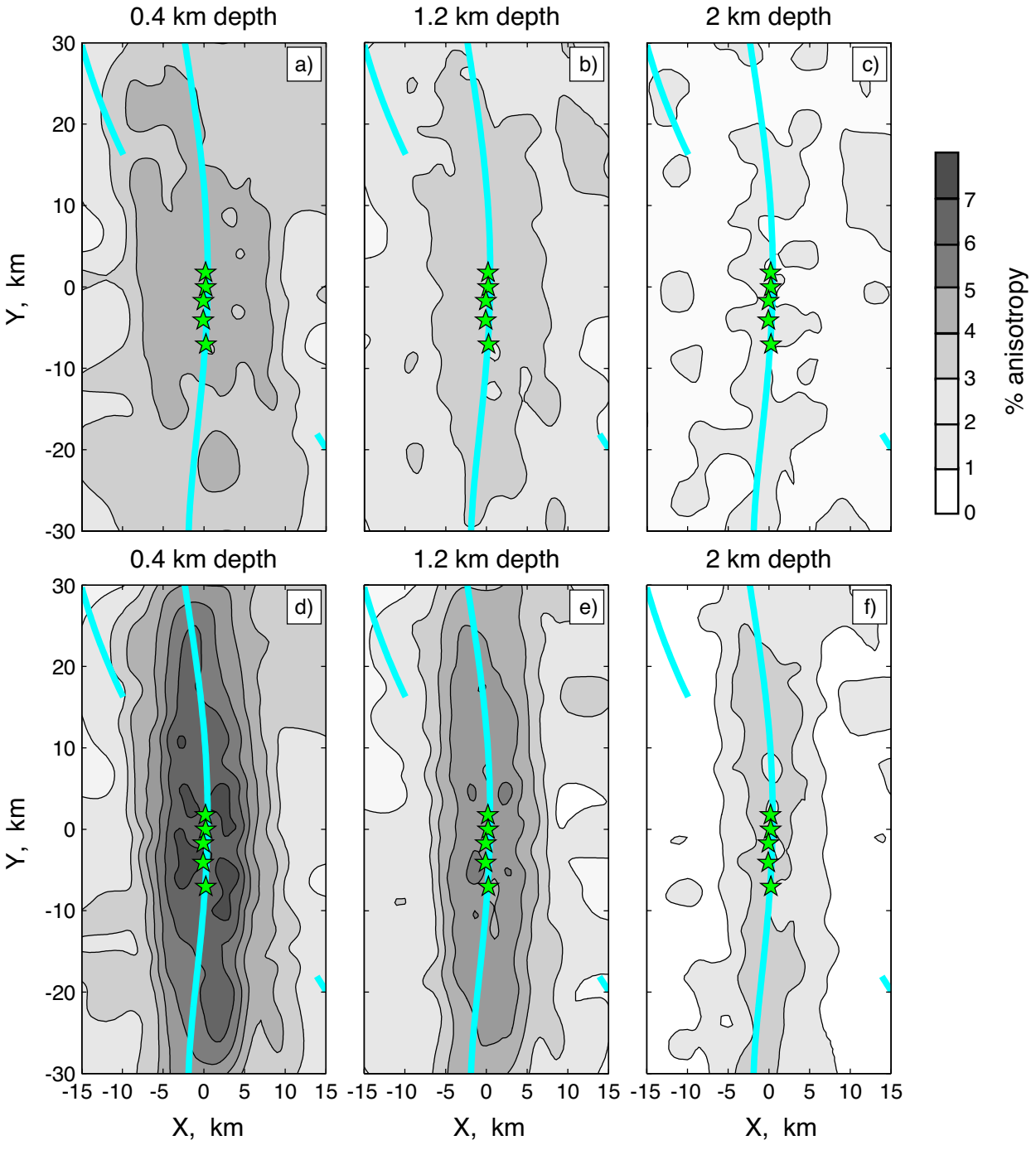

Figure B8. Plots showing the change in average magnitude of anisotropy as a function of off-axis range for the preferred anisotropic model discussed in the text (black line), the synthetic inversion of Figure B7a-c with horizontally invariant anisotropy (red line) and the synthetic inversion of Figure B7d-f with the magnitude of anisotropy doubled within 5 km of the ridge axis (blue). Note that the shape of the curves for the second synthetic inversion more closely resembles that for the preferred isotropic model, indicating that the off-axis decrease in anisotropy is well-resolved.

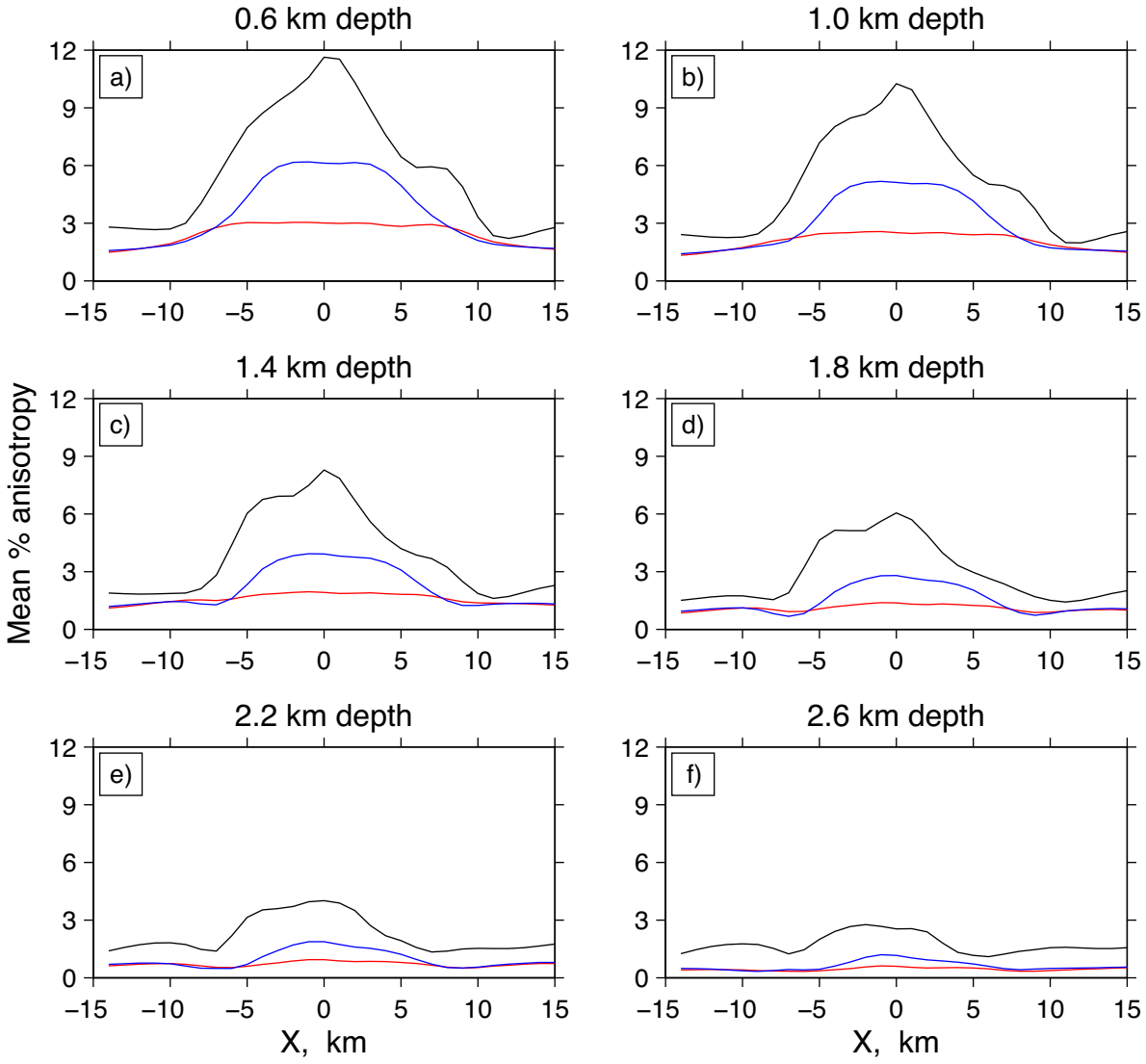

Figure B9. Map-view slices taken at 0.4 km depth for the recovery of synthetic anisotropic checkerboard models for 10-km-by-10-km columnar tiles in which the orientation of seismic anisotropy is perturbed by (a) 90˚ and (b) 45˚. Solid black lines show the orientation and relative magnitude of the fast direction of anisotropy on a 4-km-by-4-km grid. A tick of length 4 km would represent 100% recovery of the anisotropy magnitude. The vent fields (green stars) and traces of the segments (bold black lines) are also shown.